Carlin-Style Gold Mineralization in the Yukon Territory, Canada

Venus Zone, Einarson Property, Anthill Resources Ltd.

By

Nikolett Kovacs

A thesis submitted to the Department of Earth Sciences in partial fulfillment of the requirements for the degree of B.Sc (Hons.)

Memorial University of Newfoundland

December 2014

ABSTRACT

Carlin-style deposits are broadly categorized as a sediment- (predominantly carbonate-) hosted class, with gold contained as solid solution or submicron particles within disseminated pyrite and arsenian pyrite. To date, Carlin-type gold deposits have been largely defined and described in the Great Basin region of Nevada. However, recent discoveries in the Yukon Territory show many of the defining characteristics of Carlin-type gold deposits. The Venus Zone is located in the central eastern part of the Yukon Territory, 15 km east from the Nadaleen Trend, which hosts six recently recognized zones of Carlin-type mineralization in Neoproterozoic carbonates of the Selwyn Basin. Scanning Electron Microscope with Energy Dispersive X-Ray Analyzer (SEM/EDX) identified narrow rims (1-2 μm) of arsenian pyrite on syn-sedimentary framboidal and marcasitized pyrite. Two generations of submicroscopic native gold are observed in close association with: i) arsenian pyrite and stylolitic textures and ii) scorodite. These are suggested to represent ore and post-ore stages of Carlin-style gold mineralization, respectively. Thin section analysis confirmed that the major gold hosting lithology in the Venus Zone is silicified dolostone. Northeast trending brittle faults and second generation (F_2) fold hinges were the primary fluid conduits and structural fluid traps, which localized auriferous mineralizing fluids that arrived after silicification, but before the last phase of deformation. The Venus Zone is proposed to represent an eastern extension of the Nadaleen Trend, an emerging Carlin-style gold district in the Northern Cordillera. The findings of this study should prove useful in informing future exploration for Carlin-style gold deposits on the Einarson Property, and along the larger Nadaleen Trend.

ACKNOWLEDGMENTS

I would like to thank Anthill Resources Ltd. for financial and logistical support for this project during the 2013 field season.

Special thanks to Venessa Bennett for all her support and for setting up this project and supervising me with my data collection. I would also like thank Elizabeth Westberg for her helpful geological discussions and for her friendship.

I would like to thank ATAC Resources Ltd. and the Yukon Geological Survey for all the work experience I've gained from them, which greatly contributed to this research.

Many thanks are owed David Moynihan from the Yukon Geological Survey for his helpful discussions about the Venus Zone and for his regional geological mapping of the Rackla Belt, which helped me to gain a better understanding of the regional geology of the area.

I would also like thank Dr. Steve Piercey and Dr. Tom Calon who sparked my interest in economic and structural geology and for their editorial assistance and suggestions on how to improve the quality of this paper.

I'm also grateful for my family and Nicolai Goeppel who supported me throughout my academic career during all these years.

Lastly, I'm especially thankful for my supervisor, Dr. Graham Layne for his support and guidance throughout this project. Many thanks for assisting me with the SEM-EDX analysis and for supporting the analytical costs of this project. I'm very grateful for all his helpful advice and time that he has dedicated towards my research. Thank you!

Table of Contents

LIST OF TABLES

LIST OF FIGURES

LIST OF ABBREVIATIONS

Cc-	Calcite
Qz-	Quartz
Py-	Pyrite
Apy-	Arsenopyrite
Au-	Native gold
Gn-	Galena
Rea-	Realgar
Orp-	Orpiment
As-	Native arsenic
µm-	Micrometre, micron
fS_{2}-	Sulphur fugacity
fO_2-	Oxygen fugacity
Liq-	Liquid
Lo-	Loellingite
Po-	Pyrrhotite
S-	Sulphur
Sb-	Antimony
Stb-	Stibnite
Hm-	Hematite
Mt-	Magnetite
Ni-	Nickel
Tl-	Thallium
Pb-	Lead
Ag-	Silver
Hg-	Mercury
Zn-	Zinc
Co-	Cobalt
Cu-	Copper
Bi-	Bismuth
SEM-EDX-	Scanning Electron Microscope with Energy Dispersive X-ray Spectroscopy
ppm-	Parts per million
ppb-	Parts per billion
BSE-	Back-scattered electron
SE-	Secondary electron
CTGDs-	Carlin-type gold deposits
Te-	Tellurium
Se-	Selenium
Ba-	Barium
g/t-	grams/tonne
SIMS-	Secondary Ion Mass Spectrometry

LIST OF APPENDICES

CHAPTER 1

CARLIN-STYLE GOLD MINERALIZATION IN NEVADA, USA

INTRODUCTION

Carlin-style gold mineralization is a sediment, predominantly carbonate hosted deposit type where gold (Au) is contained as solid solution or submicron particles in disseminated pyrite and arsenian pyrite. The Carlin Trend is a 60 km long, north-northwest trending belt in Nevada, USA, named after the discovery of the Carlin Mine in 1961 (Figure 1.1). Open pit mining started in 1965 and underground mining began in 1993 in the Carlin Mine. The deposits occur in linear trends or clusters with over 42 separate deposits. Some of the largest deposits are Carlin, Cortez, Getchell, and Jerritt Canyon accounting for more than 90% of Au in Carlin-style gold deposit (CTGD) worldwide. The Carlin Trend contains over 6000 tons of gold, constituting the second largest concentration of Au in the world, and accounting for 9% of the annual worldwide production, making the United States the 4th largest gold producer in the world. The total gold production exceeded 50 million ounces in 2002 (Nevada Bureau of Mines and Geology, 2004). To date, the best-documented examples of Carlin-type gold deposits are found in the Carlin district of Nevada, United States.

REGIONAL GEOLOGY

Sedimentary Host Rocks

Gold deposits in the Carlin Trend are hosted in a wide variety of Paleozoic, dominantly Devonian to early Mississippian silty, shelf-carbonates and clastic sequences. Gold mineralization particularly favours laminated, locally bioturbated, silty to dolomitic limestones with local fossiliferous beds and debris flows; however, thin-bedded, calcareous siltstone with intercalated siliceous mudstones are also gold mineralized. The most extensive gold mineralization is found below the Roberts Mountains Thrust Fault in a km wide zone of the Rodeo Creek, Popovich, and Roberts Mountains Formations. Less intensive, structurally controlled vein-style gold mineralization also occurs above the Roberts Mountains Thrust Fault in lower Ordovician to Middle Silurian, easterly directed imbricated thrust sheets of siliceous mudstone, chert, and minor greenstone with local carbonate strata (Figure 1.2) (Teal and Jackson, 2002).

Intrusive Rocks

The largest deposits such as Cortez, Getchell and Goldstrike in the Carlin Trend are all spatially associated with Jurassic or Cretaceous plutons. North-northwest trending, fault bounded dikes are also common. These dikes are mafic to intermediate in composition, locally pre-ore mineralized with local, extensive (50-200 m) metamorphic aureole development. Gold mineralization is common around the margins of the plutons or at the contact between the metamorphic hornfels

aureoles and the unmetamorphosed country rocks (Teal and Jackson, 2002). Extension during the Eocene with limited low strain reactivated the north-northeast striking faults near the Mesozoic intrusions forming complex fracture mesh adjacent to the plutons. These sites of enhanced permeability, located asymmetrically around the margins of intrusions, favored subsequent gold deposition (Cline et al., 2005). In general, these intrusive bodies have an empirical relationship with gold mineralization because they intruded along the same structural weakness that acted as a fluid conduit for later gold mineralizing fluids; however, there is no direct relationship proven between the main intrusive events and gold mineralization.

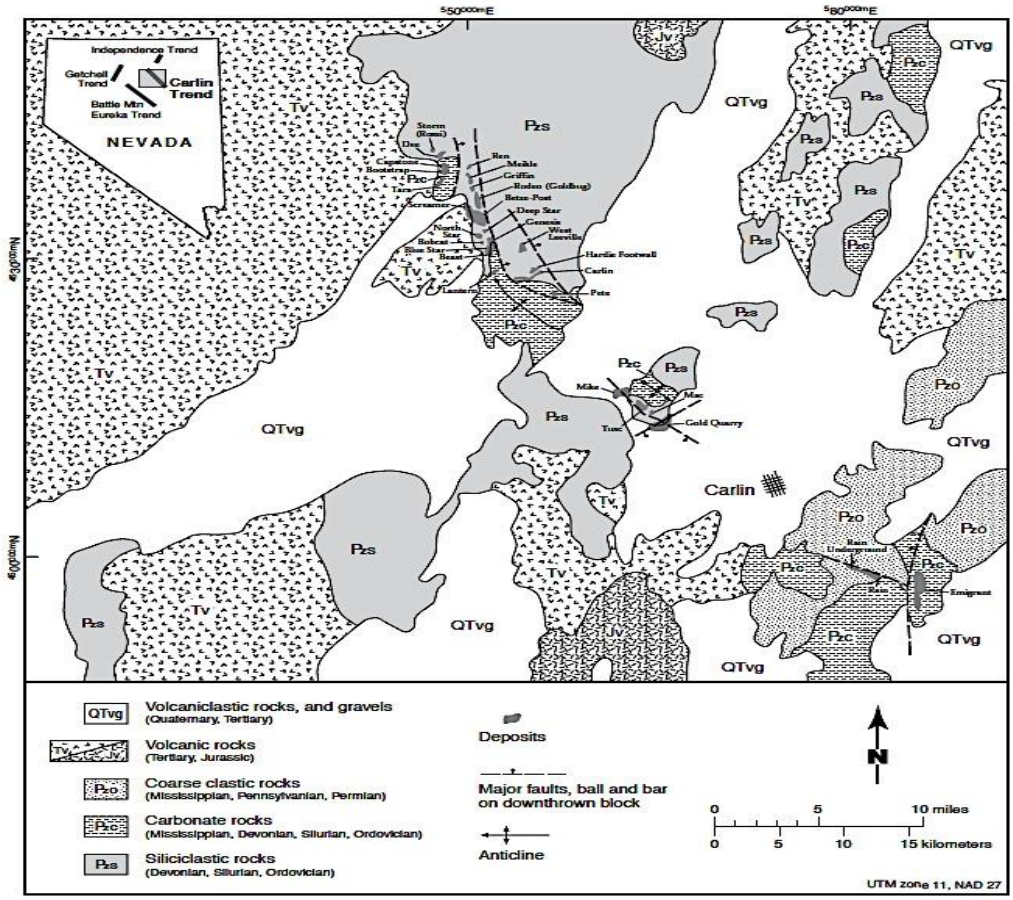

Figure 1.1. Simplified geological map of the Carlin Trend, Nevada, USA. (*After Teal and Jackson, 2002).*

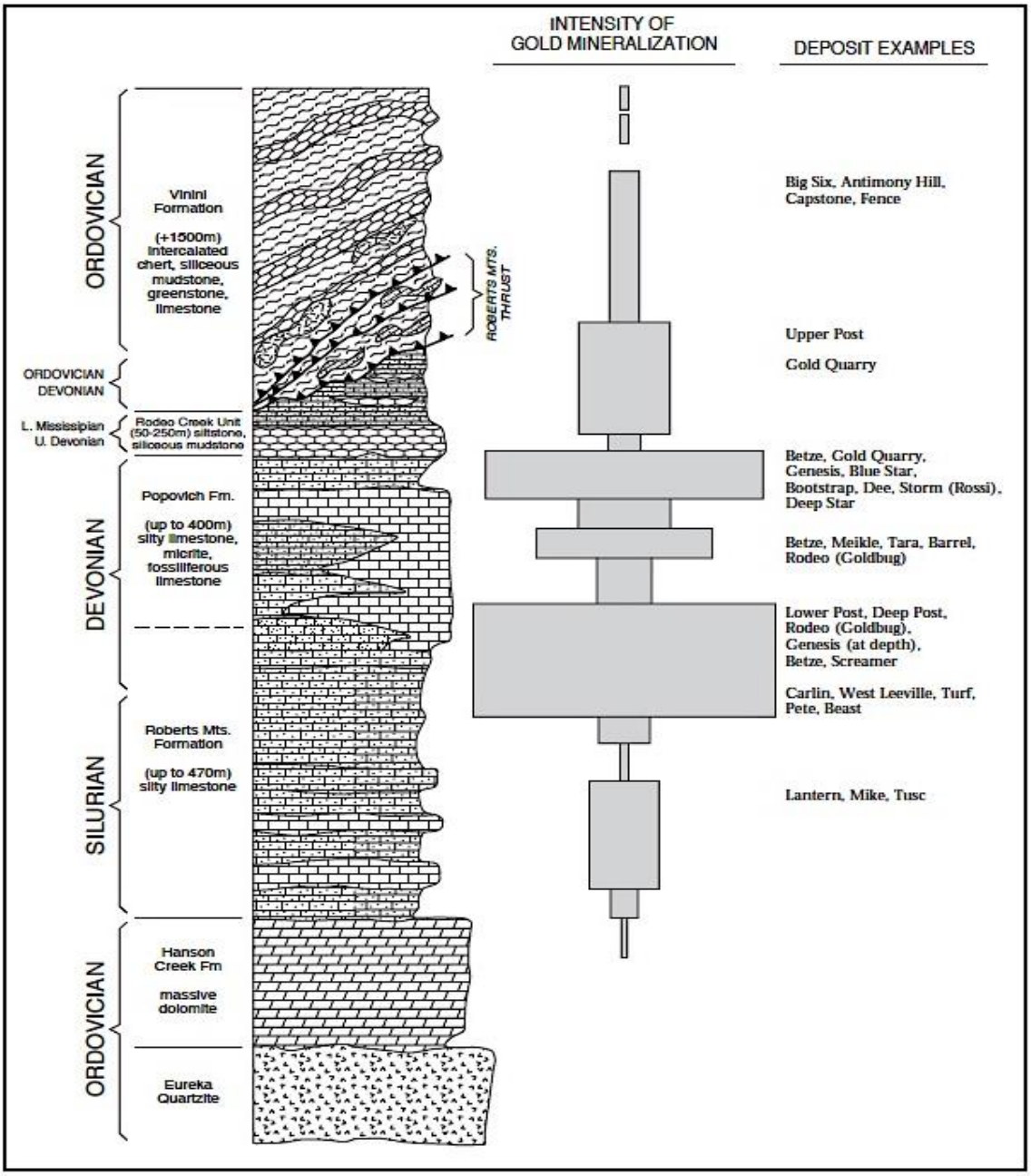

Figure 1.2. Idealized stratigraphic column and gold mineralization, northern and central Carlin Trend, Nevada. *(After Teal and Jackson, 2002)*.

STRUCTURAL CONTROLS OF GOLD DEPOSITION

Gold mineralization in most deposits occurs as structurally strata bound horizons. The north-northwest alignment of the Carlin Trend is a combination of structural features along crustal weakness due to progressive extension and periodic high heat flow by multiple intrusive episodes.

There are some common structural features on a regional scale (Teal and Jackson, 2002):

- High-angle N-NW and NE striking faults
- Anticlinal folding in autochthonous carbonates
- Collapse breccia bodies

Faults

High-angle, north-northwest striking faults are the primary fluid conduits for gold deposition in every sub-district in the Carlin Trend (Teal and Jackson, 2002). Individual fault zones range from 50 m to 800 m, characterized by complex kinematics, and multiple stages of normal, oblique, and apparent strike-slip movement, mostly dike filled within or proximal to gold deposition. High-angle northeast trending faults served as a secondary fluid conduit for gold mineralization, especially at intersections of north-northwest trending faults.

Folds

Northwest trending, broad to moderate amplitude, anticlinal folds had an important role as structural fluid traps during fluid migration within regional and deposit scale. It has been proposed that the autochthonous carbonate sequence is part of a regional north-northwest trending anticline that extended from the Gold Quarry deposit to the Genesis deposit. Gold deposits of the north-central and south-central Carlin Trend occur in the northeast and southwest limbs of the anticline (Teal and Jackson, 2002). On deposit scale, moderate amplitude, northwest trending anticlinal folds have been observed to control the high-grade gold mineralization. The folds are interpreted to form as a result of compressive shortening related to pluton emplacement (Leonardson and Rahn, 1995) that subsequently served as a structural trap for fluids that were ponded adjacent to the intrusive contact. In other deposits, such as the Upper and Lower Post deposit, anticlinal folds localize stratiform gold mineralization along the crest of the fold. At the Genesis deposit, high-grade ore mineralization is localized in the hinge zone of the NNW trending Tuscarora anticline (Schutz and Williams, 1995).

Pre-Ore Stage Breccia Bodies

The formation of pre-ore stage, high-angle, stratabound, heterolithic breccia bodies played an important role within many individual deposits, because they enhanced permeability at the contact zones for subsequent gold bearing fluids to transit of otherwise unreceptive host rocks. These pre-ore, heterolithic, localized dissolution breccias are believed to form as a consequence of decarbonatization and collapse of

carbonate rocks due to hydrothermal fluids (Teal and Jackson, 2002). High-grade gold mineralization is also described along sedimentary debris flow horizons of the Upper Popovich and Lower Roberts Mountains Formation that mark the transition of carbonate facies from massive, unreceptive, fossiliferous limestone to more permeable, micritic, silty limestone (Leonardson and Rahn, 1995).

ALTERATION

The pervasiveness and intensity of alteration in Carlin-type deposits varies within and between gold deposits; however, there are some common salient features that characterize Carlin-type deposits that include: silicification, carbonate dissolution, and argillic alteration (Teal and Jackson, 2002; Cline et al., 2005). It has been suggested that the reactions that formed Au-bearing pyrite are not the same reactions that formed alteration minerals (Hofstra et al., 1991), thus the lack of temporal and spatial relationship between ore and alteration minerals limits the use of alterations to identify ore zones (Teal and Jackson, 2002).

Silicification

The extent of silicification varies between deposits and strongly depends on the properties of the protolith. Silicification is manifested by the presence of jasperoids, quartz filled vugs, or ore-stage quartz veins. Jasperoids range from barren to high-grade ore mineralization. The size of these jasperoids is strongly dependent on the protolith; pure limestone protolith produces massive, several metres scale, jasperoids. In contrast, limey siltstones and sandstones form micro to few cm scale

jasperoids. Some jasperoids display characteristics chalcedonic, opaline silica, and jigsaw textures. Furthermore, drusy quartz filled vugs are a characteristic feature of Carlin-type deposits (Cline et al., 2005). In general, more than one stage of silicification is observed. Gold bearing pyrite occurs within both jasperoids and quartz vugs (Cline, 2001; Lubben, 2004).

Carbonate Dissolution

Carbonate dissolution in the form of decalcification and decarbonatization is the most pervasive style of alteration observed within the Carlin Trend. The extent of carbonate dissolution mostly depends on the original composition of the host rock. This pre-ore stage alteration causes a loss in density, and an increase in permeability and porosity of the host rock, providing a depositional pathway for auriferous fluids. The decarbonatized host rock is locally replaced with quartz to form jasperoids. Some decarbonatized zones show zoning patterns, such as the appearance of dolomite first, followed by calcite (Cline et al., 2005). Other carbonate minerals such as ankerite, siderite, and dolomite are also common. The extent of decarbonatization does not necessarily indicate higher gold grades (Teal and Jackson, 2002).

Argillic Alteration

Argillic alteration is particularly well developed in silty limestone, and in calc-silicate hornfels protoliths; however, it is minimal in carbonate rocks. Original K-feldspars and detrital clays are commonly altered to kaolinite, illite, and sericite.

GOLD MINERALIZATION

Gold in Carlin deposits commonly occurs as submicron domains (50-200 Å) within the lattices of pyrite and arsenian pyrite (Teal and Jackson, 2002). Fluid inclusion studies indicate that aqueous fluids contained CO_2 (4 mol %), and CH_4 (0.4 %) and sufficient H_2S (10^{-1}- 10^{-2}) that gold was transported as Au bisulfide complex at low salinity (7-10% NaCl) (Kuehn, 1989; Hofstra, 1991; Cline et al., 2005). The depth of formation for Carlin-type gold deposits is estimated between 4.4 ± 2.0 km at a low- to moderate temperature of 180-245 °C based on microthermometry of CO_2-rich fluid inclusions (Kuehn, 1989).

Deposit Mineralogy

Deposit mineralogy and geochemistry reflects a strong association of Au with As, Sb, Tl, and Hg. Most Au was deposited with main ore-stage minerals including Au-bearing arsenian pyrite, marcasite, quartz, kaolinite, illite, dickite, and local orpiment (Cline et al., 2005). Pre-ore stage framboidal and coarse-grained, usually cubic, pyrite has a disseminated, unzoned texture. Au-bearing ore-stage arsenian pyrite occurs generally as anhedral to euhedral grains with diameters of 10- 30 μm or as narrow rims of a few hundred μm on earlier formed framboidal or As-poor euhedral, cubic pyrite both largely diagenetic in origin (Simon et al., 1999; Cline et al., 2000). Where ore-stage orpiment occurs micrometer-sized arsenian pyrite inclusions occur within the orpiment. Ore-stage minerals are fine-grained in comparison to relict host-rock minerals such as quartz, dolomite, pyrite, and other clay minerals (Cline and Hofstra, 2000). Arsenian pyrite is only present in ore-stage

mineralogy. Macroscopic, late ore-stage minerals generally occur in voids or cross-cutting fractures and are generally dominated by orpiment, realgar, calcite, dolomite, stibnite, marcasite and pyrite. Realgar and calcite are interpreted as the latest post-ore minerals. Other minerals present in some but not all deposits include cinnabar, fluorite, sphalerite, and tellurides (Cline and Hofstra, 2000). Recent studies with secondary ion mass spectrometry (SIMS) confirmed that arsenian pyrite is the only significant gold host in Carlin-type deposits. These studies suggest that the highest gold content correlates with pyrite having the smallest grain size and that arsenian pyrite with overgrowth textures has relatively higher gold content than pyrite with zoned textures (Simon et al., 1999).

GENETIC MODELS

The continuously evolving database and the characteristic features in Carlin-type gold deposits have not yielded a widely accepted genetic model. The hypotheses for Carlin-type gold deposits fall into two general groups: (I) magmatic fluid origin and (II) amagmatic fluid origin. The amagmatic fluid origin can be interpreted further to involve three modes of fluid origin: 1., metamorphic, 2., meteoric, and 3., sedimentary exhalative. These categories are discussed in detail and summarized in Table 1.1 below.

(I) Magmatic fluid source

<u>Deep magmatic-hydrothermal model</u>

The deep magmatic hydrothermal model suggests that Carlin-type deposits are distal portions of magmatic hydrothermal systems, where the circulating hydrothermal fluids are driven by the magma, which is also the source for both metal and fluid components (Radtke et al., 1980). In this model, the development of high Au/Cu magma is derived from a long-lived east-dipping subduction zone along western North America in the Middle Triassic. Back-arc magmatism, along with slab dehydration, hydrated and metasomatized the subcontinental lithospheric mantle with metals including As, Sb, Tl, Pb, and Cu. The rollback of the subducting slab renewed magmatism and exposed the metasomatized subcontinental lithospheric mantle to upwelling asthenosphere, providing large volumes of CO_2, Cl, S, and Au bearing mafic magma, which partially melted the continental crust. A compositionally different, hydrous, high K, calc-alkaline, S- and Au-bearing magma of intermediate composition was formed. As this newly formed magma ascended, it reached volatile saturation releasing a single phase CO_2, H_2S and Au bearing aqueous fluid with high Au/Cu ratio. In the Carlin Trend, six individual igneous suites were emplaced during the Eocene that apparently stalled at a depth of 10 km. The above mentioned single phase, H_2S rich, high Au/Cu ratio aqueous fluid was consequently tapped during the reactivation of basement structures by a series of compressional events during late Devonian to Early Mississippian. During the ascent, ore fluids separated into a brine and vapour phase, where a significant amount of Au was

transported by the vapour and Fe by the brine. In this magmatic origin theory, the precipitation of Au is explained by the encounter of meteoric water as the low-salinity Au-bearing vapor phase rose through the upper crust. Fluid inclusions found in ore-stage quartz and kaolinite indicate an ore fluid of 250 °C with 2-3 wt % NaCl consistent with meteoric fluids. This strongly suggests the titration of the original gold bearing magmatic fluids with meteoric water (Muntean et al., 2011).

(II) Amagmatic fluid source

<u>1. Metamorphic model</u>

Fluids associated with the Carlin-type gold deposits share characteristics with the metamorphic fluids implicated in orogenic gold deposits (GQC). Orogenic gold fluids are characteristically low salinity (<3 wt% NaCl), moderate pH, high CO_2 content, and 350±50°C. Gold is transported as $Au(HS)^-_2$ or Au(HS) complexes. Isotopic data and fluid inclusions indicate that gold in Carlin-type gold deposits was also transported as Au bisulfide complex in fluids of low salinity (7-10 wt % NaCl) with moderate pH and high CO_2 content (Kuehn, 1989; Hofstra, 1989). Furthermore, many orogenic gold deposits lie along regional fault systems, similar to the 60 km long structural zone along the Carlin Trend. The metamorphic model implies that hydrothermal fluids were generated by deep, possibly mantle derived magmatic or metamorphic activity that preceded crustal extension and provided enough heat to circulate fluids (Seedorff, 1991), which then moved upwards along regional fault systems. These fluids reacted with carbonate host or country rocks and inherited

CO_2, H_2S and H_2O from the devolatization reaction of metasedimentary rocks, along with sulphur and metals (Ilchik and Barton, 1997). In addition, the $\delta^{34}S$ values in Carlin deposits derived from the Paleozoic sedimentary rock are consistent with orogenic models where H_2S is also inherited from metasedimentary rocks (Emsbo et al., 2003). The high CO_2 and trace H_2S content leads to the decarbonatization of host rock and increases permeability. As permeability was increased, and fluid-rock reaction continued, the sulphidation of host rock iron lead to the precipitation of gold and arsenic bearing pyrite. Further fluid-rock reactions and faulting allowed cooler meteoric fluids into the system, which led to a decline in fluid temperature and caused the precipitation of ore-stage gangue minerals (Cline and Hofstra, 2000). However, many inconsistencies exist; light δD values, indicative of predominantly meteoric fluids, and the absence of mid-Tertiary regional metamorphism are some of the major problems with this theory.

2. Meteoric water model

The meteoric water model is based on some of the similarities between Carlin-type gold deposits and low sulphidation epithermal gold deposits. Epithermal gold deposits form in extensional terranes at a shallow depth (<1000 m), characterized by the low temperature (50-200 °C) of ore fluids, dominated by a meteoric water system that's driven by volcanic heat. The meteoric water model calls upon the lateral flow of meteoric fluids that were circulated by the heat flow during crustal extension in the mid-Tertiary (Cline et al., 2005). This model suggests that no igneous activity is necessary for Carlin fluids, due to the lack of strong association

with contemporaneous igneous activity (Ilchik and Barton, 1997). In this hypothesis, hot, deeply buried rocks were brought to the surface during the crustal extension of the Great Basin, which raised the geothermal gradient. Later compressional events increased the permeability of rocks, enhancing fluid circulation. Meteoric fluids are suggested to have circulated to a depth where metals, sulphur, silica and gold were scavenged from the sedimentary rocks and then deposited into favorable environments during the fluid ascent (Ilchik and Barton, 1997). This amagmatic hypothesis seems supported by both isotopic data and geochemical signature. Ore fluids show low δD values reflecting meteoric origin and the similar geochemical trend of elevated Au, As, Sb, Hg, and Tl in low sulphidation, ADS-type epithermal gold deposits suggest a strong similarity between meteoric water dominated epithermal ADS-type and Carlin-type gold deposits. This model, however; does not account for the presence of deeply sourced, magmatic or metamorphic water identified in some Carlin districts (Cline et al., 2005) and for the fact that deep circulation of meteoric water commonly results in high concentration of SiO_2 and widespread precipitation of quartz, which is not found in ore-stage Carlin-type gold deposits (Emsbo et al., 2003)

3. SEDEX model

In another variation of the amagmatic fluid model, the presence of auriferous sedimentary exhalative mineralization in the local stratigraphy suggests the contribution of pre-existing gold to Carlin-type deposits (Emsbo et al., 2003). In this model, ore fluids are derived from meteoric water that evolved into ore fluid by

shallow circulation through gold and sulfur enriched rocks. Gold is suggested to source from pre-existing sedimentary exhalative sulphide deposits; i.e., meteoric fluids interacted with sedimentary rocks that provided the pre-enrichment of gold and associated trace elements. The interaction between these gold hosting, pyritic, carbonaceous sedimentary rocks and the heated meteoric water generated H_2S-rich fluids, which suppressed the solubility of base metals and deposited auriferous pyrite into reactive, Fe-rich, permeable rocks during the migration of fluids (Emsbo et al., 2003). This hypothesis, however, is not compelling for several reasons. Auriferous enrichment of sedimentary exhalative mineralization is uncommon, and thus restricts Carlin-type gold mineralization to a specific local stratigraphy, which does not readily explain the emergence of other Carlin–like gold deposits in other places in the world (China, Mexico, and Canada). Furthermore, this theory fails to prove if there was sufficient gold introduced by SEDEX hydrothermal system to account for known gold inventory of the Nevada deposits.

Table 1.1. Summary of genetic models of Carlin-style gold deposits.

	MAGMATIC FLUID SOURCE	AMAGMATIC FLUID SOURCE		
		METAMORPHIC FLUIDS ORIGIN	METEORIC FLUIDS ORIGIN	SEDEX ORIGIN
FLUID SOURCE	Magmatic hydrothermal fluids	Metamorphic fluids implicated in orogenic gold deposits	Meteoric fluids	Evolved meteoric ore fluids
DRIVING FORCE OF FLUIDS	Magma	Deeply sourced metamorphic heat	Volcanic heat	Orogenic event
METAL SOURCE	Magma	Metasedimentary rocks	Sedimentary rocks	Pre-existing SEDEX deposit-sedimentary rocks
TECTONIC SETTING	Subduction zone with back-arc magmatism and slab dehydration	Crustal extension and regional fault system	Extensional terranes at shallow depth	Rifting environment second-order basins
PROCESSES	**1.**Metasomatized lithospheric mantle partially melts the continental crust **2.** Newly formed magma reaches volatile saturation with a single phase Au-bearing aqueous fluid **3.** Ore fluids separate into vapour and brine, where Au partitions into vapour	**1.** Hydrothermal fluids generated by metamorphic activity reacts with country rocks and inherit CO_2, H_2S, H_2O along with metals and sulphur **2.** High H_2O and H_2S content leads to decalcification of host rock increasing permeability **3.** Fluid-rock reaction	**1.** Hot, deeply buried rocks are brought to the surface during crustal extension, which raises the geothermal gradient **2.**Compressional events increase permeability and enhance fluid flow **3.**Meteoric fluids circulate to a depth and scavenge metals from sedimentary rocks	**1.** Meteoric fluids circulate through gold and sulphur enriched rocks. **2.** Heated meteoric water interacts with pyrite-rich carbonaceous host rocks 3. Heated meteoric water generates, H_2S-rich fluids which suppresses the solubility of

	MAGMATIC FLUID SOURCE	AMAGMATIC FLUID SOURCE		
		METAMORPHIC FLUIDS ORIGIN	METEORIC FLUIDS ORIGIN	SEDEX ORIGIN
		precipitates gold and arsenic **4.** Faulting allows cooler meteoric fluids into the system, which precipitates ore-stage gangue minerals		base metals 4. Auriferous pyrite is deposited into reactive, Fe-rich, permeable host rocks
AU PRECIPITATION/ DEPOSITION	Encounter of meteoric fluids, titration of Au-bearing magma with meteoric fluids	Fluid-rock reactions precipitate gold	Gold is deposited into favorable environment during fluid ascend	Gold is deposited during the migration of fluids
EVIDENCE	**1**. O and H isotopes indicated 250 °C with 2-3 wt % (consistent with meteoric fluid values) **2.** Igneous Jurassic and Cretaceous plutons are present in the Carlin Trend	**1.** $\delta^{34}S$ values in Carlin deposits derived from the Paleozoic sedimentary rock are consistent with orogenic models **2.** In orogenic gold deposits gold is transported as $Au(HS)^{-}_{2}$ or Au(HS) complexes same as in CTGDs **3.** Orogenic fluids are low salinity, high pH with high CO_2 content	**1.** Low δD values reflecting meteoric origin **2.** Similar geochemical trend. Elevated Au, As, Sb, Hg, and T in CTGDs is similar to geochemical trends in epithermal ADS-type deposits.	**1.** Theory explains local base metal signatures of certain deposits **2**. Low δD values reflect meteoric origin

	MAGMATIC FLUID SOURCE	AMAGMATIC FLUID SOURCE		
		METAMORPHIC FLUIDS ORIGIN	METEORIC FLUIDS ORIGIN	SEDEX ORIGIN
		similar to Carlin fluids		
PROBLEMS WITH THE THEORY	**1.** Theory fails to explain low δD values. **2.** Plutons and mafic dikes in the Carlin Trend are not gold mineralized	**1.** Light δD values, indicative of predominantly meteoric fluids are not explained by this theory	**1.** Deeply sourced, magmatic or metamorphic water identified in some Carlin districts are not explained by this model **2.** Deep circulation of meteoric water results in high concentration of SiO_2 and widespread precipitation of quartz, which is not present in ore-stage Carlin-type gold deposits	**1**. Auriferous enrichment of sedimentary exhalative mineralization is uncommon **2.** Data does not explain if there was sufficient gold in the SEDEX deposit to account for the present values in Nevada

CARLIN-STYLE GOLD MINERALIZATION IN THE YUKON TERRITORY, CANADA

INTRODUCTION

Carlin-type gold deposits (CTGDs) have been tentatively reported in many locations worldwide (China and Mexico); however, the majority of deposits have been restricted to the Great Basin in Nevada, United States. Recent discoveries in the east-central Yukon show many of the same characteristics as the Nevada CTGDs. The Nadaleen Trend within the Rackla Belt of east-central Yukon, Canada holds promise of great potential for new discovery of Carlin-type gold deposits. In the Nadaleen Trend, an area of 4 by 2.5 km contains gold mineralized zones know as Conrad, Osiris, Isis, Amon, Anubis, and Sunrise owned by ATAC Resources Ltd. The discovery of potential Carlin-type gold deposit was made by ATAC Resources LTD. on the Conrad Zone in the summer of 2010 during the follow up of high arsenic anomalies in the stream sediments. ATAC Resources Ltd. expanded the discovery with a diamond drill intersection of 18.44 g/t Au over 42.93 m in 2012 (ATAC Resources LTD., 2012a). The clustered nature of mineralized zones and showings on the ATAC property underlines the metallogenic potential of the Nadaleen Trend.

REGIONAL GEOLOGY

Sedimentary Host Rocks

The Rackla Belt lies at the apical junction of the Neoproterozic–Permian rocks of Selwyn Basin and the Proterozoic–Paleozoic Ogilvie Platform along the east-west trending Dawson Thrust Fault (Figure 1.3). The Nadaleen Trend is in the eastern part of the Rackla Belt, at the interface between the Selwyn Basin and Neo-Mesoproterozoic basement rocks of the Windermere Supergroup (Figure 1.4). Gold mineralization is now recognized within the carbonate sequences throughout the trend in association with realgar and orpiment, and locally decarbonatized and silicified rocks (Arehart et al., 2013). Carlin-type gold mineralization within the Nadaleen Trend is hosted by the Neoproterozic to Lower Cambrian Hyland Group and the Ediacaran Gametrail and Nadaleen Formations (Moynihan, 2014).

REGIONAL STRUCTURES

The Nadaleen Trend is structurally bounded by the Dawson Thrust to the south and by the Kathleen Lakes Fault to the north (Figure 1.4). The Dawson Thrust is a north-northwest striking regional structure that is believed to have been reactivated during the Neoproterozoic (Moynihan, 2014). The Kathleen Lakes Fault is suggested to represent a basement structure that may have been reactivated during the Tertiary Period (Moynihan, 2014). The Nadaleen Trend itself is structurally complex. However, the major structure that seems to control gold mineralization on a property scale is the east trending Nadaleen Fault (Moynihan, 2014).

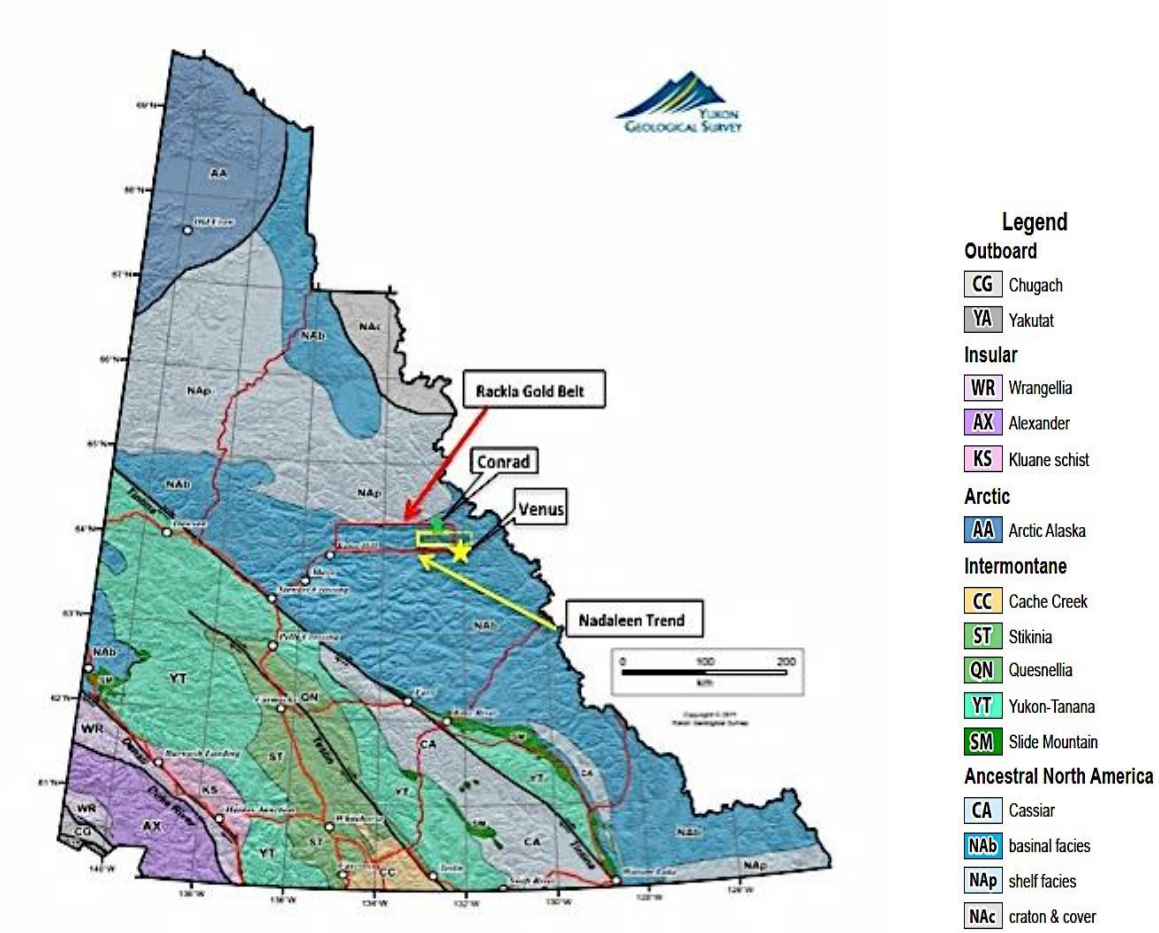

Figure 1.3. Terrane map of Yukon showing the Rackla Gold Belt and Nadaleen Trend (Modified after Yukon Geological Survey, 2011).

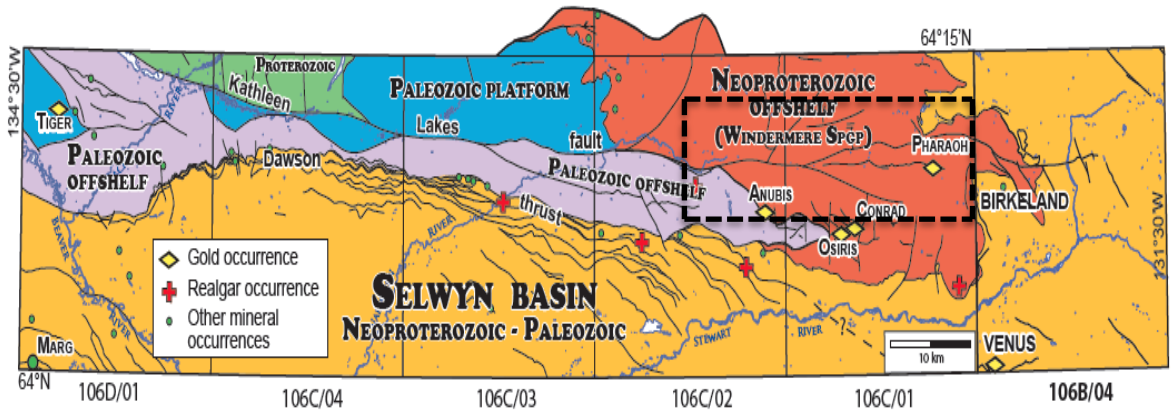

Figure 1.4. Geological map of the Rackla Belt showing the facies domains, major structures, and mineral occurrences. The black frame outlines the Nadaleen Trend (*Modified after Colpron et. al., 2013).*

PROPERTY GEOLOGY-CONRAD ZONE

The Nadaleen Trend at the Conrad Zone consists of southward younging sequences of sedimentary packages. The Conrad Zone contains silty limestone, siltstone with local carbonate debris flows, and hydrothermal dolostone, which are in fault contact with an argillaceous mudstone package to the north. The gold mineralized zones are mainly within the massive, silty, laminated Conrad limestone and the Conrad siliciclastic rocks consisting of siltstones and sandstones with lenses and interbeds of quartz-granule conglomerate. The limestone unit is intruded by mafic gabbroic dikes along the faults that are proximal to gold mineralization. These dikes show sericite alteration, abundant pyrite, and trace realgar mineralization; however, this may represent pre-ore stage mineralization (Tucker et al., 2013).

Structural controls on gold deposition

The most prominent structure is the Nadaleen Fault that separates the Osiris and the Conrad strata. The area is also defined by two large-scale antiforms that plunge steeply to southwest. These two antiforms are separated by an E-W trending, dextral strike-slip fault. The Conrad strata are complexly folded, with the Conrad limestone at the core of the antiform trending north-northeast (Tucker et al., 2013).

Alteration

There are two main alteration types associated with gold mineralization in the Conrad Zone (Tucker et al., 2013): 1. Decarbonatization of host limestone is the most pervasive alteration in the Conrad Zone. This is manifested in a very fine

grained, black, sooty material in the form of styolites. These styolites are observed near the gold mineralized areas, and compromise fine silt and carbonaceous material; and 2. Silicification occurs synchronously with decarbonatization. Areas of mineralization are dominated by the complete replacement of carbonate by silica matrix. Large-scale jasperoids are not common in the Conrad Zone.

GOLD MINERALIZATION

Visible gold is not present in the Conrad Zone. Realgar and orpiment are key spatial indicators for gold mineralization; however, they form from post-mineralizing fluids. Arsenian sulphides such arsenopyrite and scorodite are common in silicified and brecciated zones. Locally, small stibnite veins are present in the siliciclastic units, although not always indicative of gold mineralization (Tucker et al., 2013).

AIMS AND OBJECTIVES

The main objective of this project was to compare the Venus Zone, Einarson property located in the Nadaleen Trend, Yukon Territory to Carlin-type deposits and environments in Nevada, and to determine whether the geological setting and mineralogical characteristics of Au-bearing occurrences in the Venus Zone resemble those characteristic of Carlin-style gold mineralization. Thin section analysis, Scanning Electron Microscope with Energy Dispersive X-Ray Analyzer (SEM-EDX), and a compilation of field and exploration geochemical data were used to further elucidate the ore paragenesis, deportment and localization of gold mineralization in the Venus Zone. This forms the basis for the comparison of this example, within an emerging gold district in the Northern Cordillera, with the classic examples and characteristics described from the Nevada districts of Carlin-style mineralization.

CHAPTER 2

APPROACH & ANALYTICAL METHODS

APPROACH

FIELD WORK

In preparation for this thesis, 12 days were spent from August 18th to 31st, 2013 on the Venus Zone, Einarson Property with the main objective of detailed mapping of the mineralized areas. The detailed maps included three 1:1000 scaled maps along three drill hole section lines within the three zones (main, northeast, and central) of Venus. An additional 1:500 scaled map was added to the northeast zone of Venus to gain a better understanding of the structural patterns and the newly discovered mineralized host lithologies. Assay samples were taken to locate potential gold bearing zones.

5 days were spent from September 1st to 6th, 2013 re-logging, DH-12-05 (main zone), DH-13-14 (northeast zone), and DH-13-12 (central zone) drill holes including lithological, structural, and mineralogical observations. Samples were taken from the drill core for thin sectioning to identify mineralized and unmineralized zones.

LABORATORY WORK

Detailed petrographic analysis was carried out on 32 thin sections taken from both drill core and rock samples using a Nikon Eclipse Microscope to establish ore mineral paragenesis and to recognize potential favorable host lithologies.

Ten samples were further analyzed using a Scanning Electron Microscope with Energy Dispersive X-Ray Analyzer (SEM/EDX) with the aim to further elucidate

paragenesis and Au deportment. This work was performed in the MAF-IIC Facility at Memorial University of Newfoundland using an FEI MLA 650 FEG model SEM equipped with Bruker XFlash 5030 EDX detectors and Bruker Esprit Quantax v.1.9 software for spectral analysis.

As well, commercial geochemical assay data from rock chip and channel samples were plotted and interpreted to gain a better understanding of the spatial association of gold and Carlin pathfinder elements, as well as to clarify and elucidate the utility of elevated base metal associations for exploration.

ANALYTICAL METHODS

SEM/EDX & BSE

Introduction

SEM/EDX stands for Scanning Electron Microscopy with Energy-Dispersive Analysis of X-Ray Spectroscopy. SEM/EDX instruments utilize an electron beam, which is passed over the sample surface and causes energy changes in the surface layer of the specimen. These changes are detected and analyzed by the spectrometer to produce an image and to identify and characterize the elemental composition, morphology, and size of solid materials. Areas of 1 cm to 5 micron can be imaged with an approximate magnification ranging between 20X to 30,000X with a 50-to 100 nm lateral spatial resolution (Goldstein, 2003).

Principles

The principal of SEM/ EDX microscopy is based on the emission of the primary electron beam by an electron gun, which induces a number of effects on the

surface of the specimen. These effects result from the interaction between the primary electrons and the sample and they are received as various signals by the microscope. The SEM/EDX microscope is equipped with 3 detectors, which can analyze these various signals: 1) Back-scattered electron (BSE), 2) Secondary electron (SE) and 3) Energy Dispersive X-ray (EDX) detector.

Back-scattered electrons (BSE) are produced as result of elastic collision with the atom of the sample when the beams of electrons are scanned over a square area and reflected back from the sample by scattering. The intensity of the BSE signal is strongly dependent on the average atomic number (Z) of the given sample. The number of back-scattered electrons produced increases with increasing atomic number. Therefore, minerals with higher average atomic numbers will produce more back-scattered electron and they will appear brighter.

The secondary electron detector (SE) measures the secondary electron emission signal by scanning over a square area to acquire the spectral analysis. Secondary electrons are produced when an electron from the primary beam collides with an electron of a specimen atom near surface. During the collision, the electron of the primary beam loses energy to the other electron, which ionizes the atom. In order to re-establish the proper charge ratio an electron is emitted, and it's referred as secondary electron. Secondary electron signal can resolve surface structures in details less than 1 nm and it can produce high-resolution images with a 3 dimensional appearance (topography) (Goldstein, 2003).

The Energy Dispersive X-ray spectroscopy uses a finely focused beam of electrons to excite elemental electrons within the sample to a higher energy state. Electrons from the inner shell are displaced by collision with the primary electrons, which leaves a vacancy in the atom's electronic structure. This forces electrons from higher energy state to fill the lower energy vacancies until the atom regains its original minimum state. As higher energy electrons transition to lower levels they emit X-rays. This emitted X-ray is measured by the spectrometer. Each element has a different nuclear charge and spacing between the shells, which then can be detected and identified by the spectrometer based on its energy. As the spectrometer detects the X-rays, characteristic peaks are displayed for each element and their elemental position are recorded or "mapped" within the given mineral specimen (Piburn and Barron, 2013).

All data for this study were acquired using standard conditions of 25 keV electron beam energy and approximately 10nA of primary beam current focused in a 5-6 μm spot on the sample.

Sample preparation

Thin sections must be additionally prepared for X-ray spectroscopy in order to ensure a good image quality. The samples are first covered with a thin coating. This coating serves multiple purposes such as increased conductivity, mechanical stability, and reduction of thermal damage. Carbon coating is often used because of its low atomic number, which increases conductivity without sacrificing compositional information by alternating X-rays (Goldstein, 2003). Furthermore, samples must have a flat, polished surface and must be stable under vacuum

since the chamber is evacuated to prevent the interference between the atmosphere and the X-Rays (Piburn and Barron, 2013).

Advantages

The SEM/EDX microscope has many advantages over other microscopes. SEM/EDX microscopes reveal a great deal of information about solid materials including composition, topography, size, and morphology in only one application. Data acquisition is rapid for all SE, BSE and spot EDS, which can be generated in digital formats. Furthermore, while the characterization of solid materials is mainly concerned with geology related applications, the SEM/EDX analytical methods are broadly used in other scientific fields.

Limitations

SEM/EDX can only analyze solid material that can fit into the microscope chamber. Therefore, generally larger sized and "wet" samples such as rocks saturated with hydrocarbons are not suitable for SEM analysis. The EDX detector cannot detect the lightest elements, typically below the atomic number of Na, thus some elements that fall behind this criteria remain undetectable during the analysis. Furthermore, the energy peaks of some elements overlap, which in some instances makes it difficult to identify the specific element. To eliminate these issues many spectrometers is equipped with Wavelength Dispersive X-Ray variants (WDS), which can identify the separate peaks more accurately. The region of the specimen where back-scattered electrons are produced is considerably larger than it is for secondary electrons, because during collision the electrons spread out over an area, which results in lower resolution of back-

scattered electron image than the images produced by the SE. BSE images are also restricted to comparative gray-scale because they only record the average atomic number, thus they do not show as much information as it can be obtained form the EDX elemental maps (Goldstein. 2003).

GEOCHEMISTRY

Introduction

During the 2013 field season, 452 rock chip samples were collected across the Venus Zone and assayed by AGAT Laboratories using a geochemical exploration package. This type of package included a 19 multi-element (As, Ag, Au, Be, Bi, Co, Cu, Fe, Hg, Ga, K, Ni, P, Pb, Sb, Se, Te, Tl, Zn), geochemical assay with fire assay for Au and induction-coupled plasma-mass spectrometry (ICP-MS) finish. The fire assay method was chosen because it gives a reproducible, quantitative measure of gold values. Furthermore, the National Instrument 43-101 and other technical reports generally require the reporting of gold values determined by fire assay method. The aqua regia digestion in combination with ICP-MS was used to determine geochemical anomalies. In the 19 multi-element package, Hg poses special analytical challenges, because it may be partially or completely volatized by high-temperature digestions and it causes interference issues with argon molecules during the ICP-MS analysis. These issues can be avoided by specific sample preparation and preservation techniques and by the utility of certain ICP-MS that most laboratories include in their services.

Sample preparation

All rock chip samples were weighted, photographed, and identified with a special barcode before sample shipment for traceability and security purposes. Before geochemical analysis, all samples were prepared to produce a small, representative homogenous sub-sample from the submitted material. The rock chip sample preparation included jaw crush to reduce sample particle size prior to pulverization, which was followed by a riffle split and a pulverize split. After pulverization, the homogenous sub-sample is ready for geochemical analysis.

Fire Assay method

A fire assay method was used to determine gold values, because it gives a high-quality, reproducible, quantitative measure of gold. The fire assay method mixes the pulverized rock with certain fluxes and a carbon source, which then is heated to 1000-1200 °C inside an electric furnace. The carbon source reduces lead oxide in the flux to lead, which alloys with any precious metals in the sample, whereas, the fluxes combine with the crushed rock forming a glassy slag. After fusion the sample is poured into a mold, where the glassy slag floats to the top and the lead alloy coupled with precious metals sink to the bottom. After solidification, the lead bullet is further processed by cupellation, where it is placed into porous crucibles made of MgO and heated to a 1000 °C. As the lead melts and oxidizes it fills the pores of the crucible, whereas the precious metals remain at the base for final analysis of precious metal content-usually by gravimetric finish or by inductively coupled plasma spectrometry (ICP-MS).

Aqua Regia method

Aqua regia dissolution with ICP-MS finish was used to determine the 19 other elements listed above. The aqua regia method readily dissolves sulphides, oxide and carbonate minerals, while silicates, resistive oxides, and many volatile pathfinder elements, particularly mercury are preserved during digestion. Gold results obtained by this method will generally show lower values than by fire assay (Hoffman and Clark, 1999). Aqua regia is a mixture of hydrochloric and nitric acid that dissolves the mineral matrix and holds the metals in solution. Once the digestion is completed, a solvent is added to the solution, which collects the precious metals. This solution is then subjected to analysis by inductively–coupled plasma mass spectrometry (Hoffman and Clark, 1999).

Induction-Coupled Plasma-Mass Spectrometry (ICP-MS)

The inductively coupled plasma spectrometry (ICP-MS) analytical technique was used for elemental determination of the rock chip samples. This analytical technique is widely used in geochemical laboratories because of its multi-elemental capabilities in comparison to other traditional elemental techniques. The ICP source converts the atoms of the elements into ions, which are then separated and detected by a mass spectrometer. Samples are typically introduced to the ICP as an aerosol, which is achieved by aspirating the dissolved solid sample. Once, the sample is desolvated, the elements are converted into gaseous atoms and then become ionized. These ions are brought into the mass spectrometer via cones and then separated by their mass-charge ratio, where the ICP-MS identifies the elements based on their isotopic peaks (Wolf, 2005). The

most commonly used type of mass spectrometer is a quadrupole mass filter, in which alternating AC and DC voltages are applied to the opposite pairs of the rods and then rapidly switched along with an RF field. This process results in an established electrostatic filter that only allows ions of a single mass-to-charge ratio to pass through the rods to the detector at a given time. The ability to filter ions based on their mass-charge ratio also allows the discrimination of isotope ratios since different isotopes of the same element have different masses (Wolf, 2005).

Geochemical plots

From the geochemical data, 32 specific rock samples were selected from the 413 samples for geochemical plots, based on the highest gold values. The lower cut-off value for gold was chosen to be a 100 ppb to ensure a minimal precision for Au values; thus other rock samples with lower than 100 ppb Au value were not used for interpretation. In all geochemical plots, Au values were emphasized and compared to base metals and other Carlin pathfinder elements to determine trends, spatial associations, and paragenetic sequences.

Limitations

One of the main disadvantages of the geochemical plots in this study was the limited, available data points. As mentioned above, only 32 data points were used in the geochemical plots, since other data points that have lower than 100 ppb detection limit would not provide useful interpretation. Therefore, some trends in the geochemical plots may appear vague in data point density, and thus are portrayed as inferred lines.

Another limitation of the geochemical data arises from the geochemical presentation of data submitted by AGAT Laboratories. The lower detection limit of gold is 2.5 ppb in this geochemical package, but samples with exactly 2.5 ppb gold values are not differentiated from samples with <2.5 ppb in the data sheet. This poor presentation of data values eliminated 253 rock samples from the total of 453 that cannot be distinguished as having detectable Au. This is a fairly problematic issue and should be avoided in the future, because it affects and misleads data interpretation by qualifying samples below detection limit as samples with possible low gold values. In future geochemical analysis, the laboratory responsible for the assay should be advised to differentiate samples that are exactly at detection limit and samples that are below detection limit.

CHAPTER 3

CARLIN-STYLE GOLD MINERALIZATION IN THE VENUS ZONE, EINARSON PROPERTY, YUKON TERRITORY, CANADA

INTRODUCTION

The recent discovery of the Nadaleen Trend in the Yukon Territory by ATAC Resources Ltd. has led to a surge in exploration activity in the area for Carlin-style gold mineralization. Carlin pathfinder occurrences have been found over a 45 km distance suggesting the presence of a regionally significant fault system that conducted Carlin-like ore fluids (Bennett, 2012).

The Venus Zone is part of a larger claim block, called the Einarson Property, currently held by Anthill Resources Ltd. The Einarson Property is located 15 km to the southeast, along strike of the Conrad occurrence (ATAC Resources Ltd.), within a possible eastern extension of the Nadaleen Trend (Figure 3.1). Anomalous Au and other Carlin pathfinder elements (As, Tl, Hg, Sb, Se, Te, Ba) in soil and silt samples, along with a highest 191.8 g/t Au in grab sample, originally showed the potential of the area. In 2012, a successful diamond drill intersection of 9.67 g/t Au over 38.7 metres (Anthill Resources Ltd.) has led to further exploration activity on the Venus Zone during 2013.

REGIONAL GEOLOGY

The Einarson Property is located in the central eastern Yukon Territory, Canada, approximately 202 km of the town of Mayo. The Venus Zone is a 1.65 km^2 area, located at 64° 0' N, 131°57' W, 15 km east of the 50 km long Nadaleen Trend, on the northwest side of the Einarson Property (Figure 3.1). The Venus Zone is situated within the northern margin of the Selwyn Basin and on the western margin of ancestral North America. The Selwyn Basin is a part of the Cordilleran miogeocline, which is defined as a westward thickening sedimentary prism that accumulated on the westerly sloping Precambrian basement of Ancestral North America from late Proterozoic to mid-Jurassic (Gabrielse, 1991). The Selwyn Basin is a continental margin that formed from passive margin sedimentation and it is characterized by a thick accumulation of rift-related clastic rocks with deep-water offshelf sediments that persisted from late Precambrian to Middle Devonian (Gordey and Anderson, 1993). Spatially, the Selwyn Basin is bounded by the Dawson Thrust Fault to the north, the Mackenzie Platform to the east, and the Cassiar Platform to the southwest. The area on the northeastern side of the Selwyn Basin, which lies between Kathleen Lakes Fault and the Dawson Thrust Fault is informally known as the Rackla Belt (Figure 1.3-1.4). On the western side of the belt, the Dawson Thrust juxtaposes Neoproterozoic-Cambrian rocks of the Selwyn Basin (Gordey and Anderson, 1993) against Proterozoic-Paleozoic shelf and slope rocks of the Ogilvie Platform (Moynihan, 2014). The eastern side of the Rackla Belt is represented by the upper parts of the Neoproterozoic to Cambrian Hyland Group south of the Dawson Thrust,

whereas the upper part of the Neoproterozoic offshelf facies, fine clastic and carbonate rocks of the Windermere Supergroup is dominant to the north (Moynihan, 2014) (Figure 1.4). The Hyland Group, which is currently recognized as the main host of the Venus Zone mineralization is subdivided into three formations: 1. Neoproterozoic Yusezyu Formation compromising mainly coarse clastic rocks; 2. carbonate rocks of the Neoproterozoic Algae Formation; and 3. Neoproterozoic-Lower Cambrian Narchilla Formation, characterized by maroon to green shales (Gordey and Anderson, 1993; Cecile, 2000; Colpron, 2012). South of the Stewart River, the Cambrian to Silurian, fine-grained clastic rocks of the Gull Lake Formation and green, mafic volcanic breccia and conglomerate of the Old Cabin Formation is dominant in map 106B/04 Moynihan (2014).

The Venus Zone contains an isolated wedge-shaped panel (Moynihan, 2014) of Algae and Narchilla Formations in contact with mafic volcaniclastic rocks of the Old Cabin Formation to the north, and the clastic rocks of the Gull Lake Formation to southwest (Moynihan, 2014)(Figure AI.1). The wedge-shaped geometry of the Hyland Group sediments on the Venus Zone is suggested to form from out-of-sequence thrusting, where a low-angle thrust that separates the Algae and Old Cabin Formation is cut by another steeper fault, which itself is also intersected by an east-striking thrust (Moynihan, 2014). An alternative interpretation is that the Venus Zone itself is an isolated block (olistolith) that slid into its current position during the deposition of the Old Cabin Formation (Moynihan, 2014). There is evidence for both interpretations. The E-W striking thrust fault that separates the Algae

Formation from the Old Cabin Formation has been mapped by Anthill Resources Ltd. based on shallow plunging slickenlines, found underneath the dolostone cliff in 2013 during detailed mapping of the Venus Zone. However, boulders and blocks of limestone clasts up to 10 m in dimension have also been observed in area (Moynihan, 2014), which could mimic the formation of an olistolith on a smaller scale.

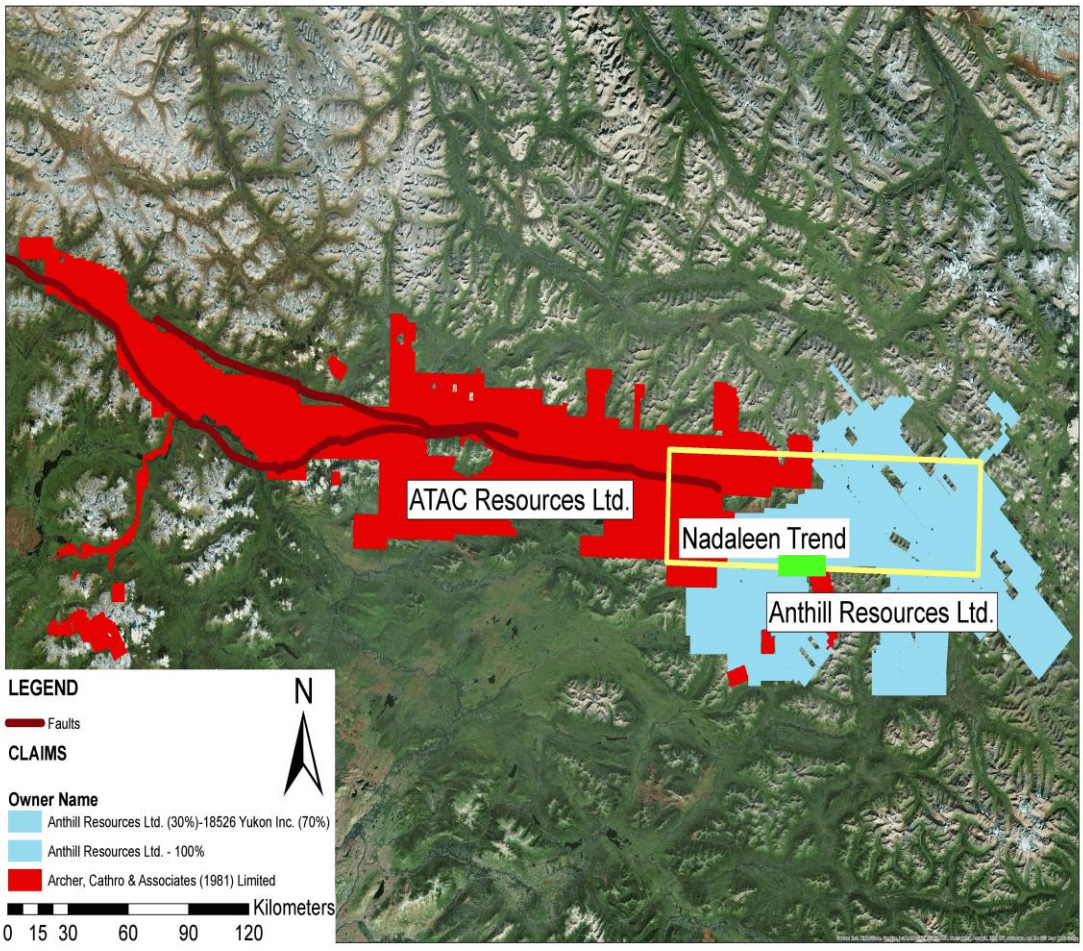

Figure 3.1. The Rackla Gold Belt outlining ATAC Resources Ltd. and Anthill Resources Ltd. claim blocks. The green rectangle indicates the Venus Zone. The yellow rectangle outlines the Nadaleen Trend.

PROPERTY GEOLOGY

The main lithology in the Venus Zone is characterized by carbonate-dominated sequences with locally intercalated siliciclastic rocks of the Algae Formation. This unit is in contact with green-coloured mafic volcanic breccia of the Old Cabin Formation to the north and southeast, and the basal member of the Narchilla Formation to the southeast (Figure 3.2). Gold mineralization in the Venus Zone is recognized in a carbonate sequence within the upper Algae Formation. The major lithological units in the Venus Zone are discussed in detail below with an emphasis on specific potential Au-bearing carbonate host lithologies within this sequence (Figure 3.3).

Non-carbonates and interbedded clastic rocks

This unit is exposed on the southeast side of Venus Zone and it is interpreted to be part of the basal member of Narchilla Formation (Moynihan, 2014) (Figure 3.2). The most characteristic rock type is thinly-bedded, well-cleaved, brown-weathered siltstone interbedded with maroon-weathered shales (Figure 3.4a). These rocks grade into thickly-bedded, variably calcareous, arkosic to quartz-rich sandstones interbedded with quartz grit, and locally strongly weathered conglomerate to the northwest (Figure 3.4b). The sandstone is light grey-weathered, medium-grained, black coloured; where calcareous it exhibits a distinctive grey-brown weathering. Thin, irregular beds of beige-weathered quartz arenite are locally present. The quartz grit is brownish-weathered, coarse-grained, non-calcareous and it locally

includes thin, scoured beds of conglomerate with 5-10 cm in diameter, sub-angular clasts that are often eroded-out from the matrix (Figure 3.4c). Abundant, orange, limonitic spots and detrital white mica in the matrix is common in the interbedded sandstones and quartz grits with sometimes more than 15 % of limonite-replaced grains. Despite the presence of local fault and silicified zones in this unit, gold mineralization has not yet been discovered.

Mafic volcanic rocks

There are two types of volcanic rocks present in the Venus Zone. The main unit is exposed on the north and southeast sides of Venus Zone, dominated by green volcanic breccia and conglomerate. This unit is brown-weathered with mafic clasts typically boulder in size in a fine-grained chlorite-rich matrix. The mafic clasts contain plagioclase and pyroxene phenocrysts and locally show amygdaloidal texture (Figure 3.5). In addition to mafic volcanic rock clasts, beige-weathered, sub-rounded limestone boulders are also common. Locally, space-filling calcite veinlets also occur in between boulders. The volcanic breccia is often interbedded with thinly-bedded, brown- to light brown-weathered, calcareous sandstone, siltstone, and local quartz pebble conglomerate. The other, less common volcanic unit is not well exposed on the property. This unit is an orange-brown to green-weathered, medium-grained, grey-green fresh coloured dacite with sometimes <10% fine-grained, disseminated pyrite in matrix. No gold mineralization has been yet observed in the volcanic rocks or at the contact between the volcanic rocks and the carbonates.

Carbonate rocks

Carbonate rocks are the dominant lithology in the Venus Zone. Dolostone is the most common rock type in a thickly-bedded, extensive cliff-face up to 300 m in width, on the northeast-northwest side of the Venus Zone (Figure 3.2). Silty limestone, calcareous sandstone interbedded with quartz grit and polymict debrite, and other clastic carbonates also occur-generally at higher elevation, above the prominent dolostone cliff. These carbonate rocks are all considered potential Au-bearing host lithologies and are discussed in detail below.

Silty oolitic limestone

Silty limestones are brown-weathered, medium-grained, with a black colour when fresh. These limestones are commonly planar bedded, and in some cases show an upward transition from graded beds to planar and cross-laminated beds. This is interpreted to represent deposition by sediment gravity flows, and it may show the A-B-C horizons of the Bouma sequence (Figure 3.6). Cross-beds indicate upward direction towards the SW. In thin section, these limestones have a fine-grained calcite matrix with medium-grained (5-20 μm) sub-rounded quartz, and anhedral calcite grains. Oolites are also present in matrix with recrystallized calcite cores (Figure 3.7a). The ore mineralogy is mainly framboidal pyrite (7%) with marcasite (1%) and minor arsenopyrite (<1%) (Figure 3.7b). Framboidal pyrites occur in clusters as small (2 μm) spherical grains. Subhedral-to anhedral, marcasite occurs as larger grains with quartz inclusions. Thin rims (1 μm) of pyrite often appear on the

edges of preexisting quartz grains and oolites. Fine-grained, euhedral arsenopyrite often nucleates on the edges of framboidal pyrite.

Sandstone interbedded with quartz grit and polymict debrite

This unit typically occurs at higher elevation above the dolostone cliff; however, the interbedded sequence has also been observed as separate beds within the dolostones on the northeast side of the property. The sequence consists of massive-bedded, brown-beige-to grey-weathered, medium-to fine-grained, non-calcareous to calcareous sandstone interbedded with brown-weathered quartz grit and polymict debrite (Figure 3.8a). Quartz grit commonly displays a gradation into sandstones. In the field, thin beds of quartz grit have a calcareous matrix, and locally contain sub-angular clasts of rusty weathered limestone, black shale, and green-weathered, mafic volcanic breccia (Figure 3.8b). Quartz grits locally exhibit a vuggy, brownish weathering in between the quartz grains. Polymict debrites usually occur at the base of the interbedded sequence. Angular-to sub-angular clasts consist of fine-grained quartz and grey-coloured limestone (Figure 3.8c). The size of the clasts varies from cm scale to boulder scale. On the northeast side of the property, orpiment clasts 1-10 cm in diameter are present in a thin bed of debrite (Figure 3.8d-e). This is interpreted as an original debrite bed with limestone clasts that have been replaced by orpiment. The interbedded sequence also occurs on the northeast side of the property, below the dolostone cliffs, where it's exposed along a NE trending fault zone. Here the sequence includes white to brownish weathered, thin-bedded siltstones that variably occur between calcareous sandstone, quartz grit, and

dolostone. In thin section, sandstones and quartz grits have a calcite-rich matrix with medium-to fine-grained (250-500 μm) sub-rounded quartz (Figure 3.8f-g). Mineralization includes predominantly syn-sedimentary, framboidal pyrite (1%) and anhedral pyrite (3%) that usually occur in clusters in between sedimentary grains. Arsenic sulphides are present in form of arsenian pyrite (<1%) and fine-grained arsenopyrite (<1%), mainly in the calcareous sandstones (Figure 3.8h). Quartz grit also contains framboidal pyrite, however, arsenic sulphides occur at a larger percentage (5%) in comparison to sandstones.

Dolostone-sandy dolostone

Dolostones are the most common rock-types at Venus Zone, where they form a distinctive, massive bedded, 300-400 m thick extensive cliff face (Figure 3.2). Dolostones are medium–to coarse-grained, often stylolitic, and are coloured light-brown, beige, and pink. Boxwork silicification and quartz-carbonate veinlets commonly occur on the weathered surface parallel and/or perpendicular to bedding. Dolostones display a wide textural variety in the field and in thin section. Some dolostone are medium-grey coloured, fine-grained, massive textured with large (1-2 cm) quartz-carbonate veins cross-cutting the matrix, while others are coarse-grained and exhibit a more pebble-like, spotty texture (Figure 3.9a-b). Sandy and non-zebra-textured dolostones seem to occur at shallow depth in drill holes to date, while zebra-textured and pebbly dolostones are at greater depth. In thin section, most dolostones have a calcite-carbonate-rich matrix; however, the quartz-calcite ratio varies greatly, depending on the nature of the rock. The quartz-calcite

ratio and the percentage of quartz grains in matrix give a great distinguishing feature between the different varieties of dolostones that is not apparent in the field. Some of the observed dolostones are sandier, which in thin section is manifested by the higher percentage (~45%) of rounded-to sub-rounded quartz grains, whereas some of the 'true' dolostones on the property contain only a very low percentage of quartz in matrix (Figure 3.9c). Very fine-grained (2-3 μm), framboidal and anhedral pyrite is also present, mainly in stylolites, and less commonly in matrix. Sandy dolostones generally have a low percentage (<1%) of realgar or orpiment. Anhedral, fractured pyrite (10 μm) is commonly present on the edges of quartz grains. Pebbly dolostones are generally more mineralized with realgar and orpiment up to 15%. Fine-grained arsenopyrite usually occurs with realgar, sometimes up to 4%.

Zebra-textured dolostone

Zebra-textured dolostones occur irregularly within the dolostone beds. In outcrop, zebra-texture is not always apparent and the rocks exhibit a similar brown-to tan-weathered surface with local pink hue as non-zebra textured dolostones. Dolostones with zebra bands tend to be more calcareous and calcite veined than other dolostones. The matrix is often vuggy, and zebra bands seem to develop parallel to bedding (3.10a). These dolostones consist almost entirely (85%) of calcite-carbonate in thin section. There is no compositional variation between the matrix and the coarser-grained zebra bands. While the matrix is fine-grained (5 μm), zebra-bands form bladed, coarse grains (500-700 μm) (Figure 3.10b). Pyrite forms anhedral, strongly fractured, medium (200 μm) grains. The dominant ore

mineralogy in zebra-textured dolostones is realgar and orpiment (5%), which most often occur in thin spider veinlets brecciating the matrix or completely replacing zebra bands (Figure 3.10 c-d). In fact, zebra-textured dolostones exhibit the most intense realgar and orpiment mineralization. Arsenopyrite (<1%) is also present as fine-grained (1 μm) inclusions within realgar and orpiment veinlets.

Silicified dolostone

Silicified dolostones occur irregularly within the dolostone beds. The degree of silicification varies. Completely silicified dolostones are typically white coloured with sugary texture, and have the appearance of pure quartz (Figure 3.11a). In drill core, the same lithology displays a black colour, massive texture, and has a hardness of ~7 throughout. Less silicified dolostones do not show any weathering or texturally distinguishable feature. In these dolostones, silicification can only be tested by the hardness, and non-reactivity to acid. This can be misleading because the reactivity of dolostones to acid and their hardness greatly varies due to the great variety of texturally and compositionally different dolostones present in the Venus Zone. In thin section, silicification is readily visible as the complete or partial replacement of carbonate matrix by quartz (Figure 3.11b). In general, most silicified dolostones are scorodite altered. In the field, scorodite alteration can be identified by its yellow-to green hue on fresh and weathered surface. In some cases, scorodite also occurs as thin (1-2 mm) veinlets that have a typical pale green colour. Framboidal pyrite and fine-grained marcasite commonly occur up to 5 %. The ore mineralogy of silicified dolostones includes fine-grained arsenopyrite (5-10%) and

arsenian pyrite (1-2 %). Realgar and orpiment are locally present (≤1%). Silicified dolostones have the highest percentage of arsenopyrite and arsenian pyrite.

Brecciated dolostone

Brecciated dolostones commonly occur along high-angle, NE trending faults and fracture zones. There are a great variety of different breccia types that have been observed. Fault breccias commonly occur as strongly weathered, incohesive fragments in float with a green-yellow hue, and locally rusty, hematitic-rich soil. Less common, dissolution breccias have a green- to yellow-coloured, and sometimes vuggy, carbonate-flooded matrix. Clasts are angular to sub-angular, 1 to 50 cm in diameter, with a recrystallized dolomite and/or carbonate matrix (Figure 3.12a-b). The intensity and scale of brecciation varies; brecciated zones range from cm to outcrop scale. In drill core, fault breccias consist of sub-angular fragments (1-10 cm) in a finer-grained matrix or as incohesive, clay rich, fine- to ultrafine-grained cataclasite with local lithic fragments. Dissolution textures in drill core lack any preferred orientation, and often occur as clast-supported breccias with sub-angular fragments, or as breccias with vuggy, decalcified matrix (Figure 3.12c). Dissolution seams are often present in the vicinity of breccias. Dissolution seams are black, thin (0.5-1 cm), fine-grained veinlets that resemble stylolites, except they have an irregular anastomosing form (Figure 3.12d). Locally, crackle dolostone breccias have been observed in drill core with sub-rounded, 1-5 cm large clasts with little or no displacement. In thin section, dissolution textures are evident by the brecciation of carbonate matrix, where anhedral, coarse-grained (500 μm) calcite and dolomite

grains occur in fine-grained carbonate matrix (Figure 3.12e). The mineralization of brecciated dolostone varies. Dissolution breccias with vuggy, calcite-flooded matrix, and with no dissolution seams present, do not show any significant mineralization. However, breccias with subangular fragments (1-2 cm) and carbonate matrix contain framboidal to subhedral pyrite (4%), euhedral arsenopyrite (3%), and local realgar (2-3%). Dissolution seams range from a 125-200 μm in width and often contain pyrite, realgar, and locally, gold grains (Figure 3.12f).

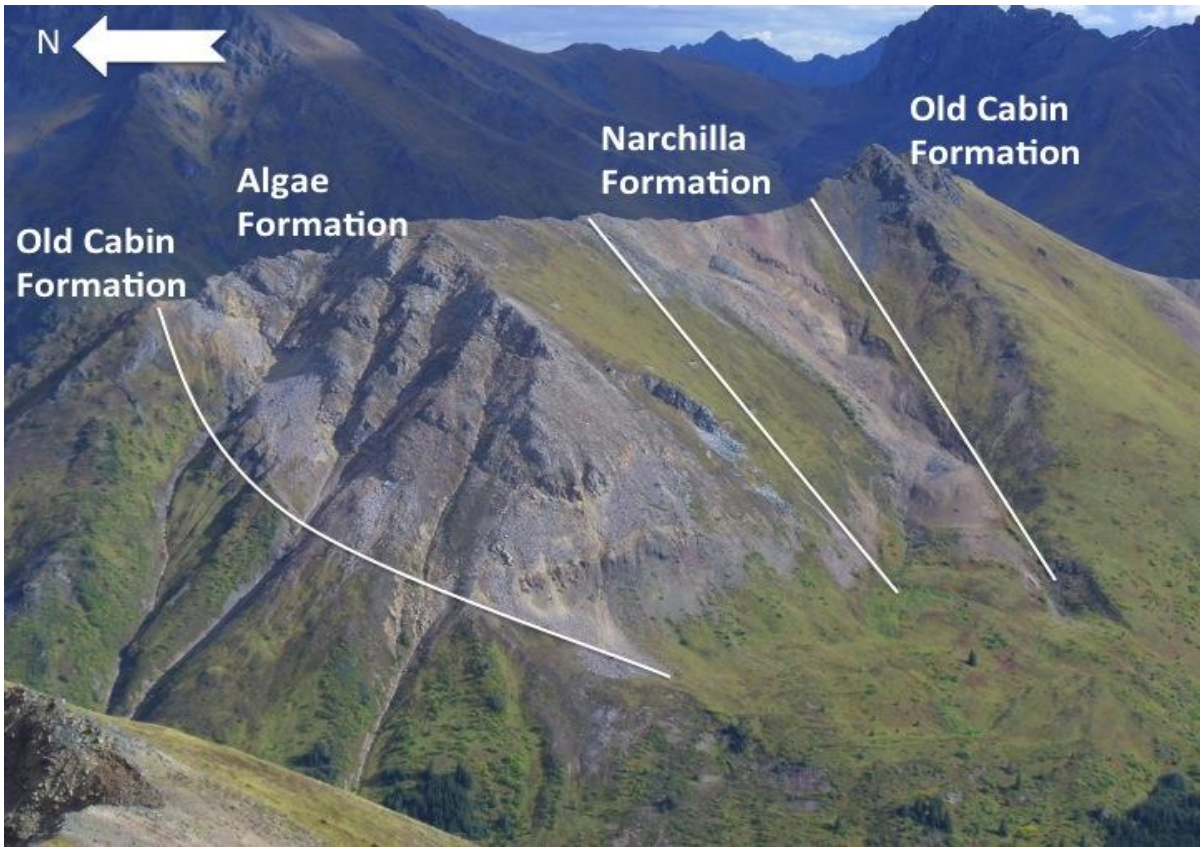

Figure 3.2. Photograph of the Venus Zone showing lithological distributions. Prominent cliff-face in centre-left is primarily composed of dolostone.

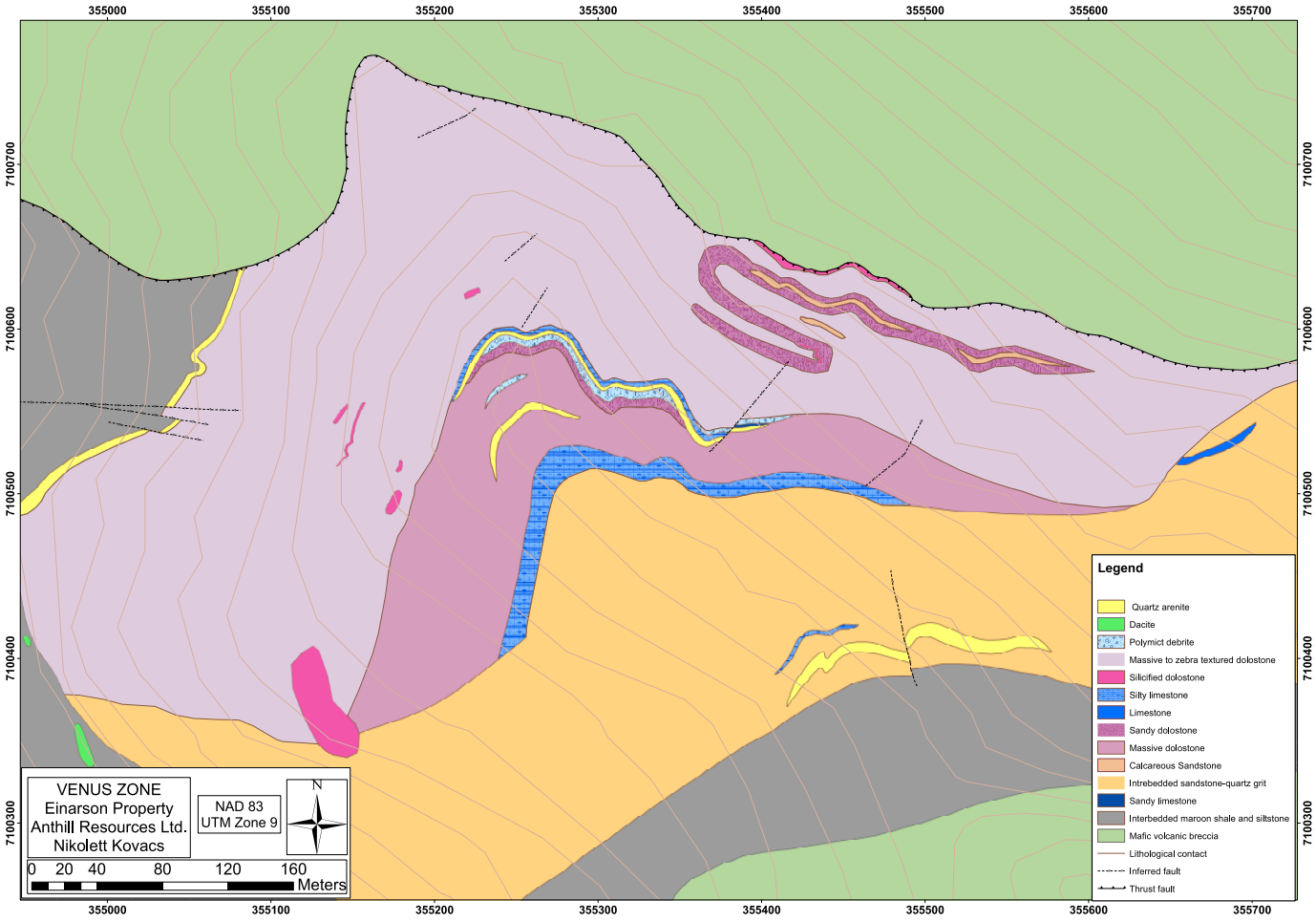

Figure 3.3. Bedrock geology map of the Venus Zone, Einarson Property, Yukon, Canada.

Figure 3.4. Non-carbonates and interbedded clastic rocks. A., Siltstone interbedded with maroon weathered shales. B., Quartz grit with limonitic grains. C., Conglomerate with weathered-out, subangular clasts.

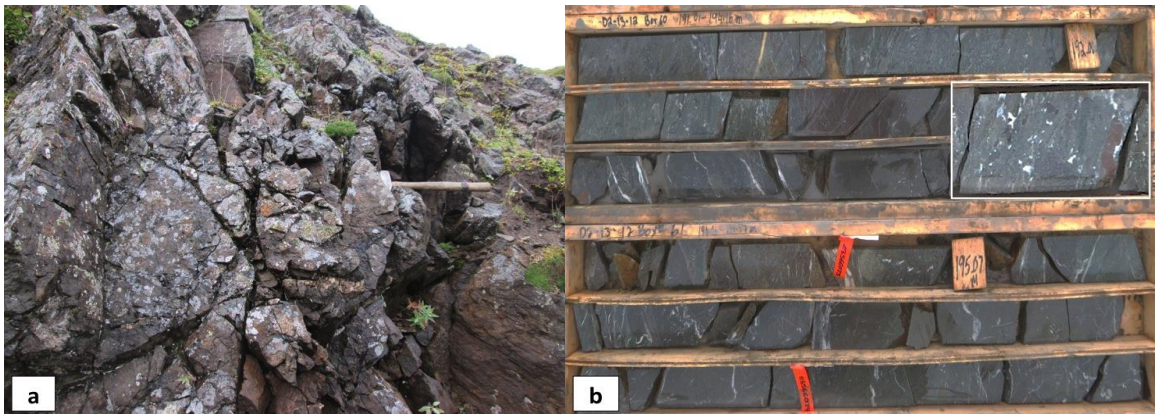

Figure 3.5 A., Mafic volcanic breccia in outcrop. B., Mafic volcanic breccia with chlorite-rich matrix in drill core.

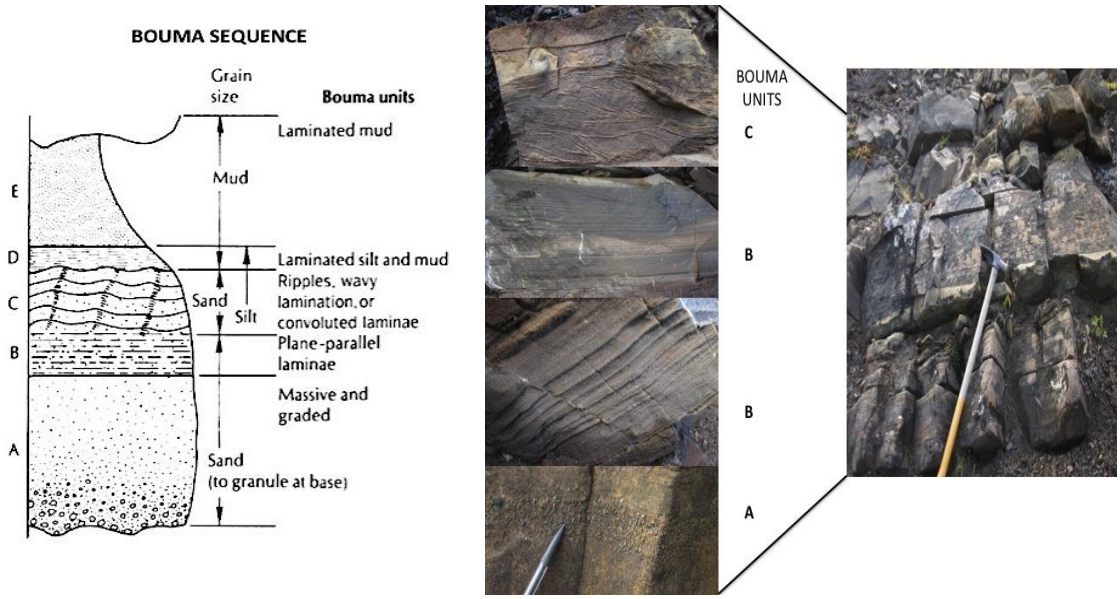

Figure 3.6. Bouma sequence in silty-oolitic limestone *(Modified after Bouma, 1962).*

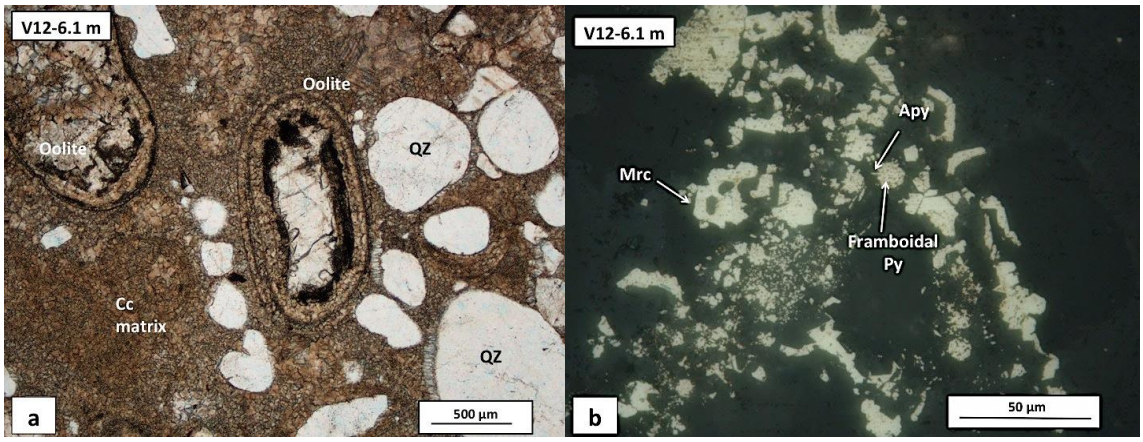

Figure 3.7. A., Silty-oolitic limestone in thin section under plane polarized light. B., Ore mineralogy of silty-oolitic limestones in thin section under reflected light.

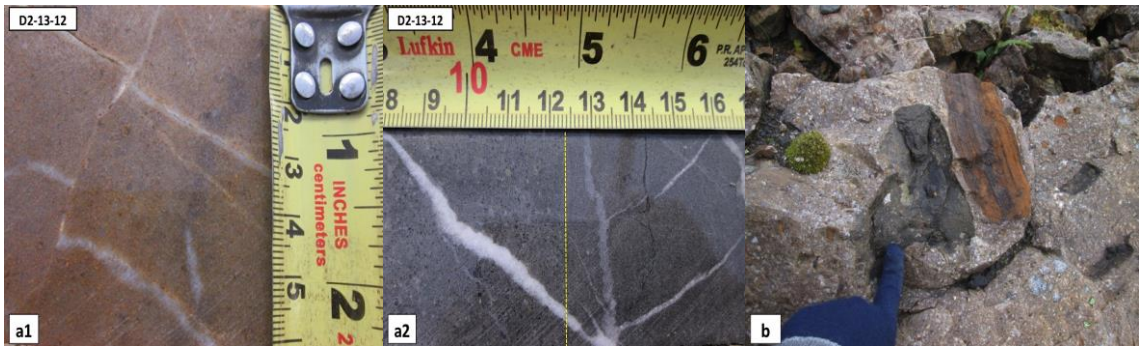

Figure 3.8. A_1 and A_2. Calcareous sandstone in drill core. B., Quartz grit with limestone and mafic volcanic inclusions.

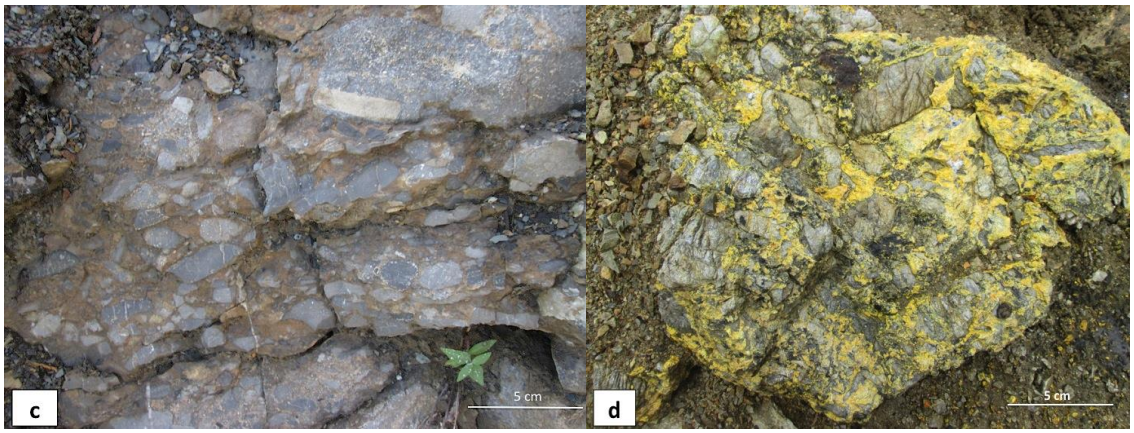

Figure 3.8. C., Polymict debrite with limestone clasts. D, Polymict debrite with orpiment replaced matrix.

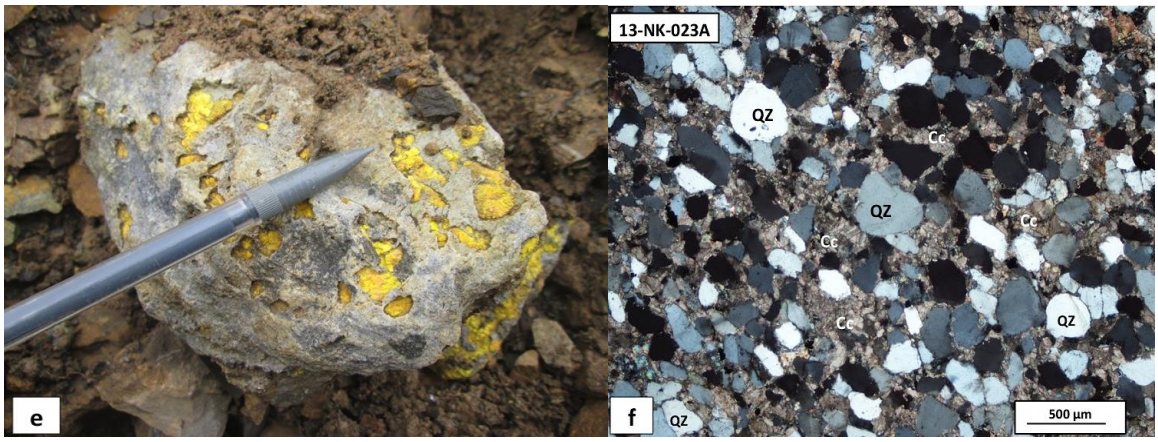

Figure 3.8. E., Polymict debrite with orpiment clasts. D., Calcareous sandstone in thin section.

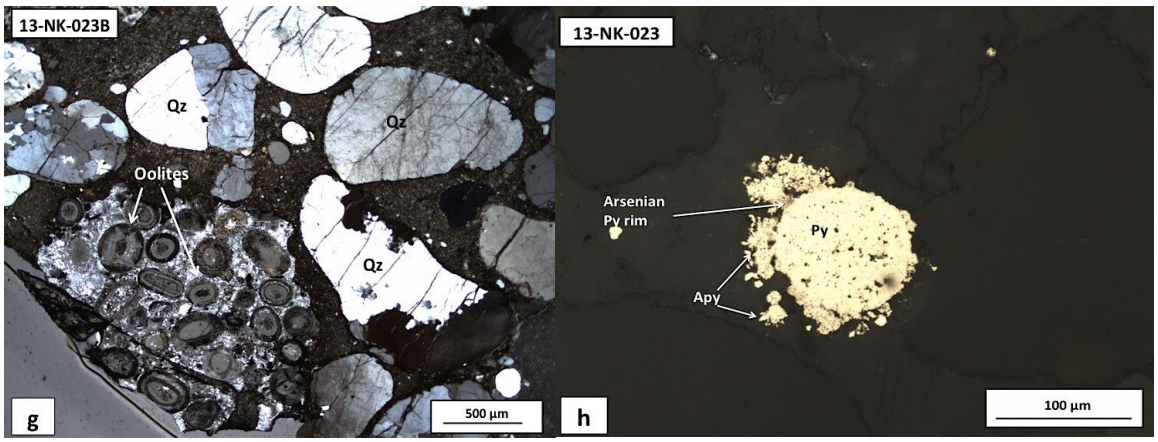

Figure 3.8 G., Quartz grit in thin section. H., Framboidal pyrite with arsenopyrite and arsenian pyrite overgrowth in calcareous sandstone, reflected light.

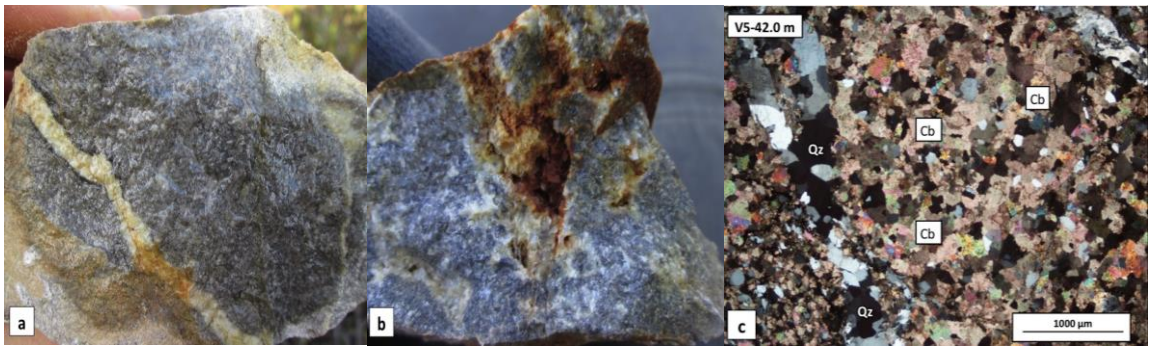

Figure 3.9. A., Massive textured dolostone. B., Pebbly textured dolostone. C., Sandy dolostone in thin section.

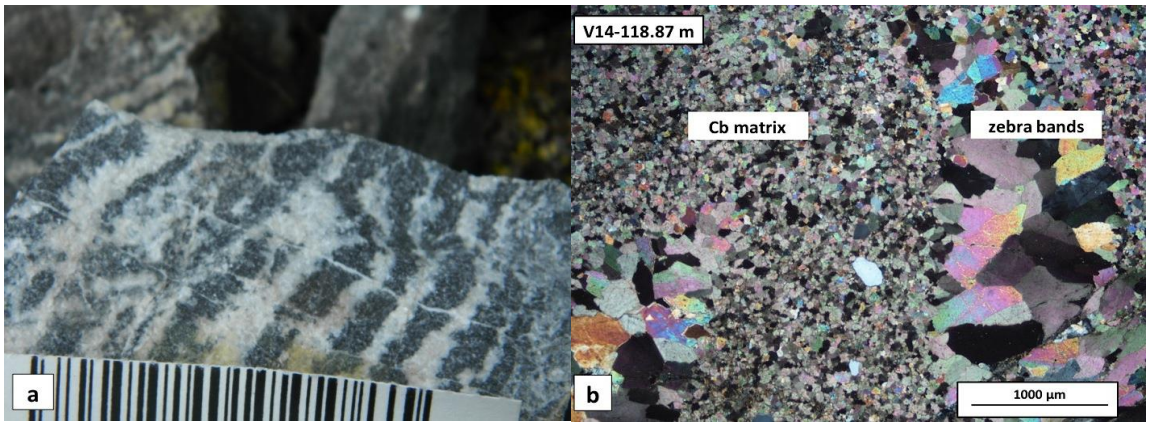

Figure 3.10. Zebra-textured dolostones. A., Zebra texture in hand sample. B., Zebra-textured dolostone in thin section showing the grain size variation between matrix and zebra bands.

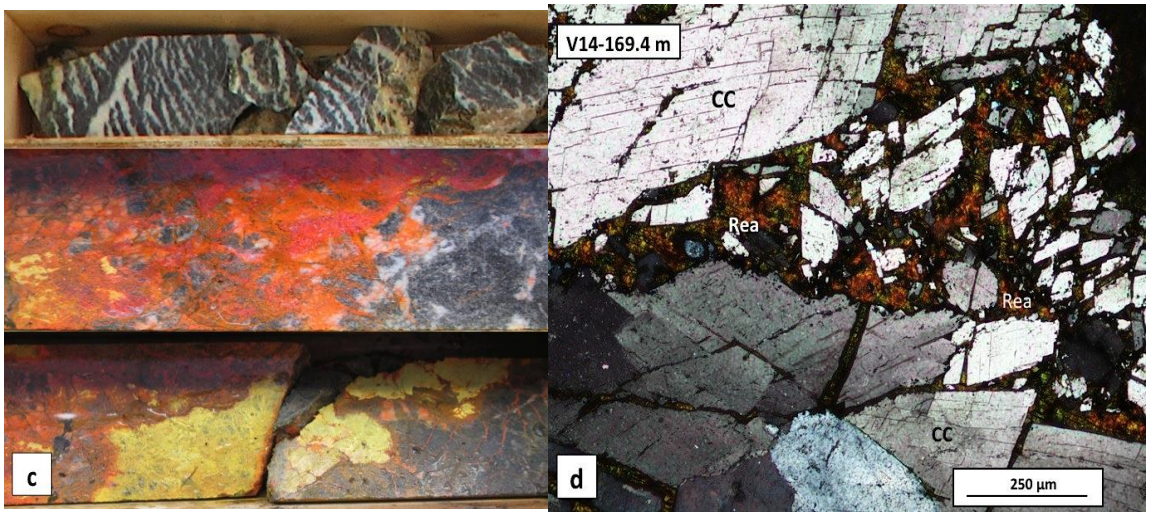

Figure 3.10. C., Realgar and orpiment mineralized dolostone showing the progression from unmineralized zebra-textured dolostone to complete replacement of matrix by realgar and orpiment. D., Realgar veinlet brecciating the matrix of zebra-textured dolostone in thin section.

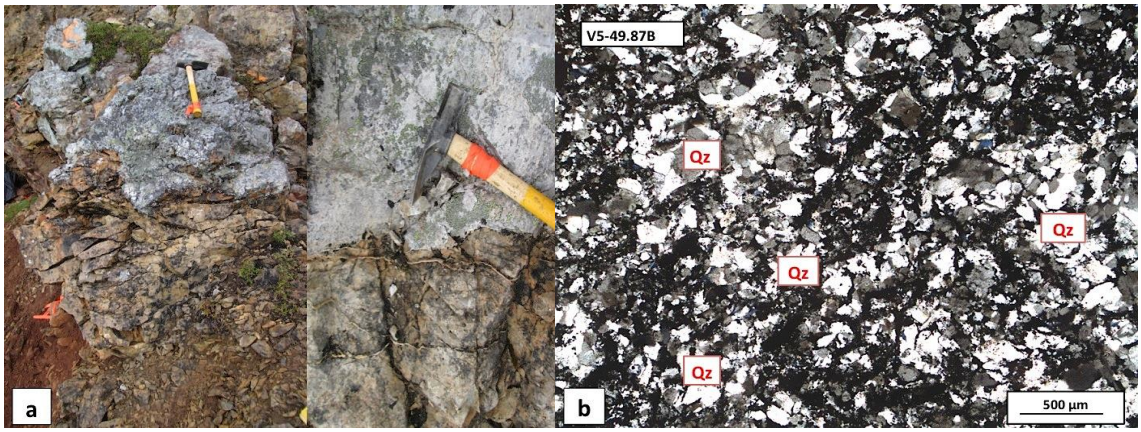

Figure 3.11. A., Silicified dolostone in outcrop. B., Silicified dolostone in thin section showing the complete replacement of carbonate matrix by quartz.

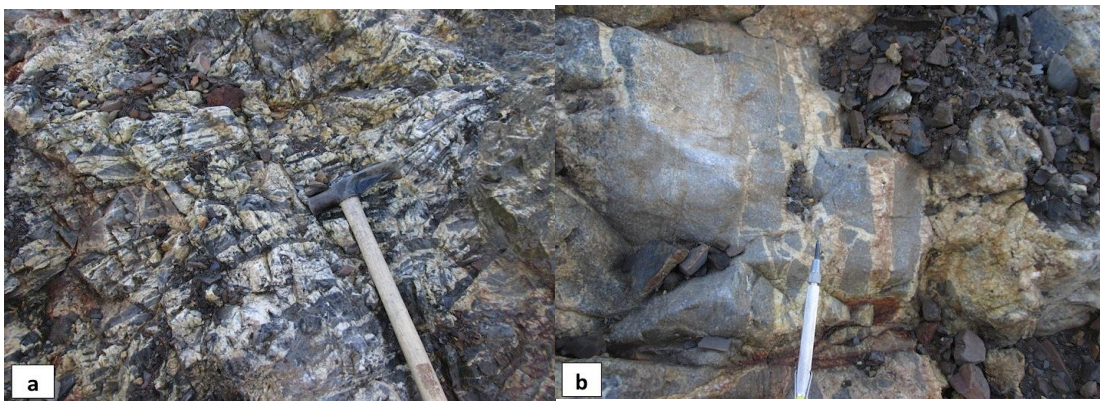

Figure 3.12. A-B., Dissolution breccia in outcrop with carbonate-flooded matrix.

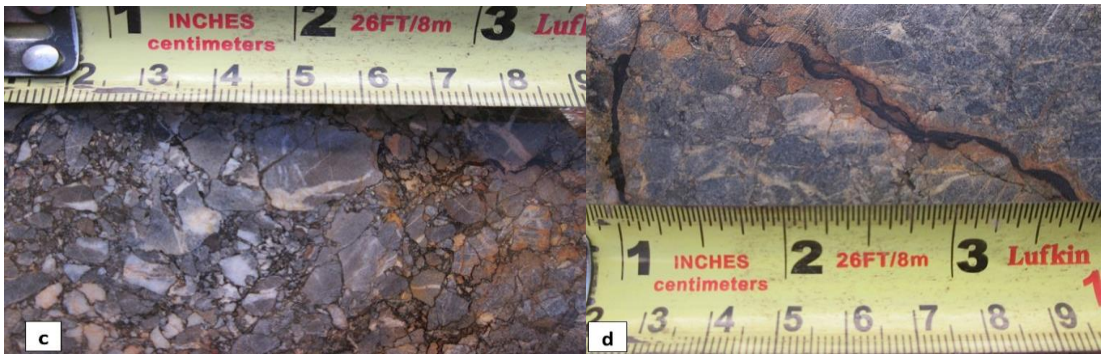

3.12 C., Dissolution breccia in drill-core. D., Dissolution seam in drill-core.

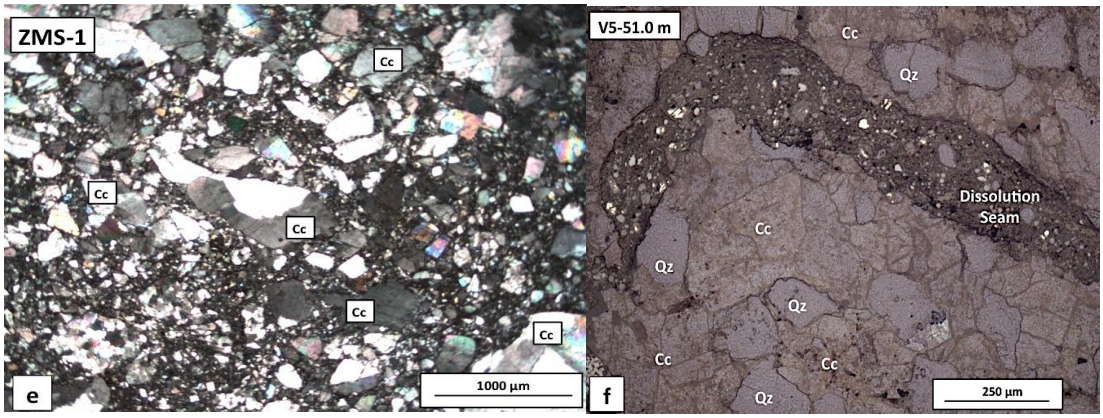

3.12 E., Dissolution breccia in thin section. F., Dissolution seam in thin section.

STRUCTURAL GEOLOGY

Regional setting

The eastern part of the Nadaleen Trend, including the Venus Zone, is part of the Selwyn Fold Belt, which developed during the Jura-Cretaceous shortening associated with the Cordilleran orogeny (Gordey and Anderson, 1993; Moynihan, 2014). There are no plutonic rocks exposed in the NTS 106B/04 map sheet area (Moynihan, 2014) (Figure AI.1). The closest nearby, small granitic stock is the 62.9±0.5 Ma (2σ) (Theissen et. al., 2011) Rackla Pluton, which is approximately 100 km east from the Venus Zone. One of the major fault systems nearby the Venus Zone is an east striking, north verging thrust fault that separates the Gull Lake Formation from the underlying Old Cabin Formation with a southerly dipping fault plane (Moynihan, 2014) (Figure AI.1), south of the Venus Zone. Dominant structures around the Venus Zone are oriented NW-SE including folds and steeply dipping axial-planar cleavage (Moynihan, 2014). The Venus Zone is a structurally complex area that does not resemble its surroundings lithologically or structurally. Bedding is inconsistent throughout the Venus Zone as result of polyphase deformation. There are three different bedding directions that have been observed: 1. NE to SE striking, moderately dipping beds to the south, 2. SW striking, moderately dipping beds to the north, and 3. NW striking, steeply dipping beds to the northeast. The most dominant bedding direction is NE to SE striking and moderately south dipping (Figure AI.2).

Polyphase deformation

There are at least 3 phases of folding in the Venus Zone. The oldest phase (F1) is interpreted to be an overturned, recumbent to reclined, isoclinal to tight fold (Figure 3.14a). F1 is difficult to see in large-scale outcrops, because of the overprinting relationship of the other two, later generations of folds. Recumbent folds have easterly striking, horizontal- to subhorizontal axial planes (AP_1) with shallow plunging, south trending fold axes (F_1). Reclined folds show a moderately south dipping (30-35°), easterly striking axial planes (AP_1) and shallow plunging, south trending fold axis (F_1). The second phase of folding (F2) is especially evident in the NE side of the property, where an antiform-synform pair with at least a 100 m of amplitude and 50 m or more of wavelength has been observed (Figure 3.13). F2 is characterized by upright, closed to tight folds with N-NW/S-SE trending, moderately dipping axial planes (AP_2). AP_1 is refolded by F2 folds (Figure 3.13). The superimposition of phase 1 and 2 folding is also evident in outcrop scale (Figure 3.14b-c). The youngest phase in the folding history is an upright, large-scale fold; however, measured fold-axes and axial planes show a great variability, because they are dependent on the earlier two phases and the massive, blocky nature of dolostone cliffs do not show deformational fabric well. The folded appearance of the Venus property itself could be indicative of the youngest deformational, post-thrusting phase.

E-W striking thrust fault

An E-W striking thrust fault has been identified and mapped by Anthill Resources Ltd. on the north side of the property based on low-angle slickenlines found underneath the dolostone cliff, which is interpreted to be the thrust plane (Figure AI.2). This thrust fault separates the dolostones of Algae Formation from the mafic volcanic breccia of the Old Cabin Formation. The same fault was also identified by Moynihan (2014) during his regional mapping of the area and described as a fault with unknown movement (Figure AI.1). The folded appearance of the fault suggests that thrusting was active before or during the youngest folding phase.

NE striking brittle faults

Geological mapping of the Venus Zone delineated 2 major NE striking brittle faults on the northeast side and three minor NE striking faults on the northwest side of the property (Figure 3.15a). Other small-scale (<100 m), E-W striking faults have also been observed in the southwest corner of the property offsetting a continuous bed of quartz arenite (Anthill Resources Ltd.) (Figure AI.2). The true orientation of the faults is difficult to define and slickenline directions show a great variability. Furthermore, no true fault plane orientation has been identified in the field, which would help to determine the true, three-dimensional orientation of the faults. The most easterly lying fault on the northeast side shows a 10 m sinistral offset in plan view (Figure AI.2). Slickenlines along the fault zone indicate southwest trending, shallow plunging movement. In general, NE striking faults are characterized by hematitic-rich soil, fault gouge to fault breccia development, and show elevated gold,

arsenic, and mercury values (Figure AI.3-5). Silicified zones often extend for several meters along these fault traces (Figure 3.15b). In drill core, faults can be traced by zones of poor recovery, which generally succeeds and/or precedes well-developed breccia zones. Clay mineralized fault gouge intervals are especially common in drill hole D2-13-14. Small-scale (3-5 cm) normal and reverse faulting is locally preserved in drill core, mainly evident by the offset of quartz-carbonate veinlets (Figure 3.15c-d). Based on the deformation characteristics, lithology, and geochemistry observed, NE striking, brittle faults appear to be a significant fluid conduit for mineralizing fluids, especially where they intersect receptive and reactive host lithologies.

High-angle brittle fractures

High-angle fractures are common structural features in the Venus Zone. The orientation of these fractures are not consistent throughout the property; however, there are two main domains that can be distinguished: 1. NW-SE striking, steeply dipping, and 2. SW striking, steeply dipping fractures. Fracture planes are commonly mineralized and often bound zones of silicification (Figure 3.15b). This is visually apparent in the field and it can help to locate mineralization.

Shear zones

Well-developed shear zones have not been yet observed in the field; however, drill hole D2-13-12 intersected a 1 m wide shear zone at 186.90 metres, close to the contact between the dolostone and mafic volcanic breccia. Rocks in drill core display elongated, sheared clasts of dolostones (3-4 cm in width) in a medium-grained,

strongly clay altered, oxidized, rusty weathered matrix. Geochemical values obtained from rock-chip samples indicated elevated arsenic and mercury values close to the contact (Figure AI.4-5). A thin section taken from the drill core showed elongated clay bands and clay altered matrix. Mineralization compromises coarse-grained (40 μm) marcasite (10%) and fine-grained (5 μm) pyrite (3%) (Figure 3.21). Mineralization has not been extensively tested at the contact zone between the mafic volcanic breccias and dolostones due to the lack of visible shear zones. However, these shear zone boundaries should be considered prospective, particularly when they occur between two lithological units, because they can result in unique zones of strain expressions that can localize fluids.

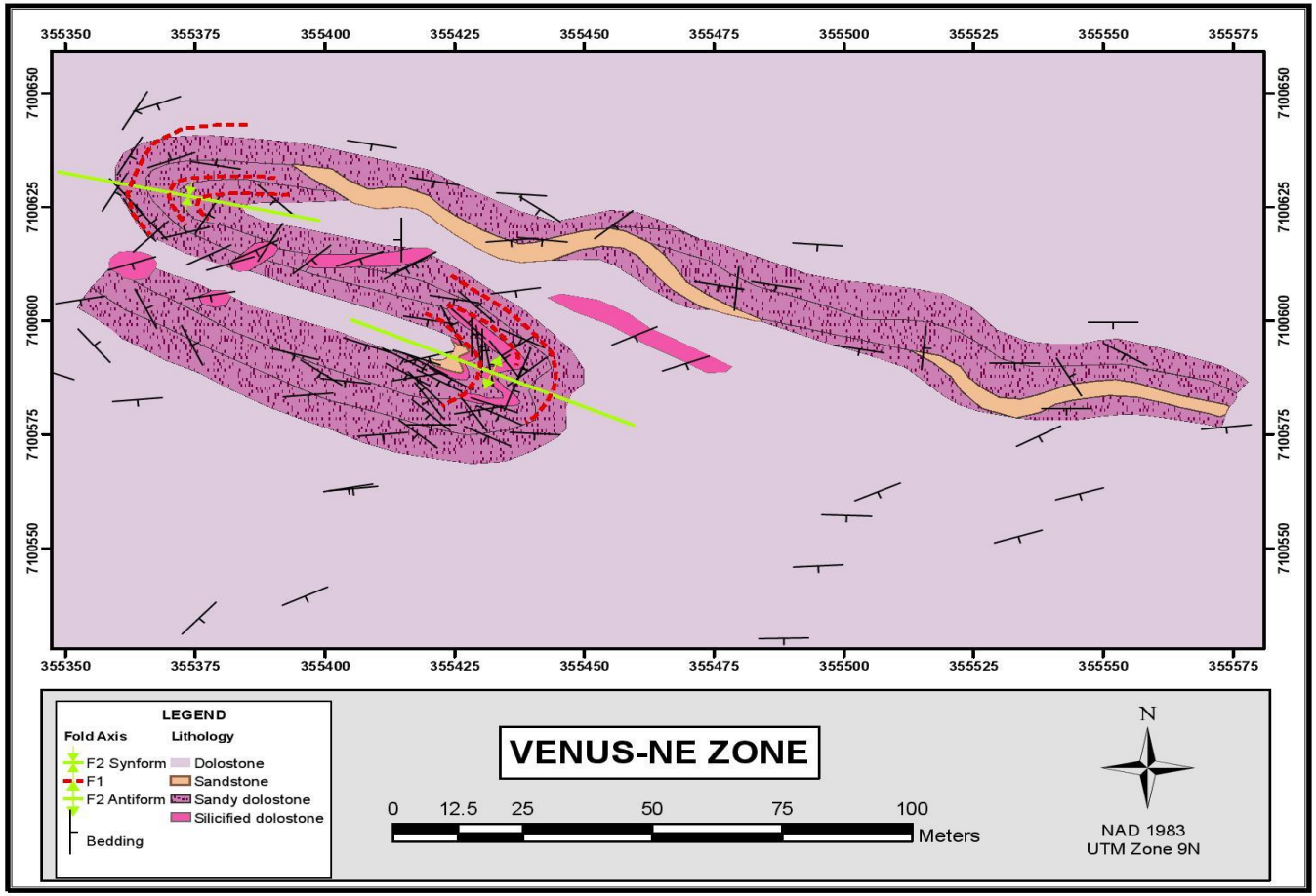

Figure 3.13. Map of the NE Venus Zone, showing a second-generation (F2) antiform-synform pair.

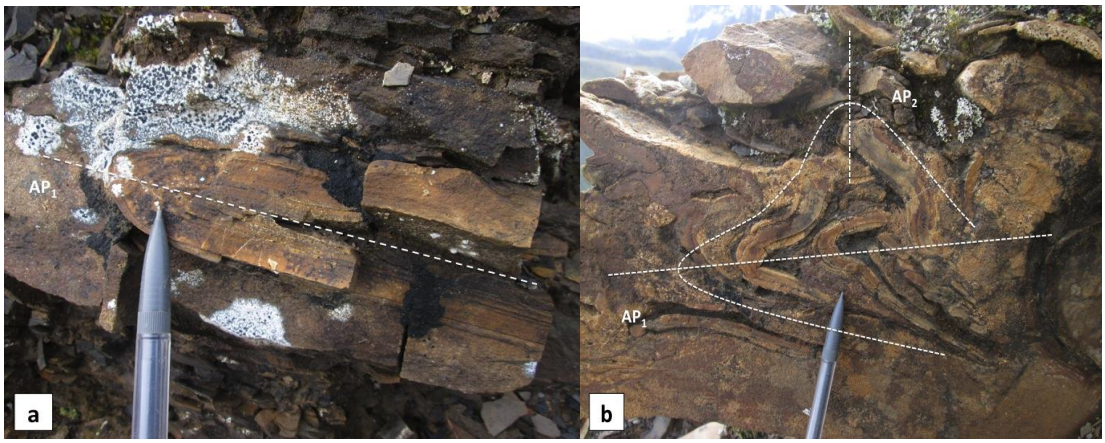

Figure 3.14. A., F1, recumbent, tight fold. B., Superimposition of phase 1 and 2 folding.

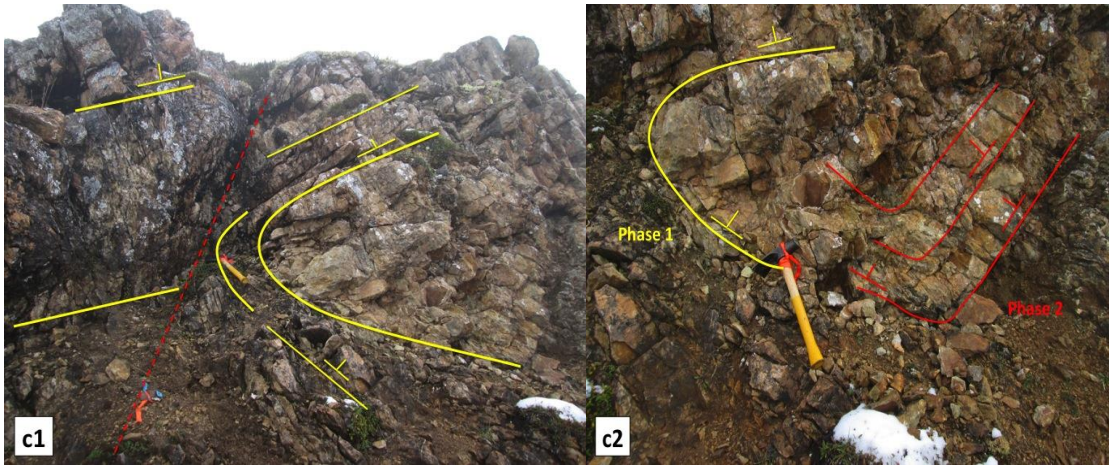

Figure 3.14. C_1., Phase 1 overturned fold truncated by a NE trending fault. C_2., Close up of image C_1 showing the superimposition of phase 1 and 2 folding.

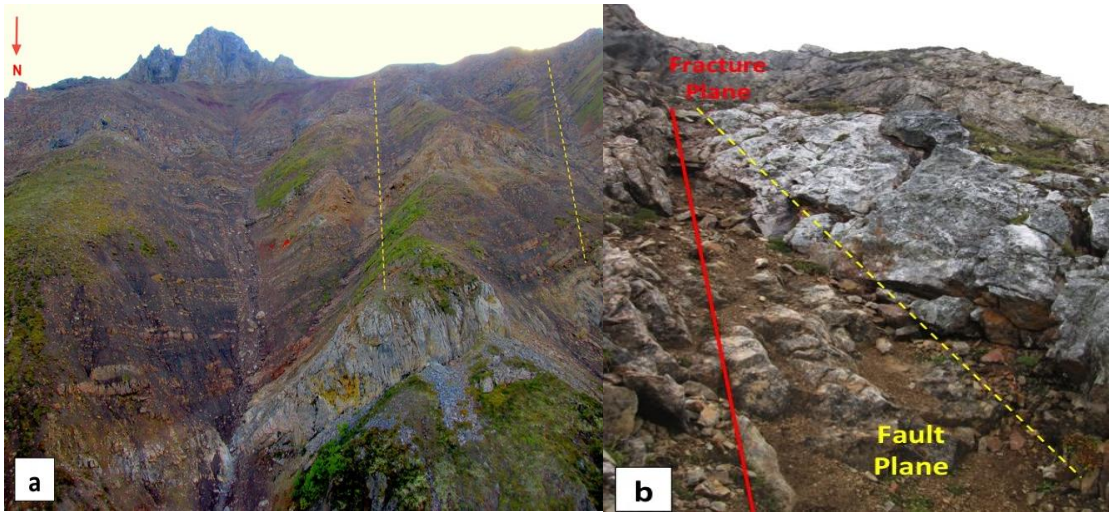

Figure 3.15. A., NE trending brittle faults, NE Venus Zone. B., Fault and fracture planes bound silicified zone, central Venus.

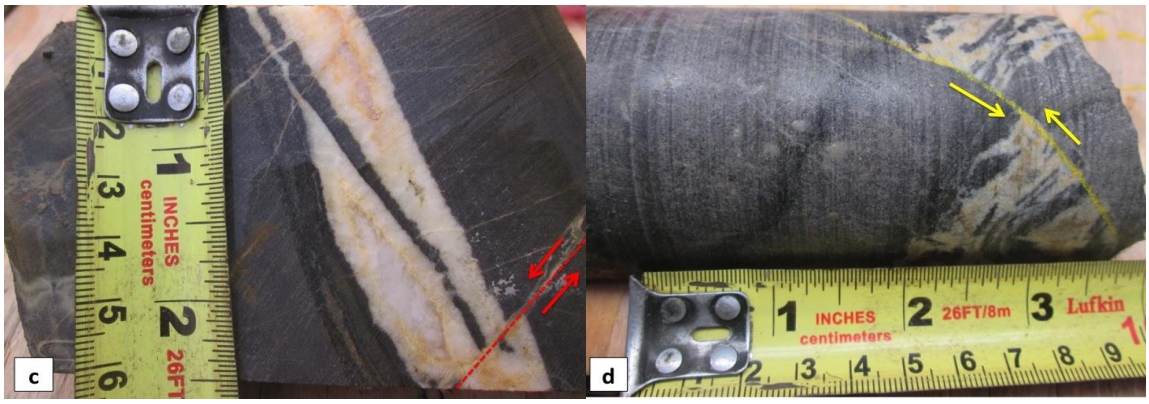

Figure 3.15. C., Normal faulting in drill core (D2-13-14), NE Zone. D., Reverse faulting in drill core (D2-13-14), NE Zone.

ALTERATION

There are two main alteration-types that have been observed on the Venus Zone: 1. silicification and 2. decarbonatization. Silicification is the most prominent and it is the best indicative alteration-type of gold-mineralized lithologies. Silicification is structural controlled and silicified zones often occur along high-angle brittle fault zones or fractures (Figure 3.15b). These zones extend from 15 to 100 metres, whereas sometimes, only parts of the outcrop are silicified (Figure 3.15a). Silicified zones in the field have a distinguishing white colour and often associated with pale yellow-green coloured scorodite mineralization. In the NE Venus Zone, silicified zones variably occur on the northeast limb and in the hinge of F_2 folds. One particularly strongly silicified outcrop in the F_2 hinge zone of the antiform shows a folded pattern, which suggests that silicification predates the second phase of folding (Figure 3.13). In other areas of the Venus Zone, silicified zones are immediately peripheral to gold mineralization (Figure AI.3). Gold mineralization has been located within 10-15 metres of identified silicified zones. In addition, the

highest gold values to date have been recognized in samples with completely silicified matrix and scorodite mineralization. SEM–EDX microscope analysis of Au-bearing samples show arsenopyrite and scorodite rimmed quartz grains. This observed paragenetic relationship between quartz–arsenopyrite-scorodite further suggests that silicification predates the second phase of folding and that silicification is pre-ore stage.

Decarbonatization is the second most prominent alteration-type; however, the true nature of decarbonatization is only apparent in thin section. Dissolution breccias locally occur in the field in outcrop-scale as a result of decarbonatization (Figure 3.12). Their characteristic appearance and textures are described under *Property Geology, Brecciated dolostones,* above. Furthermore, no significant gold mineralization yet has been discovered in dissolution breccias, thus decarbonatization may not be a useful alteration-type to directly locate gold mineralization.

Lastly, sericite alteration has been found in one thin section (V5-49.87) in a silicified, high-grade dolostone. Some sections in drill core also show white mica alteration locally. Sericite alteration in high-grade, silicified dolostone suggests that there is a spatial relationship between sericite and gold mineralization, however, the true characteristics and paragenetic sequence of sericite is beyond the scope of this paper and requires more sericite altered samples for further analysis.

MINERAL PARAGENESIS AND GOLD MINERALIZATION

Thin sections obtained from drill core and rock samples were examined petrographically to define ore paragenesis (Figure 3.36). SEM-EDX microscopy was used to elucidate gold deportment and to characterize sulphide compositions and textures. The morphology, size, and textures of gold-bearing ore and other associated sulphide and gangue minerals from the Venus Zone are discussed in detail below.

SYN-SEDIMENTARY AND EARLY DIAGENETIC STAGE

Calcite-Dolomite

Most carbonate lithologies are calcite dominated, with a modal abundance of > 70 % calcite. Calcite is subhedral-to anhedral, often medium-to coarse-grained (250-500 μm) (Figure 3.16a_1). Silty limestones and dolostones have less calcite (50-60 %) and a variable amount of quartz grains (5-15%). SEM-EDX analysis indicated that there are two compositionally different calcites. One generation of calcite grains is close to end-member, whereas the other generation is manganese-rich in composition. There is no textural or morphological difference between these two calcite generations. Dolomitization of calcite grains is common. Dolomite grains are more subhedral, coarser-grained (500-1000 μm) and often exhibit higher birefringence than calcite, with no apparent lamellar twinning (Figure 3.16a_2). This is especially apparent in zebra-textured dolostones, which show two texturally different dolomite types. Fine-grained (5-10 μm), subhedral-to anhedral dolomite grains

make up the matrix, whereas coarse-grained (500-700 μm), anhedral, locally bladed grains form the zebra-bands (Figure 3.10b).

Apatite

SEM-EDX analysis revealed the occurrence of apatite in close association with some occurrences of framboidal pyrite. Apatite grains are anhedral to sub-rounded and 5-7 μm in diameter. They often occur in clusters and rimmed by fine-grained (1-2 μm) pyrite (Figure 3.16b). Based on the lithologies observed on the Venus Zone and their inferred paleoenvironment, apatite is interpreted to have formed during early diagenesis from microorganisms as a biomineral. Apatite is also a minor constituent in clastic carbonate sediments as a detrital grain.

Ilmenite

Detrital ilmenite grains have been observed with the SEM-EDX in the matrix of quartz-rich sandstone. Ilmenite grains vary from 15-20 μm in size and are anhedral to rhombohedral in shape (Figure 3.16c). Ilmenite has been recognized as a biomineral. Given its presence in quartz-rich sandstone, it is interpreted as a detrital grain, part of a heavy mineral fraction in sand.

Quartz

The most common occurrence of hydrothermal quartz is probably diagenetic, in the form of anhedral, rounded-to sub-rounded (250-300 μm) grains in matrix. Silty limestones and dolostones have a higher modal abundance (10-15 %) of quartz than carbonates (Figure 3.9c).

Framboidal pyrite

Framboidal pyrites are mainly syn-sedimentary in origin. Secondary electron images taken with the SEM-EDX microscope on framboidal pyrite revealed that individual framboids of 0.5-1 μm in diameter often form larger, spherical grains (10-20 μm). In addition, framboids and larger spherical grains have both been observed within algal mats (300-400 μm) within the dolostone unit (Figure 3.17a). Framboidal pyrites variably occur in clusters interstitial to matrix, in stylolites or as spherical grains (2-3 μm) nucleating on the edges of quartz and calcite grains (Figure 3.17b). Framboidal pyrites are the most abundant (2-5 %) type of pyrites in the Venus lithologies and commonly exceed 5% of modal abundance in stylolites. Algal mats and framboidal pyrites both show later arsenian pyrite and arsenopyrite overgrowth, which demonstrates their early diagenetic origin (Figure 3.17c-d).

Pyrite

Fine-grained (1-2 μm), subhedral pyrite (1 %) is locally present in the matrix in close association with framboidal pyrite or on the edges of calcite/quartz grains (Figure 3.17c) The close association of fine-grained, subhedral pyrite with framboidal pyrite, quartz and calcite grains suggests an early diagenetic stage for this subhedral pyrite as well.

LATE DIAGENETIC or "MVT-TYPE" STAGE

Galena

Several galena occurrences have been found in the Einarson Property. In addition the Birkland drilled prospect located 15 km north from the Venus Zone was explored for Pb-Zn-Ag Mississippi Valley-type mineralization in the 1970s (Shearer, 1976), with mineralization located in zebra-dolostone within the upper Algae Formation (Moynihan, 2014). Galena showings have also been found within the Venus Zone in partly silicified, massive dolostone. In hand sample, this galena exhibits a sheared appearance (Figure 3.18a). In thin section, one large (5 cm), massive galena grain shows slightly curved, fractured surfaces towards the edge of the grain, whereas perfect cubic cleavages are preserved towards the centre of the grain (Figure 3.18b).

PRE-ORE STAGE

Calcite

Pre-ore stage of calcite is manifested by the presence of dissolution texture, which is a result of decarbonatization. Decarbonatization in thin section is characterized by subhedral, coarse-grained (500-1000 μm), calcite-dolomite grains in fine-grained (<1 μm) calcite cement (Figure 3.12e). Samples with dissolution textures do not exhibit intense mineralization, but when they do, mineralization is always interstitial. Therefore, it is interpreted that dissolution breccia calcite is pre-ore stage.

Quartz

Pre-ore stage quartz appears as a form of alteration. Silicified dolostones constitute more than 90 % quartz. Anhedral, medium-grained (200-300 μm) quartz grains form interlocking matrix (Figure 3.19a). In partly silicified dolostones, silica flooding of matrix is common. Silica flooding is characterized by fine-grained (1 μm), aphanitic quartz that makes up the matrix between relict calcite grains (Figure 3.19b). Quartz pseudomorphs after calcite are locally present, and the original rhombohedral crystal outlines of calcite are preserved (Figure 3.19c). Back-scattered electron images revealed subhedral, 200-300 μm diameter quartz grains in silicified dolostone with arsenopyrite and scorodite overgrowth, respectively. This demonstrates that silicification is pre-ore stage (Figure 3.19d).

Pyrite

Subhedral, medium-to coarse-grained (50-100 μm), locally fractured, anhedral pyrite is present in matrix (Figure 3.20a-b). Some massive grains (30 μm) of subhedral pyrite appear to have been pseudomorphed by marcasite and exhibit a strong, blue-green anisotropy. The modal abundance of pyrite varies; however, in general, anhedral, fractured pyrite is the least abundant (<1%) and marcasitized pyrite (1 %) is the most abundant, respectively. Marcasitized pyrites often exhibit arsenian pyrite overgrowth, which demonstrates their pre-ore stage position in the paragenetic sequence (Figure 3.20c). The presence of realgar within the fractures of some pyrite shows that fractured pyrites were present before realgar, which also

suggests an early stage in the paragenesis, since realgar in most Carlin systems is typically post-ore stage (Figure 3.20d).

Marcasite

Marcasite pseudomorphs of pyrite are the most common occurrence of marcasite; however, locally anhedral-to subhedral coarse-grained (50-70 μm) marcasite also occurs (Figure 3.21a). High abundances (10%) of marcasite are particularly common in sheared, clay-altered dolostones, where marcasite occurs as coarse (100-170 μm), subhedral grains, and often exhibits pitted-texture with gangue inclusions (Figure 3.21b). The paragenetic relationship between marcasite and other sulphide minerals has not been observed explicitly; however, marcasite would generally appear to post date pre-ore stage pyrite.

ORE-STAGE

Arsenian pyrite

Arsenian pyrite is strongly associated with elevated gold values and with free native gold in samples examined to date. It thus appears to be a clear marker for the gold-forming ore-stage event in the Venus Zone. The presence of arsenian pyrite was confirmed by BSE imaging and by EDX spectral analysis in which arsenian pyrite displays characteristic excess As content and Fe deficiency. Arsenian pyrite occurs as narrow, 1-2 μm wide rims on pre-existing framboidal pyrite and marcasitized pyrite (Figure 3.22a-b). BSE images showed that the narrow rims of arsenian pyrite form an intergranular, porous texture (Figure 3.22c). The overall modal abundance

of arsenian pyrite is difficult to estimate due to its fine-grained nature. Further, not every framboidal pyrite and marcasitized pyrite exhibit arsenian pyrite overgrowth. However, where arsenian pyrite is present, it constitutes 1-2 % of the modal abundance in these sections. Under reflected light, some framboidal pyrite shows a "fuzzy rim" at high magnification (Figure 3.22d). This texture forms from the overgrowth of arsenian pyrite on framboidal pyrite or marcasitized pyrite, which is then overgrown by arsenopyrite. This texture is indicative of the presence of arsenian pyrite and shows that arsenian pyrite predates arsenopyrite.

Arsenian pyrite pseudomorphs after arsenopyrite have also been observed in realgar and orpiment veinlets. Prism-shaped, 2-3 μm in size arsenian pyrite crystals are present as inclusions in realgar and orpiment (Figure 3.23a). The arsenian pyrite pseudomorphs after arsenopyrite may be explained by the presence of a second-generation arsenian pyrite. This second-generation arsenian pyrite may have replaced ore-stage arsenopyrite during the incipience of arsenopyrite replacement by realgar and orpiment (Figure 3.23b).

The arsenian pyrite rim has been detailed by SEM-EDX-BSE elemental maps (Figure 3.24a-b). Submicroscopic free gold (1-2 μm) particles have been identified nucleating on the edge of arsenian pyrite (Figure 3.25a). The presence of free gold particles on arsenian pyrite rim further confirms that arsenian pyrite is the Au-bearing ore-stage indicator mineral in the Venus Zone.

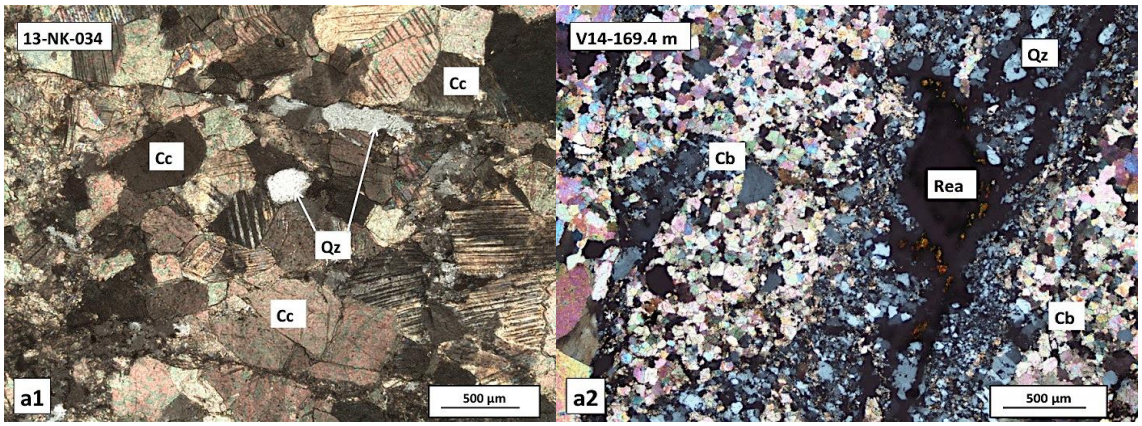

Figure 3.16. A., Calcite-rich matrix (1) versus dolomitized matrix in dolostones (2). Note realgar in example A_2.

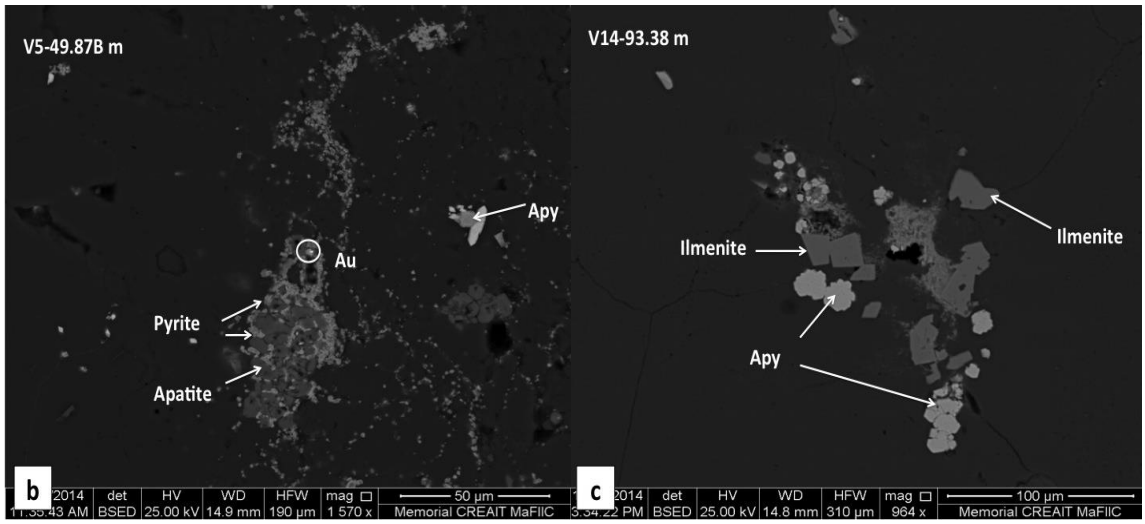

Figure 3.16. B., SEM-EDX, BSE image of apatite grain in close association with framboidal pyrite and gold. C., SEM-EDX-BSE image of ilmenite grains with later arsenopyrite in sandstone.

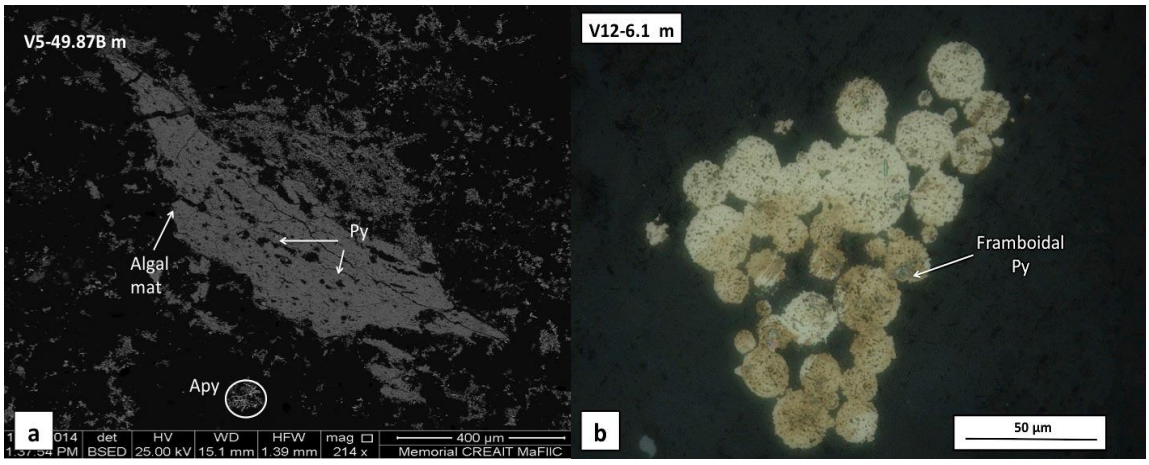

Figure 3.17. A., SEM-EDX BSE image of algal mat with framboidal pyrite. See higher magnification image in 3.17.C. B., Framboidal pyrite cluster under reflected light.

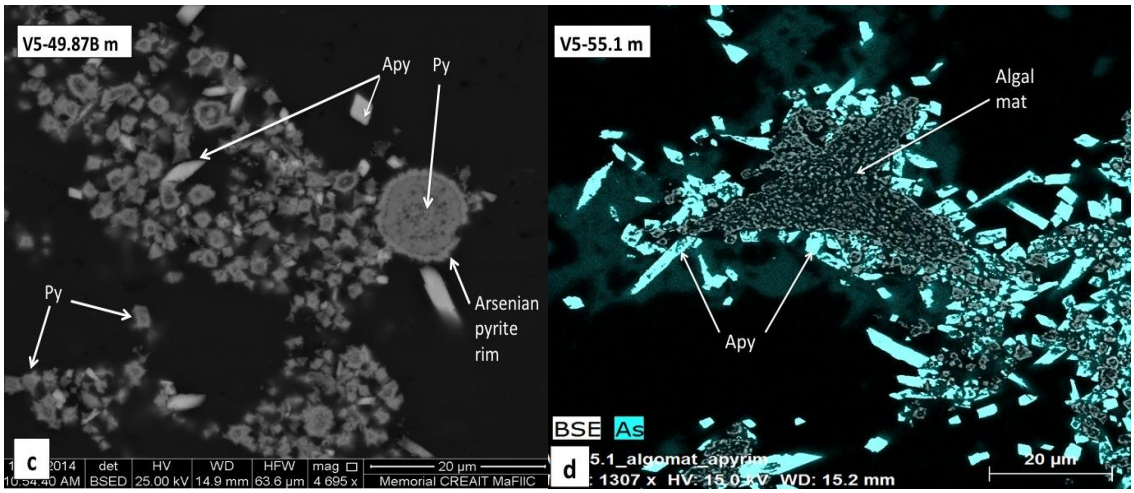

Figure 3.17. C., Framboidal pyrite with arsenian pyrite and arsenopyrite overgrowth. D., SEM arsenic map of algal mat demonstrating the arsenopyrite overgrowth on algal mats.

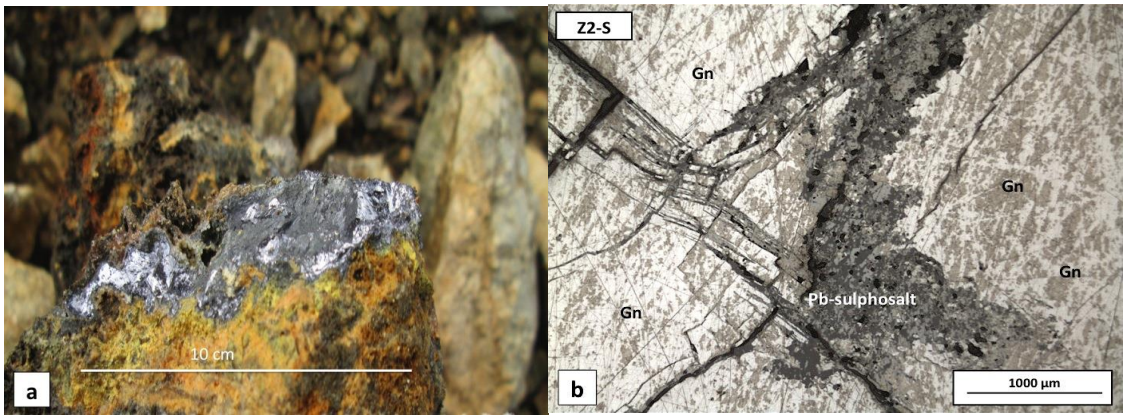

Figure 3.18. A., Sheared galena in hand sample. B., Galena in thin section with late-stage Pb-sulphosalt veinlet.

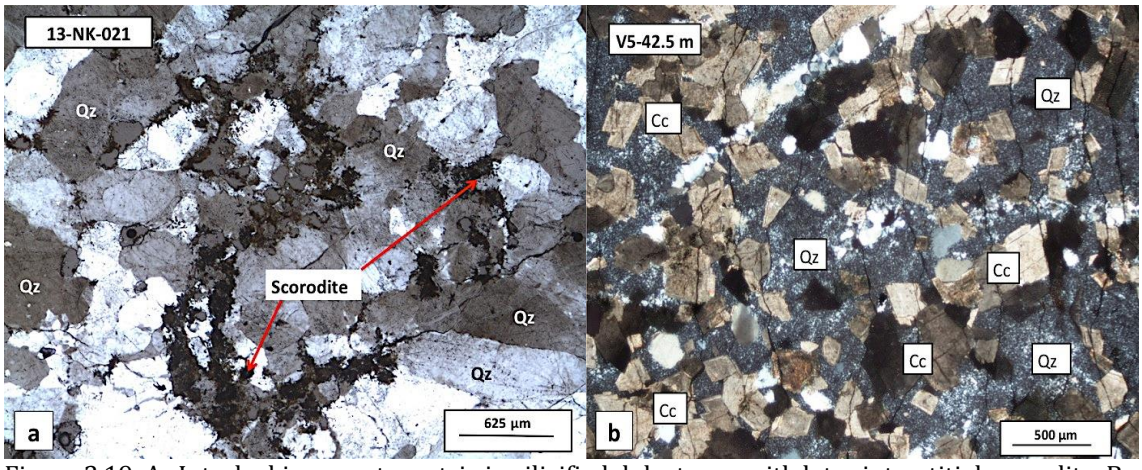

Figure 3.19. A., Interlocking quartz matrix in silicified dolostones with later interstitial scorodite. B., Silica-flooding of carbonate matrix in partly silicified dolostone.

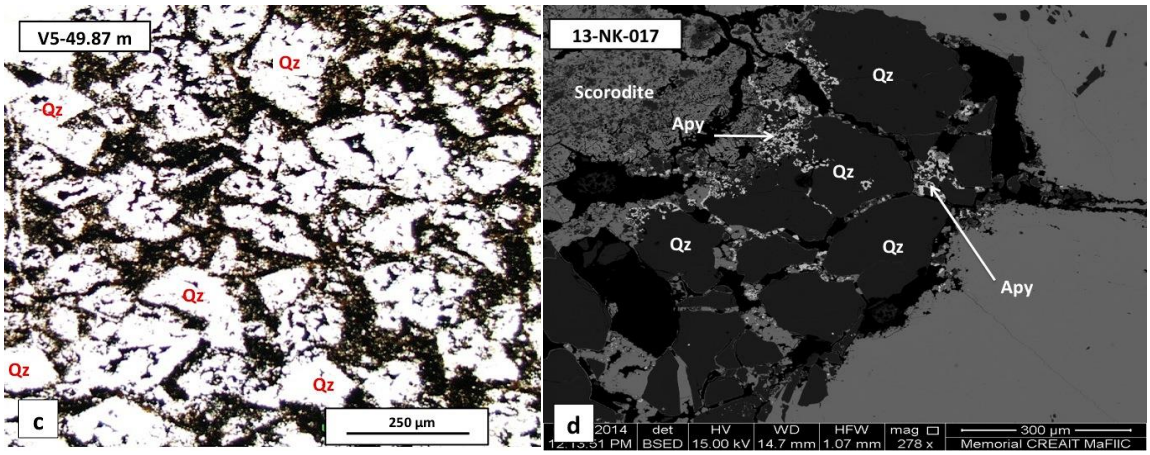

Figure 3.19. C., Quartz pseudomorph after calcite in plane polarized light. D., Quartz grains in scorodite veinlet with arsenopyrite rim indicating pre-ore stage silicification.

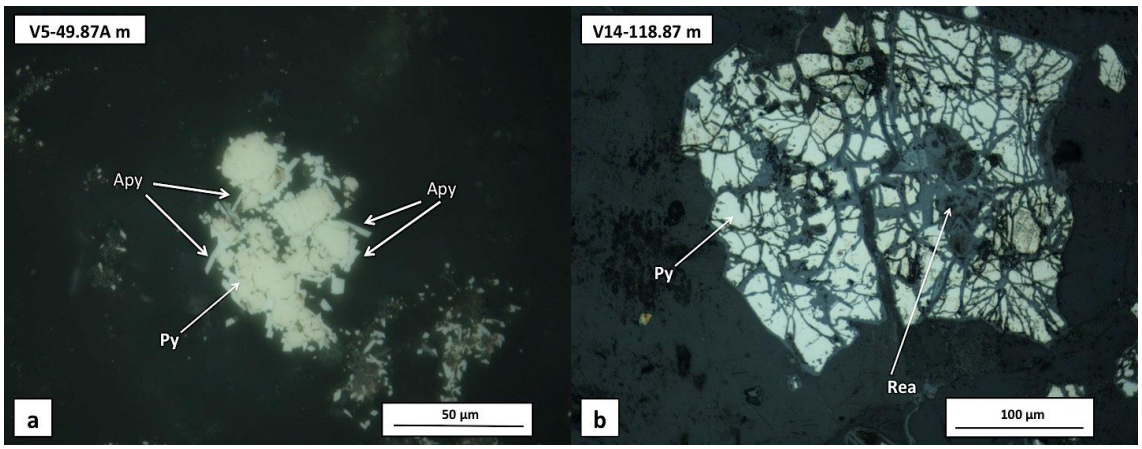

Figure 3.20. A., Subhedral pyrite with arsenopyrite overgrowth. B., Fractured pyrite under reflected light. See also Figure 3.20.C, below.

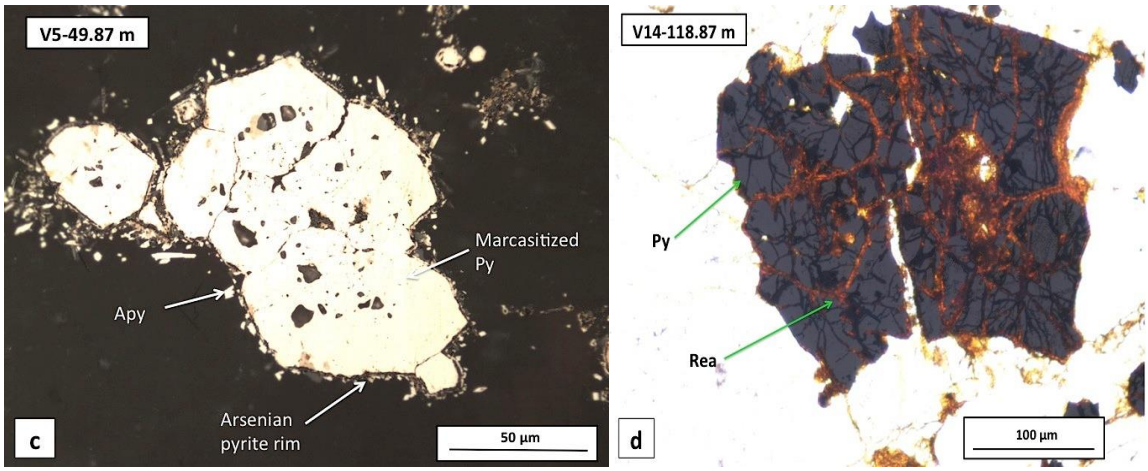

Figure 3.20. C., Marcasitized pyrite with arsenian pyrite rim and arsenopyrite overgrowth. D., Fractured pyrite under partially crossed polars showing the realgar replacement of pyrite.

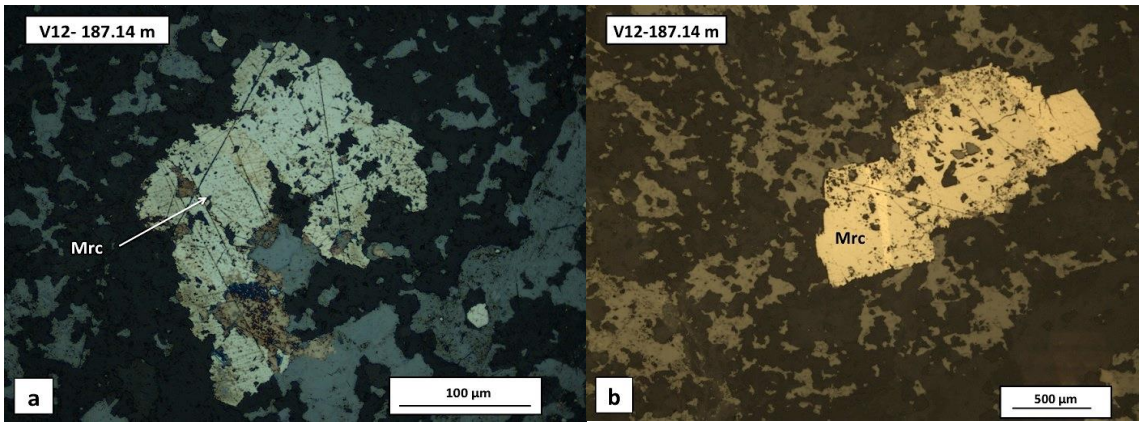

Figure 3.21. A., Anhedral marcasite grain in strongly clay altered dolostone. Pitted marcasite grain with gangue inclusions.

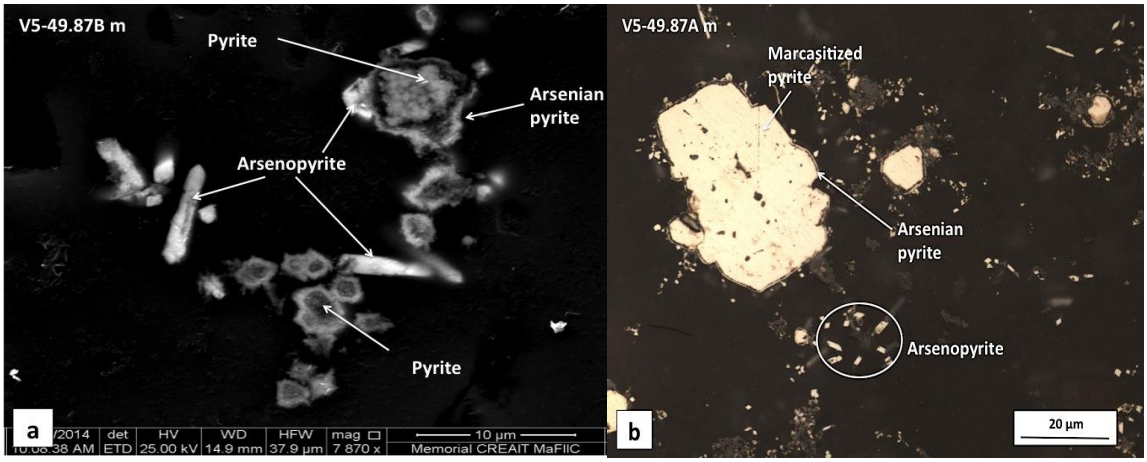

Figure 3.22. A., Arsenian pyrite overgrowth on framboidal pyrite, SEM-EDX, BSE image. B., Arsenian pyrite overgrowth on marcasitized pyrite, reflected light.

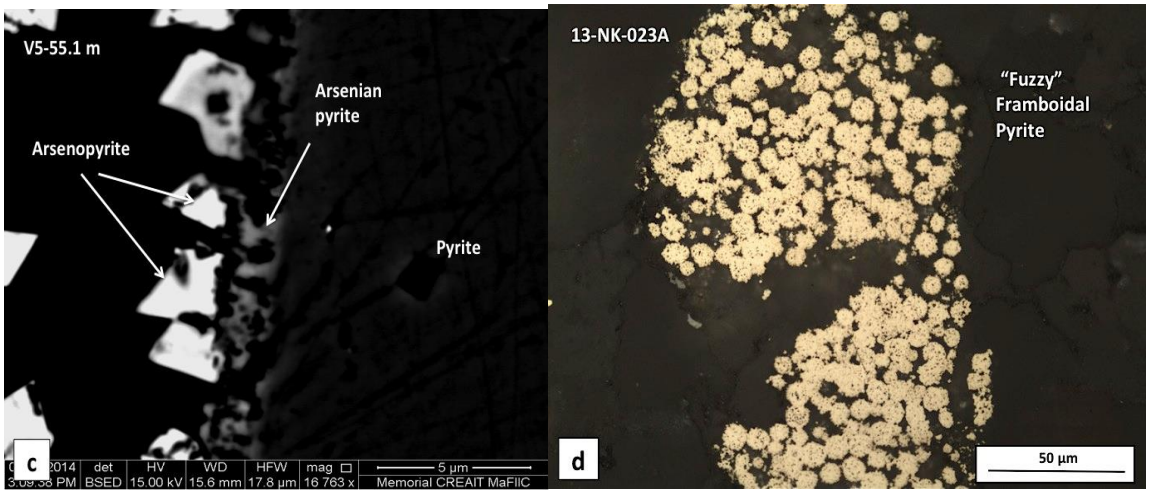

Figure 3.22. C., SEM-EDX, BSE image showing the intergranular, porous nature of arsenian pyrite rim. D., "Fuzzy", framboidal pyrite in matrix.

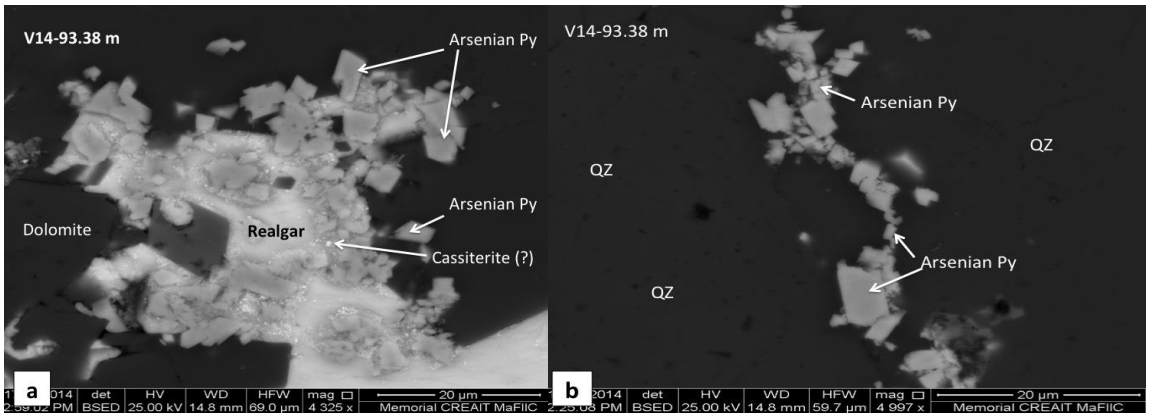

Figure 3.23. A., Arsenian pyrite pseudomorph after arsenopyrite in realgar. B., Arsenian pyrite pseudomorph after arsenopyrite in realgar veinlet.

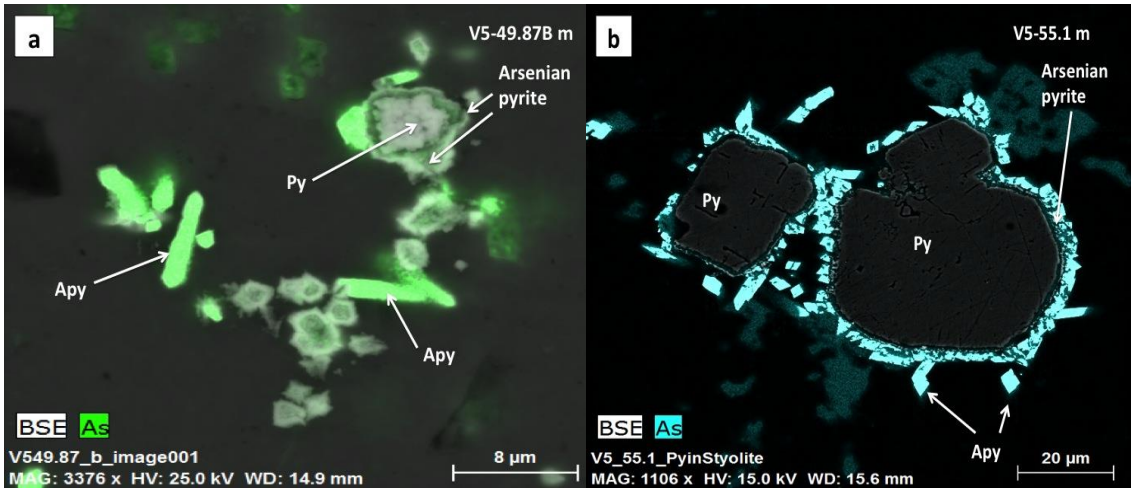

Figure 3.24 A. SEM-EDX, BSE map of framboidal pyrite showing arsenian pyrite-rich rim. B., SEM-ED, BSE map of marcasitized pyrite, showing arsenian pyrite rim.

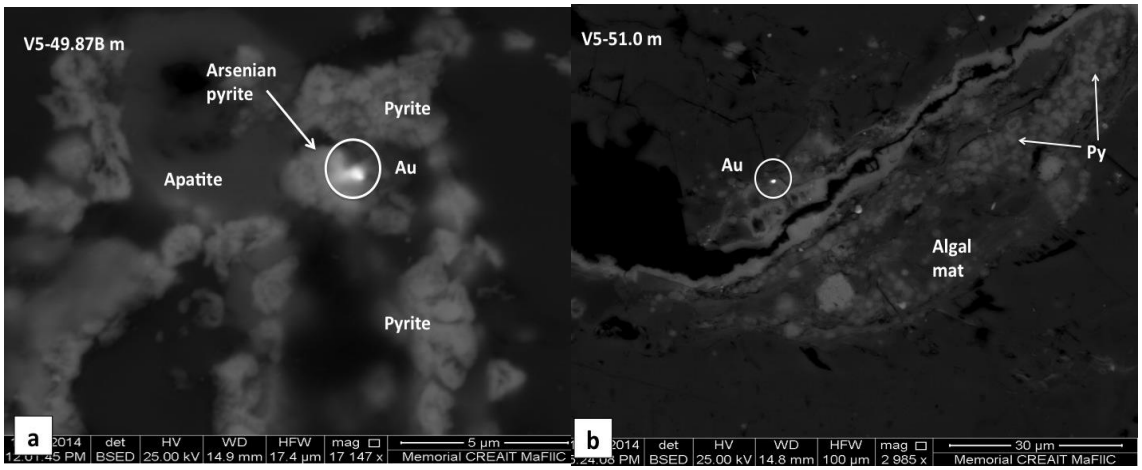

Figure 3.25. A., Submicroscopic free gold nucleating on the rim of arsenian pyrite in silicified dolostone. B., Native free gold in algal mat.

Native Gold

Fine-grained (1-2 μm), native gold has been observed in close association with arsenian pyrite in silicified dolostone (Figure 3.25a). In addition, fine-grained (<1 μm), native free gold particles have also been located in remnants of algal mats within stylolites (Figure 3.25b). Previous studies have established that gold in arsenian pyrite is structurally bound (Au^1) or occurs as submicroscopic inclusions of free gold (Au^0) (Simon et al., 1999). Therefore, based on the presence of arsenian pyrite rims and previous studies, fine-grained native gold observed in silicified dolostones from the Venus Zone also represent Carlin-style ore-stage mineralization.

Arsenopyrite

Ore-stage arsenopyrite exhibits a great textural variety. Most commonly it is characterized by euhedral arsenopyrite overgrowth on arsenian pyrite rims (Figure 3.26a). The same texture is also present as inclusions within realgar and orpiment veinlets (Figure 3.26b). This relationship clearly indicates that ore-stage arsenopyrite is being replaced by realgar and orpiment. Furthermore, the direct replacement of ore-stage arsenopyrite by realgar has been observed in sandy dolostones (Figure 3.26c). In such grains, a small (1 μm), vestigial euhedral arsenopyrite grain is present within a larger (50-60 μm) grain, which has been replaced by realgar. Scorodite pseudomorphs after arsenopyrite occur in scorodite veinlets, which exhibits spar shaped textures that nucleate interstitially between

quartz grains. Spectral analysis confirmed that the spar shaped texture on the edges of scorodite veinlets is the result of the pseudomorphic shape of arsenopyrite prisms (Figure 3.26d). Arsenopyrites also occur in clusters or as individual, sometimes zoned, prismatic crystals (1-2 μm) or long (50-100 μm), prisms, dominantly in dolostone host rock (Figure 3.27a-b). Fleet and Mumin (1997) reported that a substantial fraction of Au in CTGDs is present as "invisible gold" in arsenian pyrite and arsenopyrite. The close association of arsenopyrite to arsenian pyrite and previous studies, including Fleet and Mumin (1997), suggest that euhedral arsenopyrite overgrowth may also represent ore-stage Carlin-style mineralization.

POST-ORE STAGE

Native Gold

Native gold has been observed as apparent residuum of 3-25 μm size grains in scorodite veinlets that formed by the replacement of arsenian pyrite and arsenopyrite (Figure 3.28a-d). This process may explain the high concentration of gold present in scorodite veinlets and scoroditized host and supports the post ore-stage of a second generation of native gold.

Pb-sulphosalts

Two separate Pb-sulphosalt phases have been observed in fractures replacing galena. SEM-EDX spectrum analysis was carried out to determine the composition of the Pb-sulphosalts (Figure 3.29a-b). The analysis revealed that Pb-sulphosalts with elevated W-As and Sb-As in composition are replacing the galena. Antimony and

arsenic are typical Carlin pathfinder elements, and tungsten probably represents a submicroscopic mineral included within the Pb-sulphosalt, because there has not been a Pb-sulphosalt described in the literature with formulaic tungsten. The replacement of galena by Sb-As-rich Pb-sulphosalts is particularly notable in the evolution of a Carlin-type system, because it indicates the replacement of an older, MVT-type event by younger Carlin-like fluids.

Realgar and Orpiment

Realgar and orpiment are abundant in the latest stage of paragenesis of the Venus Zone. In the field, they are often exposed in fault zones or cliff faces and form a distinctive orange-red-yellow weathering (Figure 3.30a). In thin section, realgar and orpiment occur in small veinlets as coarse-grained (40-60 μm), anhedral crystals. The intensity of realgar and orpiment mineralization varies. The most intense realgar and orpiment mineralization can compromise 15-20 % of the modal abundance. Silicified dolostones are less prone to realgar and orpiment mineralization with only 0-5 % of realgar-orpiment in matrix. The paragenetic relationship between realgar and orpiment is unclear. In a few samples, realgar occurs overgrown or replaced by orpiment; therefore, it is concluded that realgar is an earlier stage than orpiment (Figure 3.30b). Realgar and orpiment almost always have arsenopyrite inclusions, confirming their post-arsenopyrite occurrence (Figure 3.26b). In addition, realgar locally has inclusions of anhedral, fractured pyrite (Figure 3.20d). The presence of pyrite and arsenopyrite inclusions in realgar and

orpiment may be indicative of a late hypogene/supergene process that replaced these earlier phases with realgar and orpiment.

Scorodite

Scorodite ($FeAsO_4.2H_2O$) in the field is commonly associated with silicified rocks and occurs as pale green-to yellow-weathered, earthy, clay-like texture with no visible crystalline affinities (Figure 3.31a-b). In thin section, scorodite occurs in thin (1 cm), irregular veinlets with felty texture cross-cutting the matrix (Figure 3.31c). Scorodite veinlets exhibit a great textural diversity. They locally occur as spar-like forms as a result of pseudomorphing arsenopyrite crystals (Figure 3.26d). In addition, acicular and colloform textures have also been observed (Figure 3.31d). The pseudomorphous nature of scorodite after arsenopyrite indicates the post-ore timing of scorodite. Coarse-grained (10-25 μm) free gold particles have been located in scorodite veinlets (Figure 3.27a-d). In fact, almost every scorodite veinlet that has been observed contained native gold. The presence of free gold in scorodite veinlets was further discussed under *Post-ore stage/Native Gold* above.

Cinnabar

Cinnabar has been identified in a few places in the field as dark red, fine-grained, prismatic crystals (Figure 3.32a). Under SEM-EDX analysis, cinnabar exhibits anhedral-to subhedral, fine-grained (1-3 μm) crystals in close association with an unidentified Al-Si-O phase. More commonly, cinnabar grains have been identified in stylolites and fractures forming thin (1-2 μm) veinlets (Figure 3.32b). No

paragenetic relationship has been established between cinnabar and other minerals; however, the occurrence of cinnabar in fine veinlets and in fractures suggests a later post-ore stage.

Native Arsenic

Native arsenic has been found once in the matrix of silicified dolostone, using BSE-EDX. The grain is anhedral, 25-30 μm in diameter with a Bi-rich core (Figure 3.33). This grain does not show any obvious paragenetic relationship to other ore or gangue minerals; therefore, its position in the sequence is unknown. However, based on $fS_{2\,(g)}$-$fO_{2\,(g)}$ diagram (Figure 3.47) showing the stability fields of mineral assemblages, it is suggested that native arsenic may have precipitated during the latest stage of Carlin-style mineralization.

Quartz

This stage of quartz is not the same stage as pre-ore stage silicification, but a later post-ore stage, which occurs in the latest of paragenesis. In the field, a mixture of cross-cutting quartz-carbonate veinlets commonly occur on fractured surfaces or perpendicular to bedding, sometimes forming boxwork silicification texture (Figure 3.34a). In thin section, this stage is characterized by thin quartz veinlets cross-cutting both the matrix and pre-existing realgar veinlets. Realgar veinlets are also brecciated and replaced by quartz (Figure 3.34b). In hand sample, the replacement of realgar can be seen as quartz veinlets having a thin residual vein of realgar within them. In thin section, cross-cutting quartz veinlets are generally 200-500 μm in

width and have anhedral, medium-grained (200-300 μm) quartz. Realgar grains and veinlets are often rimmed by quartz. The cross-cutting relationships of this generation of quartz veins demonstrates that silicification manifested by boxwork-textured quartz veinlets is post-ore stage.

Calcite

Post–ore stage calcite veining is more common in sandy dolostone and silty oolitic limestones than in other lithologies present in the Venus Zone. In the field, quartz-carbonate veinlets, 1-2 cm in width occur parallel or perpendicular to bedding. Bladed calcite veins have locally been observed (Figure 3.35a). In thin section, multiple generation of cross-cutting calcite veinlets from 10-to 500 μm in width occur as medium (200-500 μm), anhedral grains (Figure 3.35b).

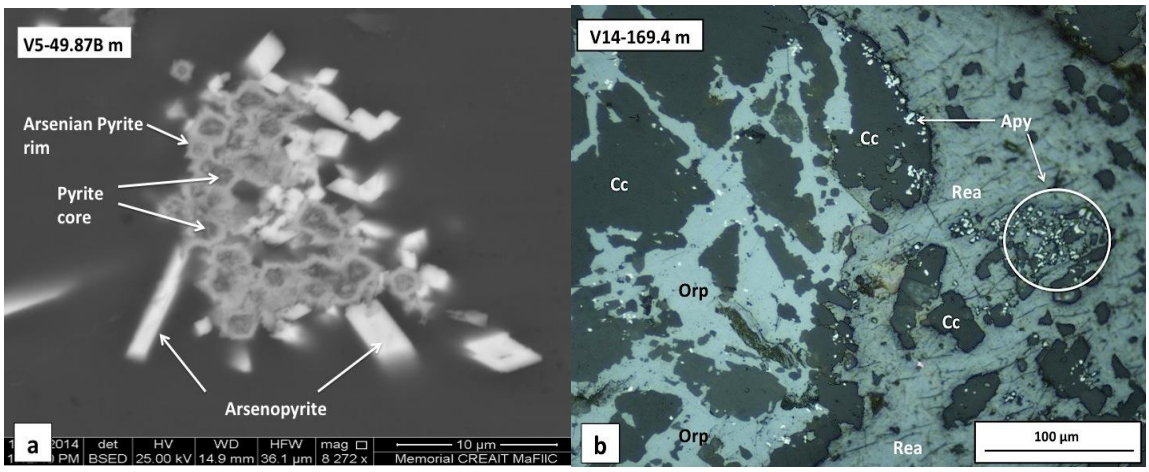

Figure 3.26. A., Ore-stage arsenopyrite overgrowth on arsenian pyrite rim. B., Ore-stage arsenopyrite inclusions in realgar and orpiment veinlets in non-silicified dolostone.

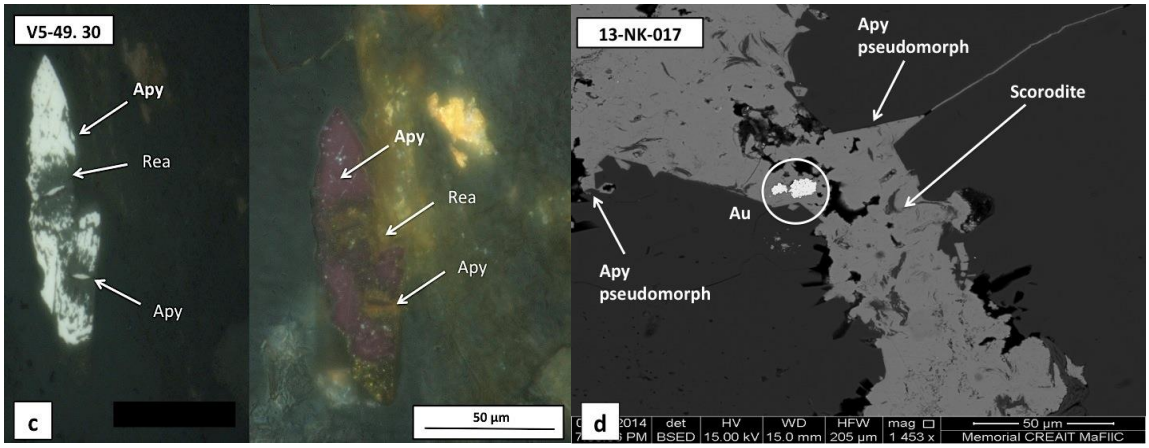

Figure 3.26. C., Multiple nucleation of arsenopyrite. Image with partially crossed polars showing the direct replacement of ore-stage arsenopyrite by realgar. D., Scorodite pseudomorph after ore-stage arsenopyrite in silicified dolostone, SEM-EDX, BSE image.

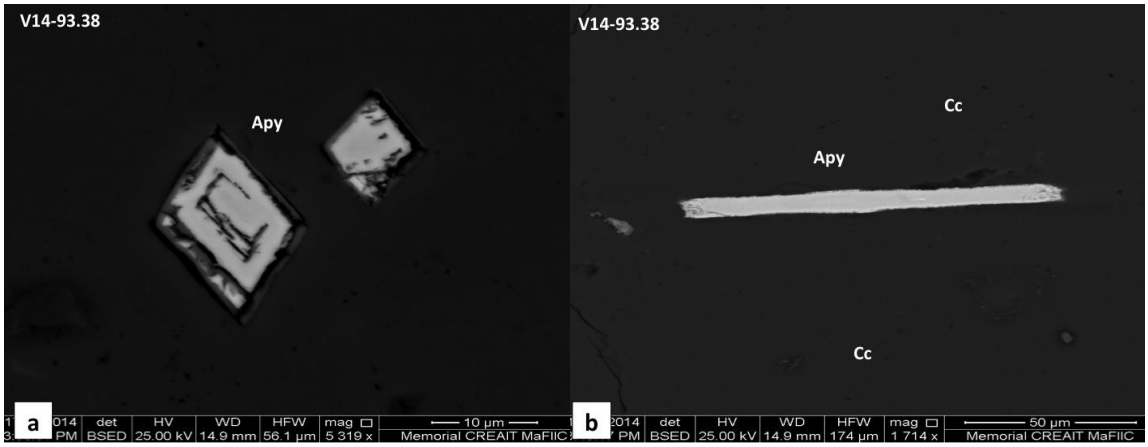

Figure 3.27. A., Zoned arsenopyrite grains in calcareous sandstone. B., Needle-like crystals of arsenopyrite in calcareous sandstone.

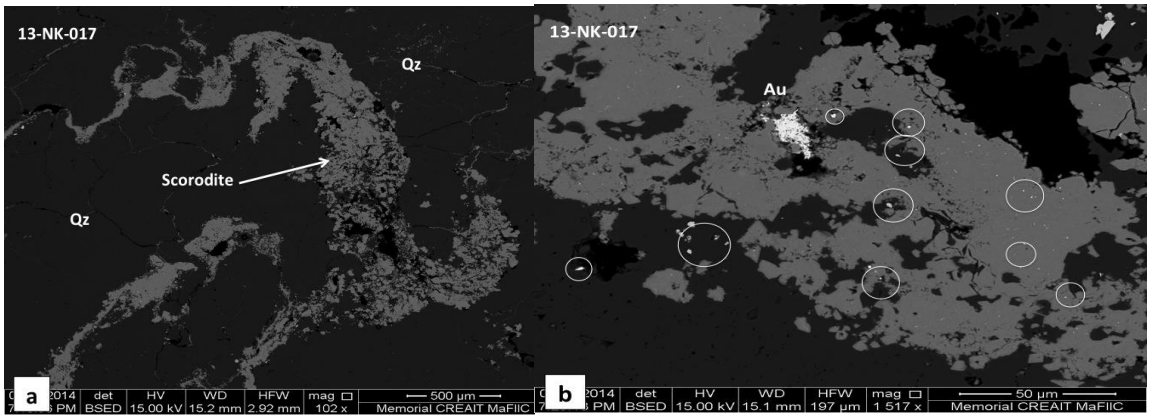

Figure 3.28. A., Au-bearing scorodite veinlet in silicified dolostone. B., Close-up of Figure 3.27. A. Native free gold in scorodite veinlet. Multiple gold grains are circled.

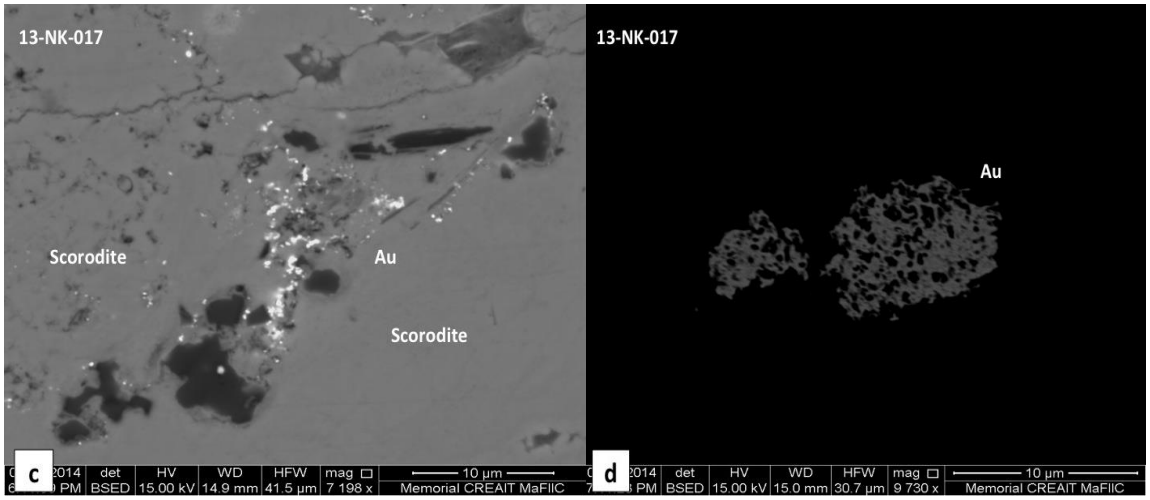

Figure 3.28. C., Native free gold in scorodite veinlet. D., Native free gold in silicified dolostone.

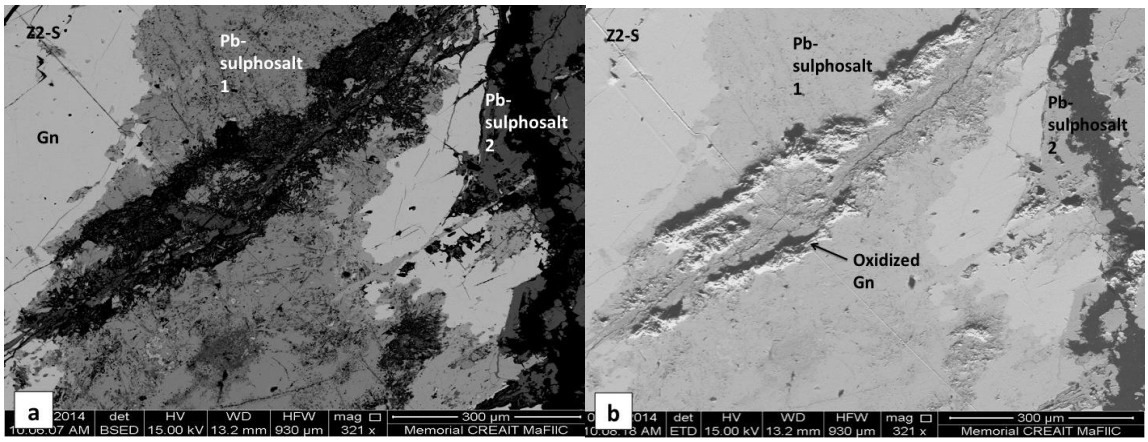

Figure 3.29. A., Galena replacement by Pb-sulphosalts. B., SEM-EDX-SE image showing the topography of Pb-sulphosalts and oxidized galena.

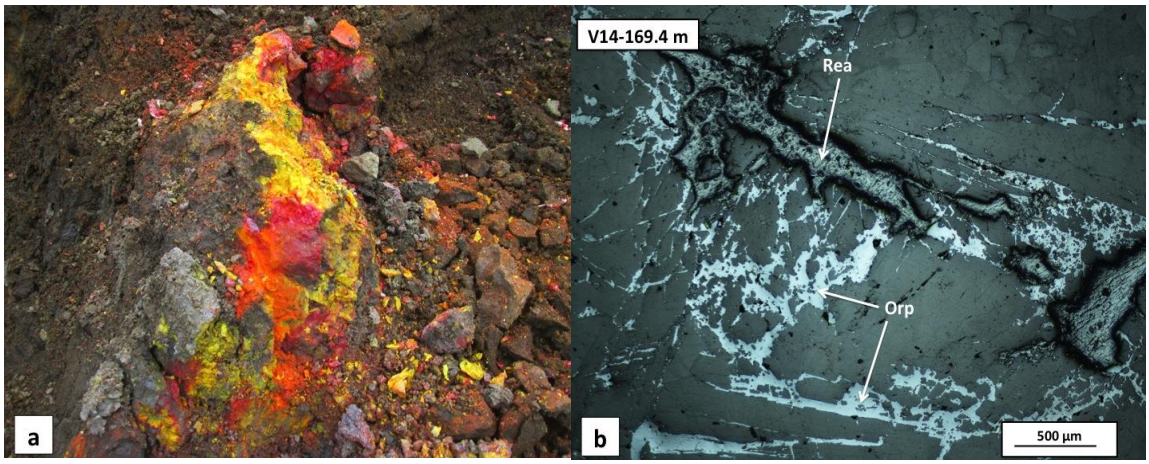

Figure 3.30. A., Realgar and orpiment in outcrop. B., Realgar inclusion in orpiment veinlet.

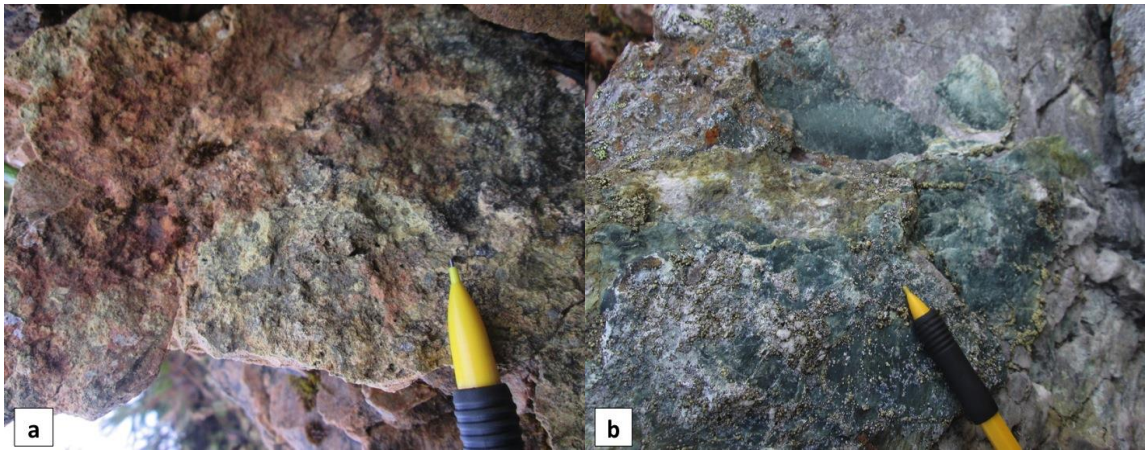

Figure 3.31. A., Scorodite in outcrop. B., Pale green coloured scorodite alteration in silicified dolostone.

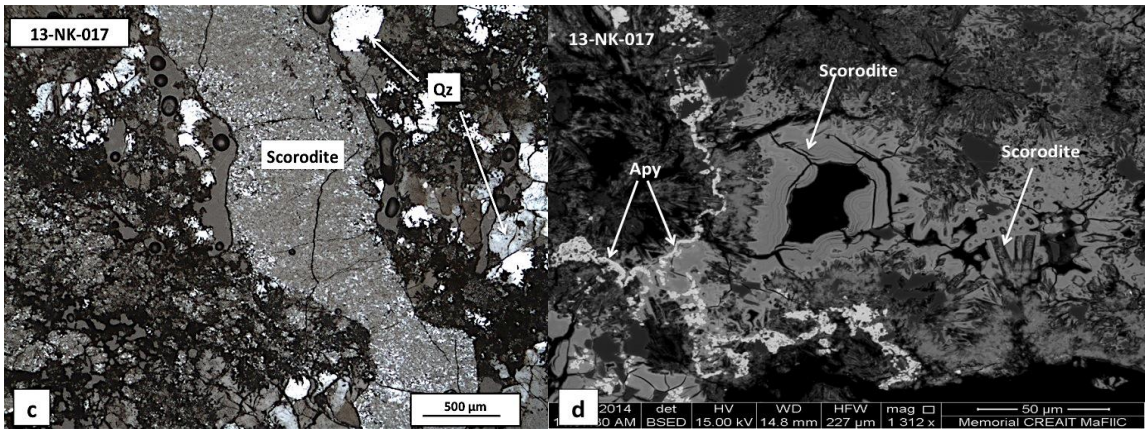

Figure 3.31. C., Scorodite veinlet in silicified dolostone. D., SEM-EDX BSE image showing the colloform and acicular textures of scorodite.

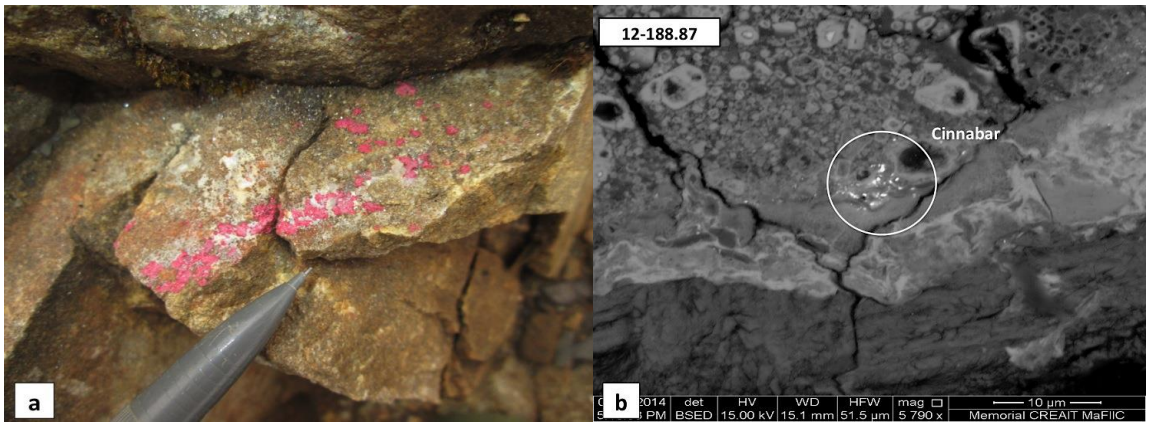

Figure 3.32. A., Cinnabar in outcrop. B., Cinnabar veinlets in stylolites in SEM-EDX BSE image.

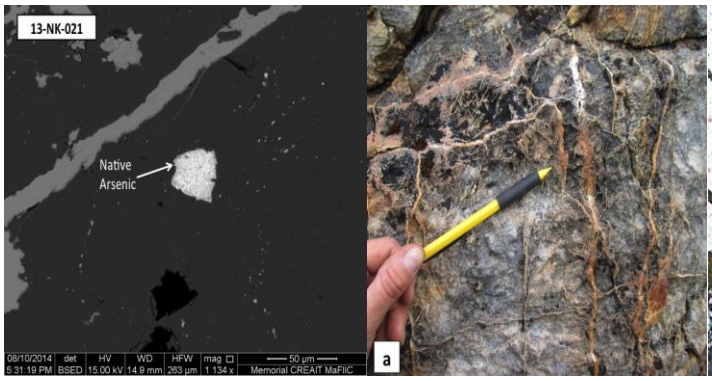

Figure 3.33. Native arsenic grain in silicified dolostone.

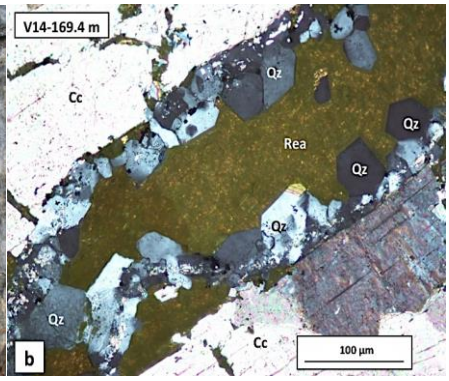

Figure 3.34. A., Quartz veinlet in outcrop, boxwork silicification texture. B., Realgar veinlet replaced by quartz.

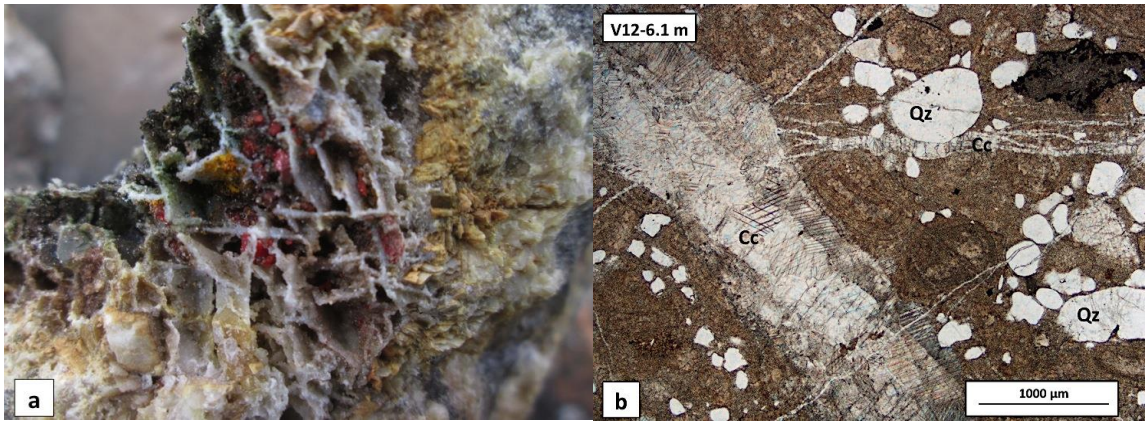

Figure 3.35. A., Bladed post-ore stage calcite veinlets with realgar crystals.
B., Multiple generations of post-ore stage calcite veinlets in silty oolitic limestone.

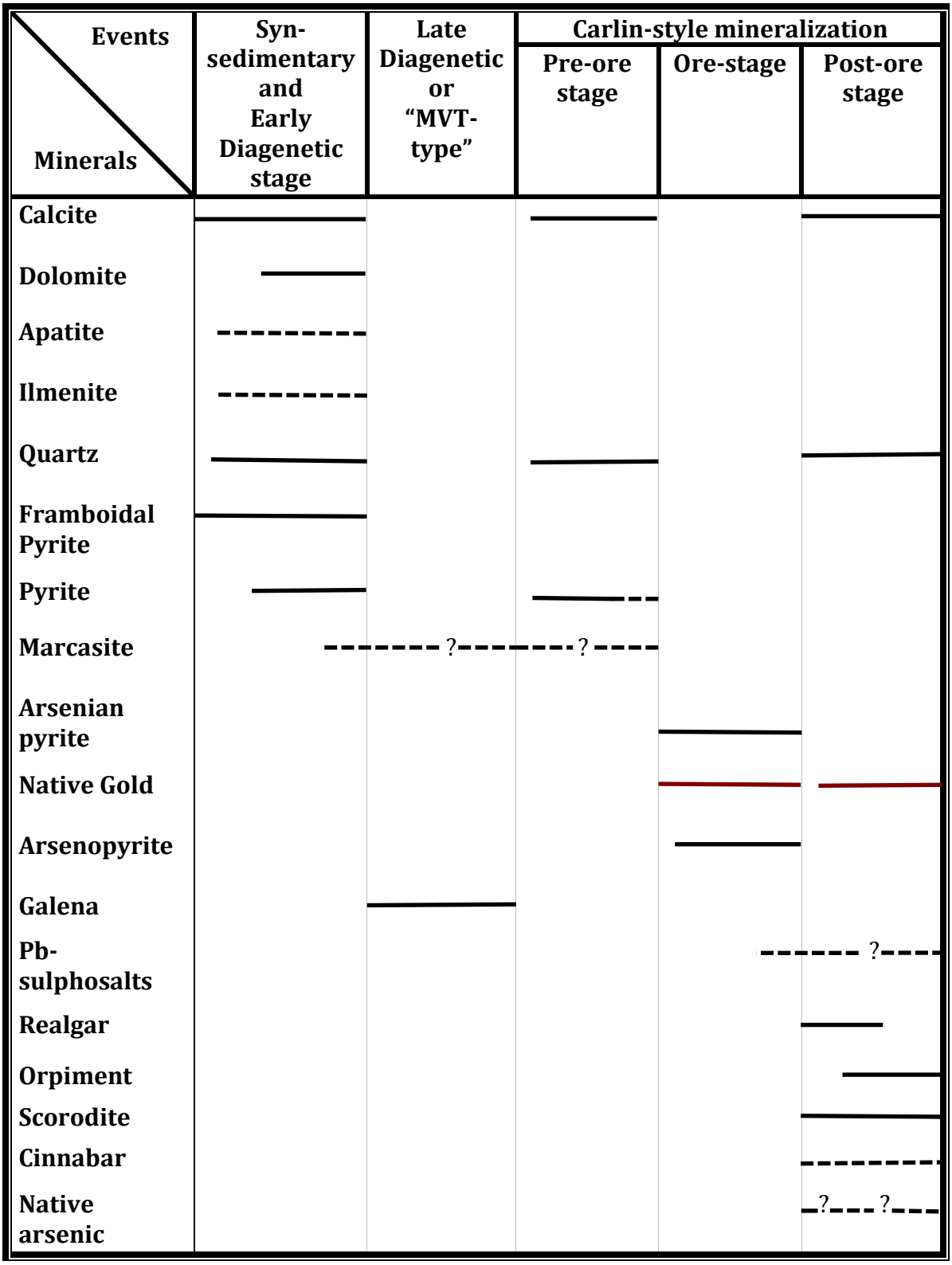

Figure 3.36. Paragenetic sequence of the Venus Zone.

GEOCHEMICAL TRENDS

An extensive rock-chip sampling program was conducted on the Venus Zone along 7 section lines to locate gold mineralized areas in the summer of 2013. In total 413 rock-chip samples were collected with 2 m sample intervals. The samples were analyzed by AGAT Laboratories using a geochemical, 19 multi-element (As, Ag, Au, Be, Bi, Co, Cu, Fe, Hg, Ga, K, Ni, P, Pb, Sb, Se, Te, Tl, Zn) package. The aim of the geochemical plots is to define any correlation between gold and other elements and to determine if these correlations can be used for future exploration. In addition, some elements used in the geochemical plots can show correlation with the paragenetic sequence, which could help to elucidate paragenesis and geochemical signatures of the Venus Zone.

Geochemical background signatures

Samples were separated into two groups based on their gold values. One group contains 31 samples, with gold values in all samples greater than a 100 ppb (Figure 3.37-3.43) (Figure AII.9-AII.13). This group was used to determine if there is correlation between distinct gold mineralization and other elements. The other group has 413 samples with gold values ranging from 0 ppb to 32.6 ppb (Figure AII.1-AII.8). This group was used to determine the geochemical background signatures of the Venus lithologies, because the first group does not provide sufficient data to analyze trends and background values. Furthermore, 4 samples have particularly anomalous Au gold values, which makes the plots skewed to one

side, and limits data interpretation. Geochemical background signatures are particularly important because they indicate the geochemical signature of the unmineralized rocks. It is essential to understand the background values because it helps to identify the true geochemical signatures of the mineralized rocks with application to soil and rock sampling programs. Background signatures were tested for As, Hg, Tl, Sb, Zn, Co, Pb and Ni.

Samples with less than a 100 ppb gold value indicated that Tl and Sb are elevated in non-mineralized lithologies (Figure AII.1-2). Arsenic and mercury showed more variance; however, there are three observations that can be applied for both As and Hg. 1. Lithologies with no detectable gold mineralization have elevated As and Hg. 2. Where gold mineralization is evident (>100 ppb) arsenic and mercury values actually decrease in comparison to non-gold-mineralized samples. 3. There are two distinct clusters in both arsenic and mercury geochemical plots characterized by high Au and Hg or high Au and As values. These clusters may represent the close proximity to gold mineralization, where elevated Hg and As background values are still present (Figure AII.3-4). These three general trends are also evident in the paragenesis. Gold mineralized samples always show lesser realgar and orpiment abundance than arsenic sulphide-bearing samples with no gold mineralization. In addition, gold has been found in samples taken from the drill core 3 m below the highest-grade zone. These samples also compromise arsenopyrite with local realgar and cinnabar, which can explain the elevated Au-As-Hg cluster in the plots. Zinc,

cobalt, lead, and nickel geochemical plots do not show meaningful correlation with gold (Figure AII.5-8).

Gold mineralized samples

Gold mineralized samples are defined here as containing >100 ppb gold. Of the 32 samples in this category, 4 samples are particular anomalous with 32600, 21500, 20000, and 13800 ppb Au, respectively. 11 geochemical plots were used to compare gold mineralization to As, Fe, Hg, Tl, Sb, Ag, Pb, Zn, Co, Cu, and Ni. In general, all geochemical plots outline 2 main trends. One trend (red squares) indicates enrichment in most elements with the exception of Zinc. The second trend (blue diamonds) indicates gold enrichment. These two trends probably represent two separate fluids with different composition. The first trend probably represents supergene/late hypogene fluids, whereas the second trend with highly elevated gold may indicate the hypogene fluids responsible for Ore-stage mineralization (Figures 3.39-3.41).

Arsenic-Iron

The Au-As and Au-Fe plots show two almost identical trends, which can be explained by the different modes of gold occurrence (Figure 3.37-3.38). SEM-EDX revealed that native gold can occur in close association with arsenian pyrite, scorodite, and pyrite-rich stylolites. The three modes of gold occurrence are evident in these 2 plots. Trend 1 shows elevated As-Fe with less gold, which may indicate "invisible gold" in arsenian pyrite. Trend 2 indicates more gold with less As and Fe.

This trend may represent gold in scorodite, where gold is generally coarser-grained (5-25 μm) than in arsenian pyrite (<1 μm). The third trend (Trend 3) may be indicative of gold in pyrite-rich stylolites. In addition, elevated arsenic and gold values also show correlation, which further confirms that gold is associated with elevated arsenic (Figure AI.7).

Antimony-Mercury-Thallium

The Hg-Sb-Tl vs. Au geochemical plots all indicate two main trends (Figure 3.39-3.41). Trend 1 indicates rocks that are highly enriched in Hg-Sb-Tl. Trend 2 shows anomalous Sb-Hg-Tl with highly elevated gold. The two different trends are probably indicative of supergene/late hypogene (Trend 1) and hypogene (Trend 2) fluids. Hypogene fluids deliver ore-stage mineralization, which was the initial residence of gold. Supergene minerals form from the oxidization of primary minerals in a process where descending meteoric water redistributes the ore elements from the oxidization and chemical weathering of primary minerals. Therefore, trend 1 can be representative of the later hypogene or supergene fluids that redistributed antimony, mercury, thallium but left gold as a residue. These observations are echoed in Figure AI.6, where anomalous gold samples are often correlated with elevated mercury and explained as a consequence of hypogene (Trend 2) processes.

Lead

The Pb geochemical plot does not show meaningful correlation with gold (Figure 3.42). However, there is known Mississippi Valley-type (MVT) mineralization in the area and several galena occurrences have been found in the property. Therefore, Pb-enrichment may be a consequence of earlier MVT-type mineralization of the carbonate host rocks, and thus it is not a good indicator for gold mineralization.

Silver

The silver-gold geochemical plot (Figure 3.43) shows similar trends to trends 2-3 in the arsenic and iron plots (Figure 3.37-3.38). One possible explanation for the similarity is that silver could occur dissolved in free gold particles; however, it will not dissolve into arsenian pyrite. Therefore, trend 1 in Figure 3.37-3.38, which represents gold in arsenian pyrite shows low silver values in trend 1 Figure 3.43. However, trend 2 and 3 in Figure 3.37-3.38 representing free gold shows strong correlation with trend 2 and 3 in Figure 3.43.

Zinc

The four most elevated gold samples were omitted from the geochemical plot, because the graph was strongly left-skewed and did not show the rest of the samples. The Au-Zn plot shows a great variance, and does not outline any significant trend (Figure AII.9). A possible explanation for this great variance is that some sedimentary rocks, such as shales have naturally elevated zinc values. Irregular shale beds are present within the dolostones and that may influence the data by

showing irregularity within the plots. Zinc residue thus is interpreted to reflect the composition of pelitic rocks, rather than hypogene hydrothermal mineralization.

Copper, Copper-Arsenic

There has not been a dominantly Cu-mineral observed in the paragenesis; however, Trend 1 in Figure AII.10 based on very limited geochemical data implies that there may have been some mobility of Cu in ore-stage fluids. In addition, arsenic and copper correlations were tested; however, Cu shows no demonstrable correlation with As (Figure AII.11).

Cobalt-Nickel

Cobalt and nickel do not show any correlation with gold (Figure A.II12-13). Therefore, high Ni and Co values are not useful for locating gold mineralization on the Venus Zone.

Summary of geochemical plots

The above outlined geochemical plots are a general representation of the geochemical trends in the Venus Zone, based on 413 rock-chip samples. This geochemical data set was supplied by commercial lab analysis, and thus there is no explicit data error attached to each sample. In addition, only 7 % of the data has gold mineralized samples that are available for interpretation; therefore, most of the trends are inferred due to the lack of sufficient data points. In summary, As, Hg, Sb, and Tl are good spatial indicators and may represent proximity to gold

mineralization. Elevated Zn, Ag, and Pb values do not necessary reflect gold mineralization and should be followed up in the field before further exploration.

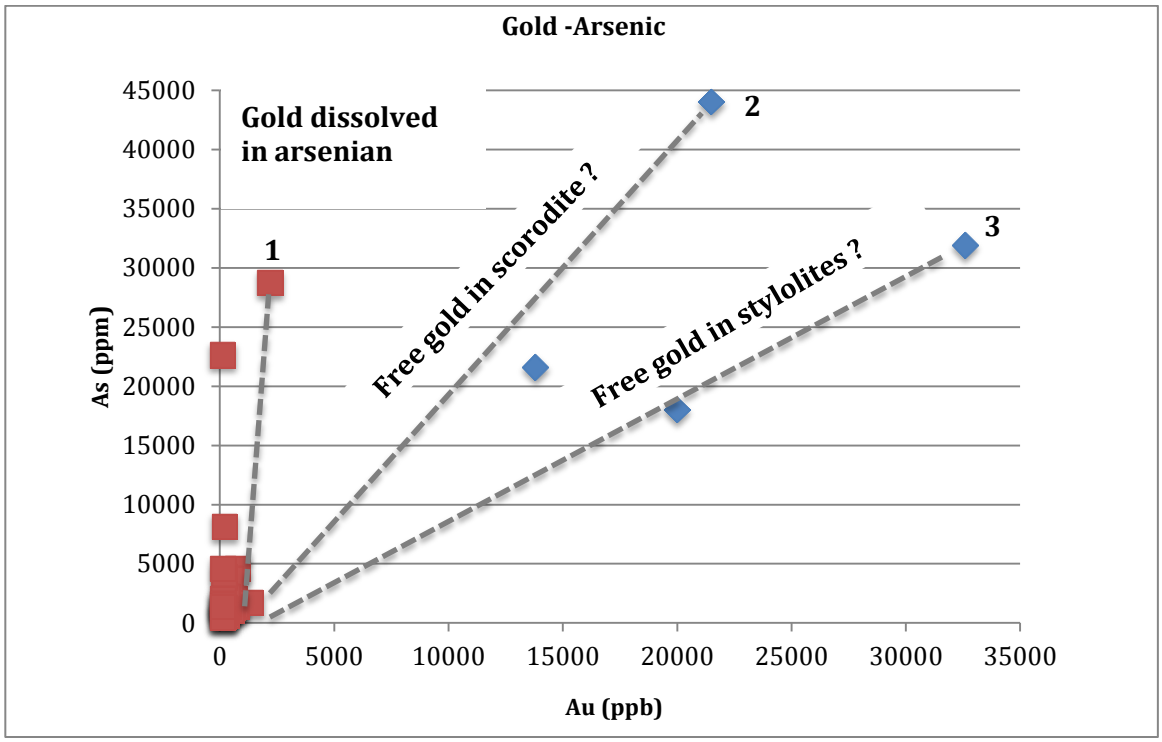

Figure 3.37. Gold-arsenic plot showing the different modes of gold occurrence.

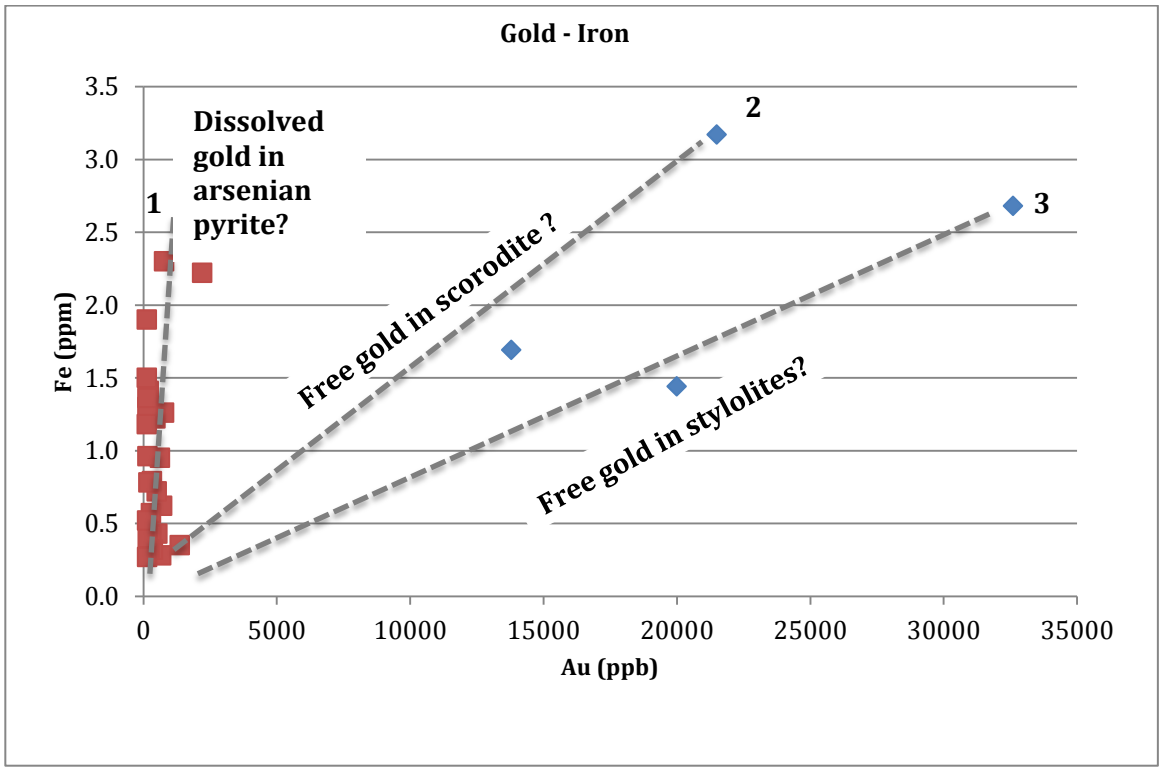

Figure 3.38. Gold-iron plot showing the different modes of gold occurrence.

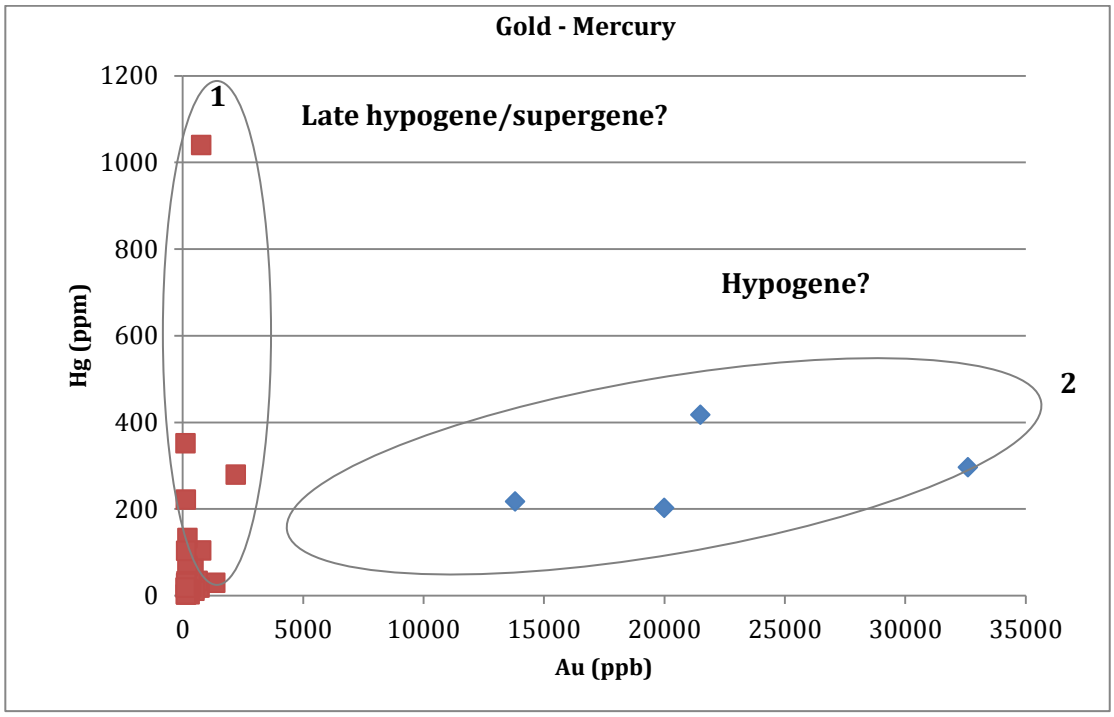

Figure 3.39. Gold-mercury plot indicating the correlation of Au and Hg. Trends may represent hypogene and late hypogene/supergene enrichement of fluids.

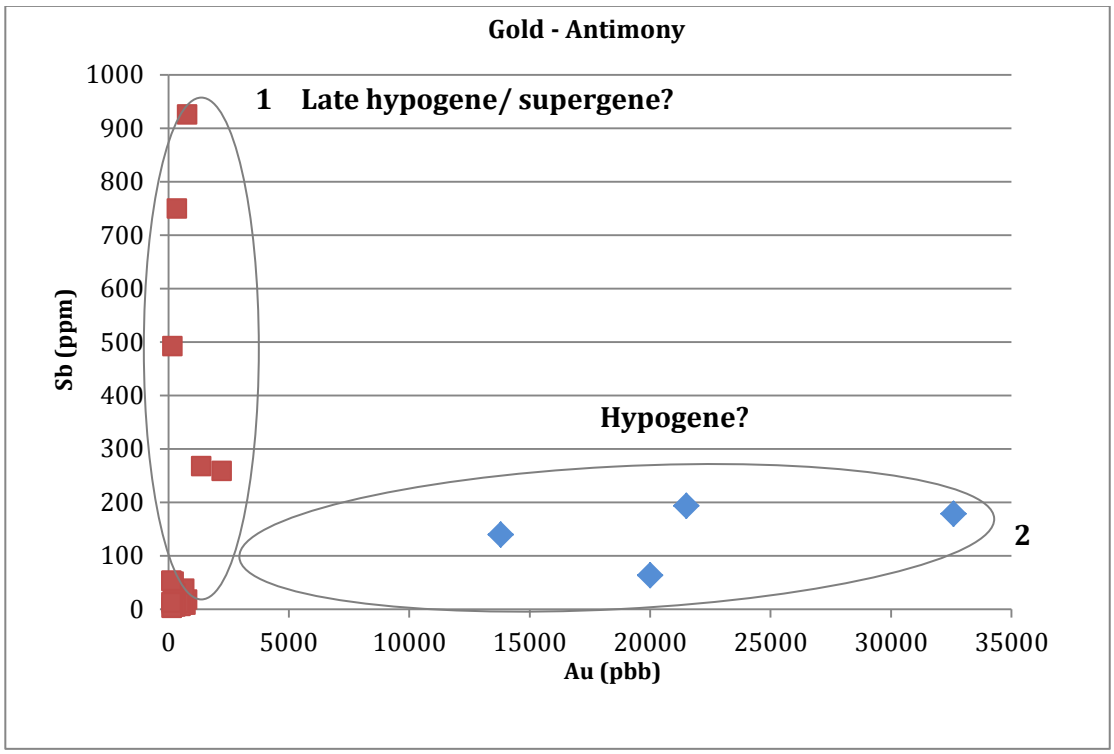

Figure 3.40. Gold-antimony plot indicating the correlation of Au and Sb. Trends may represent hypogene and late hypogene/supergene enrichement of fluids.

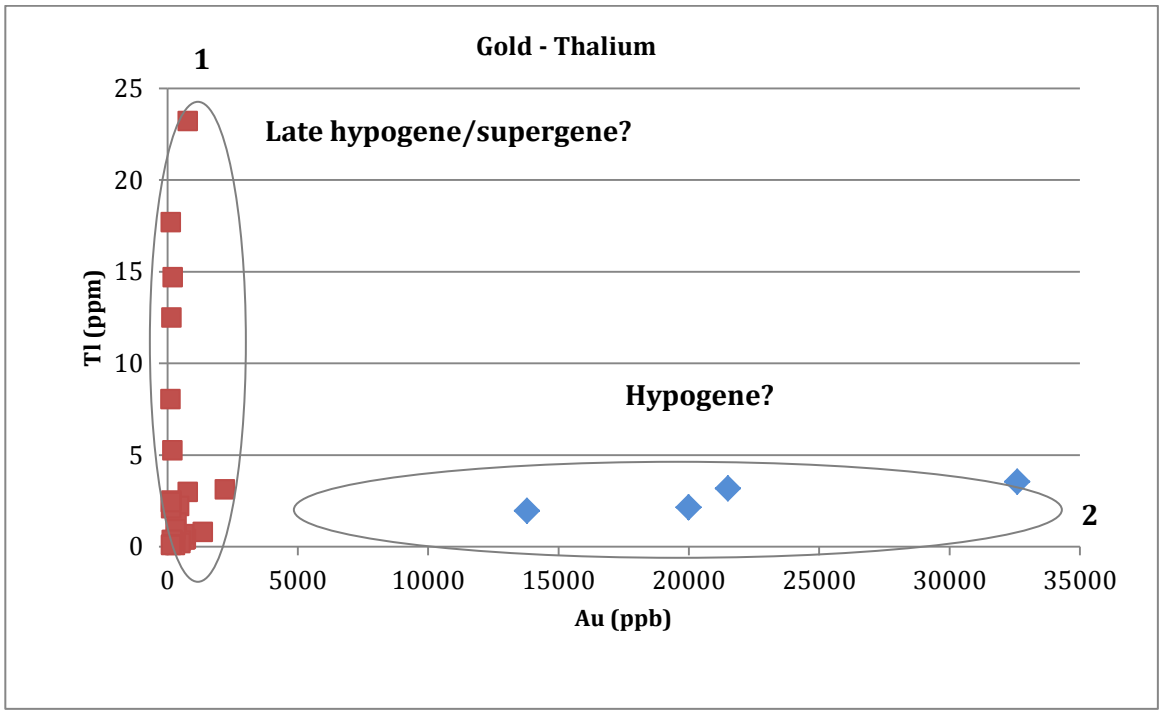

Figure 3.41. Gold-thallium plot indicating the correlation of Au and Tl. Trends may represent hypogene and late hypogene/supergene enrichement of fluids.

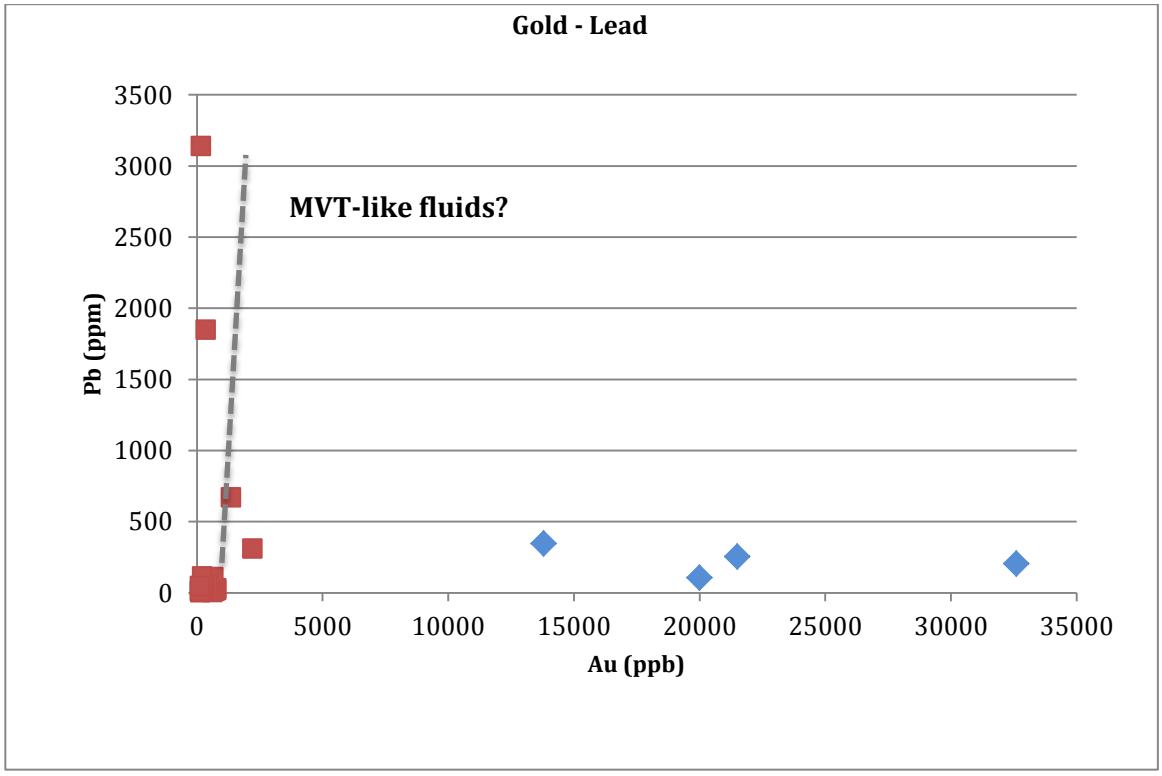

Figure 3.42. Gold-lead plot. The trend may be a consequence of earlier MVT-like mineralization.

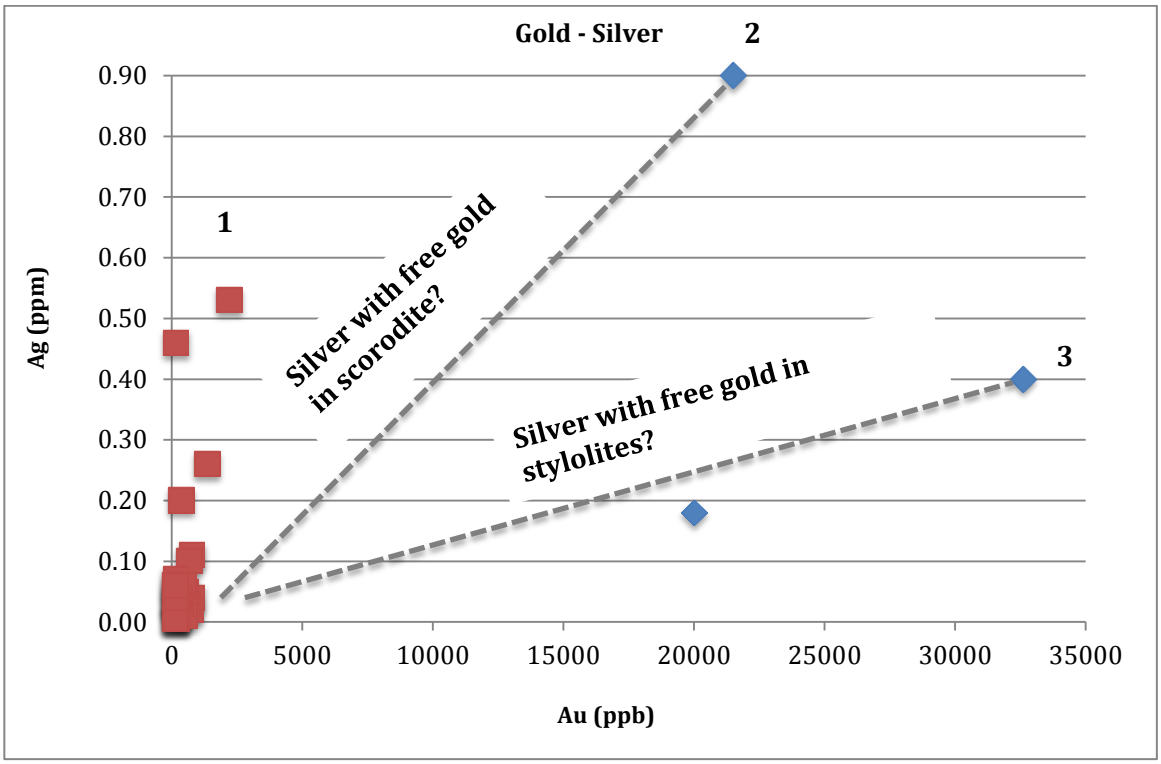

Figure 3.43. Gold-silver plot indicative of native silver may be in association with native gold.

Table 3.1. Summary and comparison of the characteristic features of Carlin-type gold deposits in Nevada and the Yukon Territory, Canada.

Characteristics	Nevada		Nadaleen Trend-ATAC Resources Ltd. Yukon	Venus Zone, Yukon
Tectonic History	• Continental rifting, followed by passive margin sedimentation • Compressional tectonism forming the Roberts Mountains Thrust • Extension-related magmatism		• Continental rifting, • Passive margin sedimentation accumulated clastic sedimentary rocks of Windermere Supergroup and Hyland Group, followed by shelf facies carbonate rocks and deep water sedimentary sequences of the Selwyn Basin • Convergent margin tectonism and back–arc extension • Mesozoic thrusting occurred along the Dawson Thrust	• Continental rifting, • Passive margin sedimentation accumulated clastic sedimentary rocks of Windermere Supergroup and Hyland Group, followed by deep water sedimentary sequences of the Selwyn Basin • Convergent margin tectonism and back–arc extension Mesozoic Thrusting occurred along the Dawson Thrust
Stratigraphical names of host rocks	**Carlin Trend** • Roberts Mountains Formation • Popovich Formation	**Northern Carlin Trend** • Bootstrap Limestone	• **Windermere Supergroup** • Conrad-Nadaleen Formation • Osiris-Gametrail Formation • Anubis-Devonian limestone	• **Hyland group** • Algae Formation
Host rock	Carbonate shelf-slope facies Pyritic, carbonaceous silty to dolomitic limestones	Diagenetic planar dolostone to zebra-textured dolostone Silicified breccias	Slope and basin facies, carbonate, clastic rocks, siltstones with significant amount of deep-water black shale • **Limestone** (Conrad, Osiris, Sunrise, Anubis) • **Dolostone** (Isis) • **Black Shale** (Anubis)	Slope and basin facies, carbonate, clastic rocks, siltstones with minor amount of deep-water shale • **Dolostone** variable sandy to zebra-textured interbedded with polymict debrite and variably calcareous sandstones and silty limestones

Characteristics	Nevada		Nadaleen Trend-ATAC Resources Ltd. Yukon	Venus Zone, Yukon
Age of host rocks	Paleozoic, dominantly Ordovician to early Devonian	Silurian-Devonian	Neoproterozoic-Ediacaran (Conrad, Osiris, Sunrise) and Silurian to Devonian (Anubis)	Neoproterozoic-Ediacaran
Intrusive Rocks	• Jurassic to Cretaceous I-S – type granitoids • Intermediate to mafic composition dike swarms related to subduction		• Cretaceous plutonism, northeast of the Tintina Fault • Late Cretaceous Tombstone Suite • Granitic Rackla Pluton 62.3± 0.7 Ma	• Cretaceous plutonism, northeast of the Tintina Fault • Late Cretaceous Tombstone Suite • Granitic Rackla Pluton 62.3± 0.7 Ma
Structural control	• High-angle N-NNW and NE striking faults • Anticlinal folding in autochthonous carbonates • Collapse breccia bodies		**Regional-Scale:** • Dawson Thrust Fault • Kathleen Lakes Fault **Property-Scale:** • Nadaleen Fault • Large-scale, steeply SW plunging antiforms separated by an E-W trending dextral strike-slip fault (Osiris) • Conrad strata lies in the core of north-northeast trending, doubly plunging antiform	**Regional-Scale:** • Dawson Thrust Fault • Kathleen Lakes Fault **Property-Scale:** • NE-trending brittle faults • Polyphase deformation, mineralization in F_2 hinge zones • E-W striking thrust fault
Alteration				
Silicification	Jasperoids, variably mineralized, quartz druses lined vugs formed as a result of decarbonatization or in collapsed breccias.		Silicification is present but no significant jasperoids have been reported	Silicification is dominant • Extensive, 15-20 m silicified outcrops, • Carbonate matrix completely replaced by quartz in high-grade rocks

Characteristics	Nevada	Nadaleen Trend-ATAC Resources Ltd. Yukon	Venus Zone, Yukon
Decarbonatization	Collapsed breccia bodies locally hosting high-grade gold mineralization	Decarbonatization is primary manifested by stylolites, lesser solution collapse breccias	Dissolution breccias in outcrop-scale, decarbonatization is primary manifested by stylolites, decalcification is evident in thin section
Argillic alteration	Presence of minimal kaolinite±dickite+illite in pure carbonate rocks, and distal sericite	Clay alteration is present nearby in a few igneous rocks, but poorly understood	Not present, sericite alteration is present in high-grade drill-sections, but poorly understood
Ore mineralogy	Arsenian pyrite, marcasite, arsenopyrite	Arsenian pyrite as secondary growth on pre-existing pyrite, primary arsenian pyrite	Arsenian pyrite as secondary growth on pre-existing pyrite, native gold
Pre-ore stage minerals	Calcite, quartz, sericite, pyrite, pyrrhotite, chalcopyrite, sphalerite, arsenopyrite, galena,	Calcite, dolomite, sphalerite, pyrite	Calcite, dolomite, quartz, pyrite, marcasite, arsenopyrite, galena
Late-ore to post-ore stage minerals	Orpiment, realgar, fluorite, galkhaite, stibnite,	Realgar, orpiment, fluorite, stibnite, calcite	Orpiment, realgar, cinnabar, native arsenic, Pb-sulphosalts, quartz, calcite
Pathfinder elements	As, Hg, Sb, Tl± Ba	As, Hg, Tl, ± Sb	Dominantly As, Hg ±Tl, Sb

DISCUSSION

Gold distribution and deportment

Previous studies have established that invisible gold is spatially associated with local arsenic enrichment in pyrite grains and concluded that Au is probably incorporated into metastable solid solution in arsenian pyrite via As-rich growth surfaces (Fleet and Mumin, 1997). Secondary ion mass spectrometry (SIMS) also identified Au associated with As- and Sb-bearing rims of auriferous pyrite from the Post deposit (Bakken et al., 1991). Furthermore, sporadic amounts of invisible gold have also been observed in pyrite, arsenopyrite, and marcasite by electron microprobe analysis in samples taken from various Carlin deposits in Nevada (Fleet and Mumin, 1997). The study of invisible gold in sulphides and arsenian sulphides is beyond the scope of this paper; and the identification of invisible gold has not been attempted during this research. However, based on previous studies and on the presence of arsenian pyrite, it is concluded that invisible Au is likely to occur in ore-stage arsenian pyrite, arsenopyrite, (and marcasite) in the Venus Zone.

Two generations of native gold in close association with: i) arsenian pyrite and stylolitic textures; and ii) scorodite have been observed in SEM-EDX analyzed samples. These two generations of native gold are suggested to represent ore- and post-ore stage of Carlin-type mineralization, respectively (Figure 3.36).

Native gold occurs in remnants of algal mats within stylolites (Figure 3.25b). In the Venus Zone, syn-sedimentary pyrites are the primary sites of nucleation for

auriferous hypogene fluids from which gold, arsenian pyrite, and arsenopyrite precipitated. Algal mats commonly contain syn-sedimentary pyrite and are the dominant constituents of stylolites (Figure 3.44). Stylolites form as a result of diagenetic processes that favour algal mat-bearing horizons within the carbonate host rocks. Therefore, stylolitization of algal mats provide an enhanced depositional site for hypogene Au-bearing fluids. In addition, native gold has also been identified nucleating on the rims of arsenian pyrite. The close association of native free gold with arsenian pyrite suggests that free gold likely precipitated from the same hypogene fluids as arsenian pyrite (Figure 3.25a). Therefore, native gold associated with stylolites and arsenian pyrite is proposed to represent ore-stage Carlin-style mineralization.

Native gold in scorodite is suggested to represent the residuum or the reprecipitated aggregate that formed from the replacement of gold-bearing arsenian pyrite and arsenopyrite by scorodite. This mode of gold occurrence is interpreted as post-ore stage Carlin-style mineralization as it represents a localized redistribution of ore-stage gold (Figure 3.28).

In conclusion, based on previous literature and SEM-EDX analysis, arsenian pyrite, arsenopyrite, and marcasite are all potential Au-bearing sulphides in the Venus Zone. Native gold associated with arsenian pyrite and stylolitic texture is concluded to represent ore-stage Carlin-style gold mineralization with post-ore stage gold redistribution during scoroditization.

Gold-bearing host lithologies

The major gold hosting lithology recognized to date in the Venus Zone is silicified dolostone. The protolith of silicified dolostones is inferred as variably silty to sandy, permeable carbonates with syn-sedimentary pyrite, which provides a Fe-source for Au-bearing fluids to react with. Silicification is interpreted as a pre-ore stage alteration-type, which strongly affects the localization of gold by creating a barrier along sedimentary horizons and influencing permeability and focused fluid flow of ore-forming fluids. The spatial relationship between gold mineralization and silicification is evident in Figure AI.3, where silicification is often observed immediately peripheral to gold mineralization. In addition most silicified dolostones show scorodite mineralization, which may be a useful field indicator of gold-bearing lithologies (Figure 3.45a-b).

Structural control of gold mineralization

The Venus Zone is a structurally complex, polyphase-deformed area. NE trending, brittle faults are the primary fluid conduits for gold mineralizing fluids. Silicification and anomalous gold, arsenic, and mercury rock-chip samples are all concentrated along NE trending fault zones (Figure AI.3-5). In addition, elevated Au, As, and Hg also occur along F_2 fold hinges because hinge zones provided a structural fluid trap for mineralizing fluids. Figure 3.46 demonstrates the concentration of gold and major pathfinder elements along these F_2 fold hinges. The timing of mineralizing fluids is also evident in Figure 3.46. Gold bearing fluids in the Venus Zone seem to occur after F_2 folding, but before the last phase of deformation (F_3).

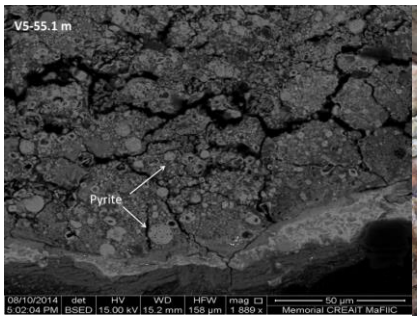

Figure 3.44. Algal mats with syn-sedimentary, framboidal pyrite.

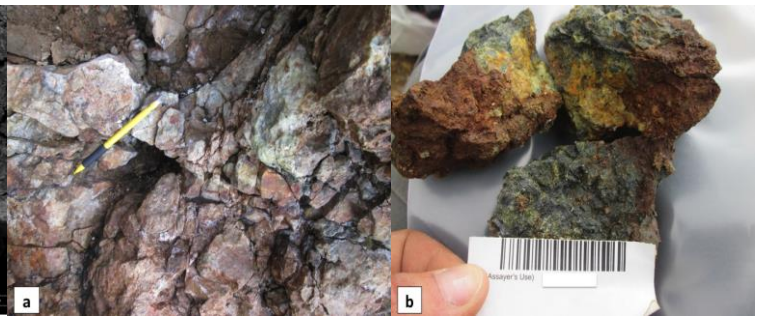

Figure 3.45. A., Silicified dolostone with scorodite mineralization. B., Sample taken from silicified, scorodite mineralized outcrop (A) with 191.8 g/t Au.

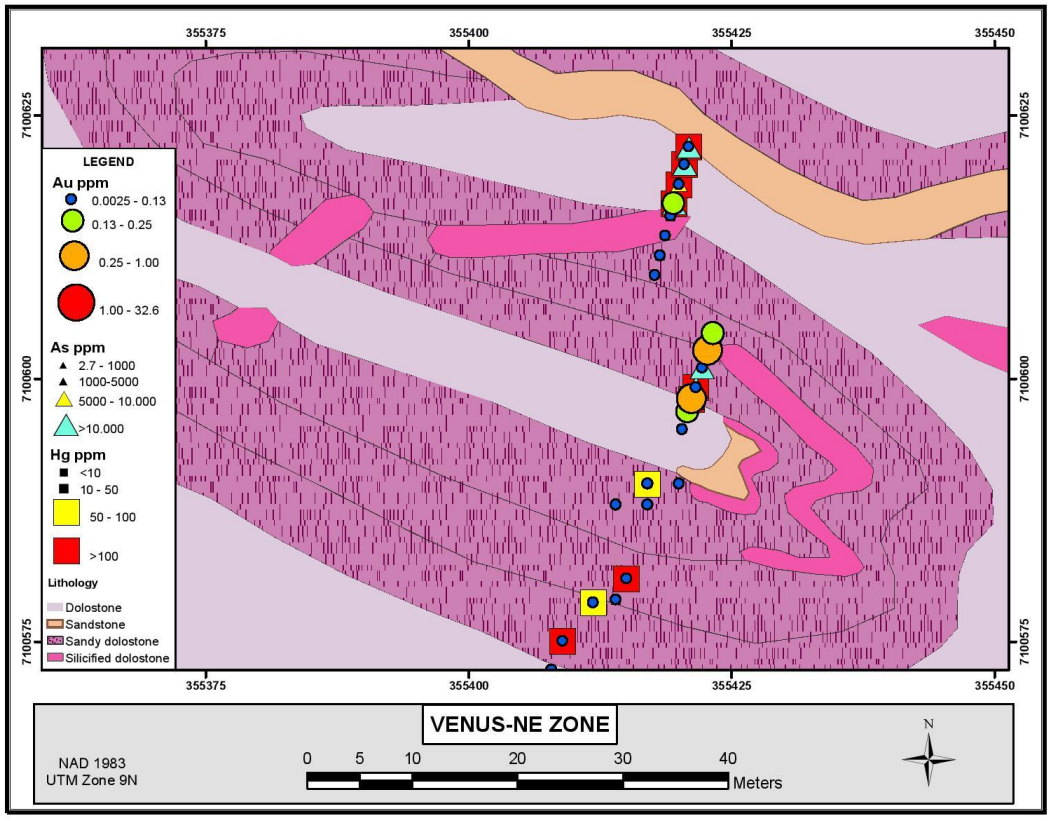

Figure 3.46. Antiform, synform in the NE Venus Zone showing the concentration of elevated Au, As, and Hg in F_2 fold hinges.

Proposed genetic model for the Venus Zone

The common genetic models and their inconsistencies for Carlin-type gold deposits have been discussed above in *Genetic Models, Chapter 1*. A general sulphur fugacity trend is implied by the ore mineralogy, which may explain the paragenetic sequence of the Venus Zone. For the interpretation of this trend, a $fS_{2\,(g)}$-$fO_{2\,(g)}$ diagram has been used from Simon et al. (1991) (Figure 3.47). This diagram indicates sulphur fugacity (fS_2) on the x-axis and oxygen fugacity (fO_2) on the y-axis. The slope in fO_2 is schematic and the interpretations are limited to fS_2. The progression of ore and post-ore stage is represented by the arrows on the diagram.

The pre-ore and ore-stage paragenetic sequence is obviously within the pyrite field. The pyrite field starts approximately at -16 log $fS_{2\,(g)}$ and progresses towards -19 log $fS_{2\,(g)}$. The interpreted ore-stage implies decreasing sulphur fugacity. The ore-stage field is suggested to end at approximately -19.2 log $fS_{2\,(g)}$, at the boundary between the pyrite and stibnite field, because stibnite or pyrrhotite has not been yet observed in the paragenetic sequence. Ore-stage minerals on the $fS_{2\,(g)}$-$fO_{2\,(g)}$ diagram include pyrite, then arsenopyrite, which correlates with the observed ore-stage mineralogy in paragenetic sequence.

The realgar-orpiment field represents post-ore stage. The increase in sulphur fugacity from approximately -19.2 log $fS_{2\,(g)}$ to -7.5 log $fS_{2\,(g)}$ would simulate progression of fluids that precipitated post-ore stage minerals. This observed progression from ore-stage to post-ore stage is also evident in the paragenesis.

Direct replacement of ore-stage arsenopyrite by realgar and in some cases arsenian pyrite has been observed. In addition native arsenic, which is suggested to form post-ore stage, could be produced on this path by the breakdown of arsenopyrite.

The increase in sulphur fugacity may be explained by the mixing of the original deeply sourced magmatic or metamorphic fluids with meteoric water or with matured, basinal fluids enriched in H_2S. Mixing results in the addition of more H_2S to the system, which changes the composition of fluids and thus may increase sulphur fugacity. Based on the above mentioned interpretations and mineralogical observations, mixing of a deeply sourced fluids with meteoric water or with matured basinal brines may explain the paragenetic sequence and therefore suggests that ore formation on the Venus Zone is the result of mixing two differently sourced fluids.

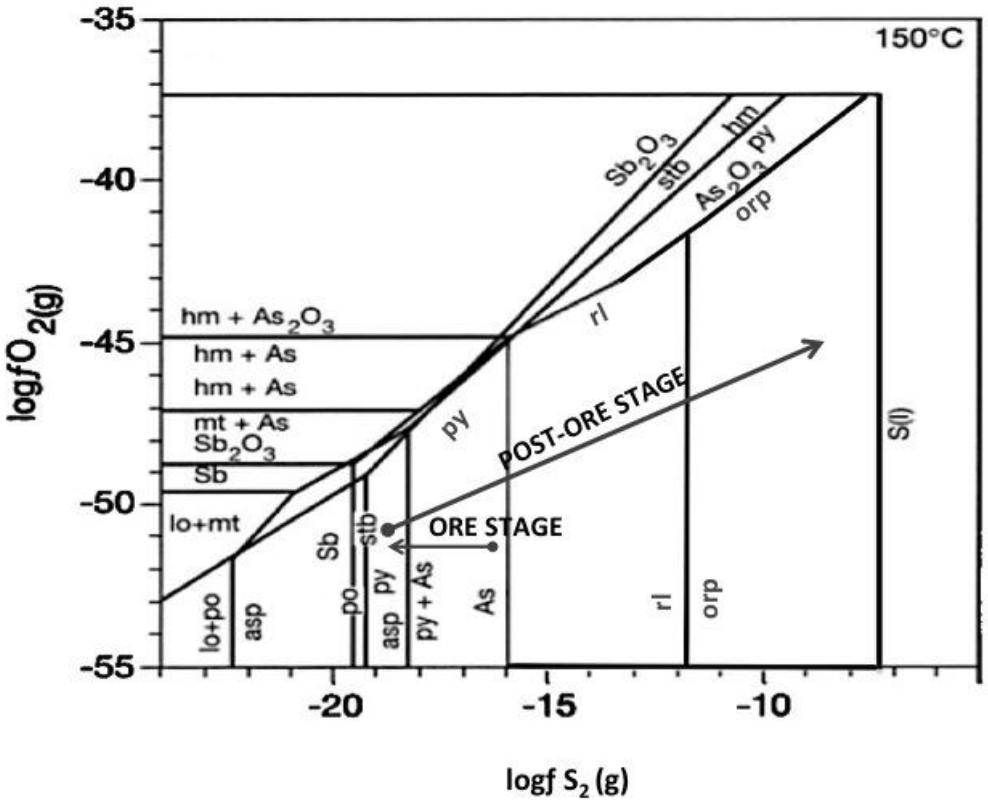

Figure 3.47. $fS_{2\,(g)}$-$fO_{2\,(g)}$ diagram showing the ore-stage and post-ore stage mineralogical pathways of the Venus Zone. *(Modified after Simon et al., 1999)*

Abbreviations

As-arsenic, Asp-arsenopyrite, Liq-liquid, Lo-loellingite, Orp-orpiment, Po-pyrrhotite, Py-pyrite, Rl-realgar, S-sulphur, Sb-antimony, Stb-stibnite, Hm-hematite Mt-magnetite

CHAPTER 4

SUMMARY AND CONCLUSIONS

EVIDENCE FOR CARLIN-STYLE GOLD MINERALIZATION

The main focus of this study is to determine whether the mineralogical and structural observations in the Venus Zone resemble characteristic Carlin-style gold mineralization in Nevada. The Venus Zone is located in central east Yukon Territory, Canada. This area of the Yukon shares similar geological history to the Great Basin, Nevada including depositional setting and tectonic evolution.

Gold mineralization in the Venus Zone is identified in carbonates within the Algae Formation of the Selwyn Basin. The Algae Formation is part of the Neoproterozoic Hyland Group, which is interpreted to form on the continental margin of the Selwyn Basin from passive margin sedimentation. Silicified dolostones are the major gold-hosting lithology recognized to date, because their protolith is interpreted as a favorable receptor site for auriferous fluids. Elevated gold and major pathfinder elements occur along both northeast trending brittle faults and second generation (F_2) fold hinges. The occurrence of gold within characteristic silicified carbonate horizons and along structural zones shows that gold mineralization in the Venus Zone is both lithologically and structurally controlled.

Pre-ore stage silicification is the most prominent and useful alteration-type for locating gold mineralized lithologies. Decarbonatization is a recognized alteration-type; however, further research is required to truly understand its prominence and relation to gold mineralization. The characteristic pathfinder elements of Carlin-

style gold mineralization are present in the Venus Zone. Elevated arsenic and mercury are a useful spatial indicators for proximal gold mineralization; however, they do not necessary directly reflect the presence of gold.

Arsenian pyrite and submicroscopic native gold are both present in the Venus lithologies. Mineralization consists of pyrite, marcasite, arsenian pyrite, arsenopyrite and subsequent native gold deposition; realgar, orpiment, and scorodite are commonly observed as post-ore minerals.

In conclusion, the regional tectonic setting and the local features at the Venus Zone are similar to sediment hosted gold deposits in the Carlin Trend of Nevada in that gold is hosted in silty, variably dolomitic carbonates and intimately associated with arsenian pyrite. Based on detailed surface mapping, core logging, and laboratory work on both host rocks and mineralized lithologies, the author suggests that the Venus Zone is a Carlin-type gold deposit.

FUTURE EXPLORATION CRITERIA

Field observations

Silicification is the most prominent and useful alteration-type; therefore, future exploration plans are recommended to focus on the extensive rock-chip sampling of these zones, and particularly domains immediately peripheral to these silicified areas. In addition, sampling dissolution breccias may also provide further useful indication of gold mineralized areas. Realgar and orpiment are typically more erratic at the deposit scale, and do not necessarily indicate gold mineralization.

However, scorodite mineralization is generally evident in Au-bearing lithologies, and it is a more effective signature of gold mineralization. Therefore, scorodite mineralized outcrops and areas should be trenched and extensively sampled instead of realgar and orpiment showings.

Structural observations

Northeast trending faults are primary fluid conduits and as a result of that they are often mineralized. A closely spaced rock-chip sampling program is advised to locate areas where mineralizing fluids along these faults intersected favorable host lithologies. Furthermore, detailed mapping of F_2 hinge zones is recommended to test gold mineralization within these zones.

The northeast Venus Zone holds a great potential for gold mineralization. Detailed mapping would help to identify the extent of antiform-synform pair. A diamond drill hole perpendicular to the F_2 fold axis of the antiform-synform pair may prove to be successful in future exploration. Previous drill holes D2-13-14 and D2-13-17 that drilled towards the northeast zone were placed too far from the antiform-synform pair to intersect the hinge zone.

Prospecting the thrust contact between the dolostones and the mafic volcanic breccia on the northeast side of the property may help to discover newly mineralized or silicified areas in this sheared contact.

Geophysical methods

Gold-hosting lithologies contain a reasonable amount of syn-sedimentary pyrite (2-5 %). An electromagnetic conductivity (EM) survey may prove to be effective in delineating these pyritic zones. The high-grade zone of drill hole D2-12-05 with its silicified, pyritiferous lithology would appear to have potential as a strong EM responder.

Drill-core observations

In the drill core, sampling of stylolites and dissolution seams on a shorter interval from the rest of the drill core is strongly recommended. This is essential because native gold in stylolites is very localized and sampling on a shorter interval would increase the probability of detecting elevated gold mineralization. Sampling of fault zones should proceed beyond the fault gouge into unaltered rock. Some of the mineralized intervals in previous drill holes immediately occurred after the fault gouge. In addition, the consistent testing of silicification during core-logging and sampling silicified zones on a shorter interval is advised. Scorodite mineralization holds a great a promise, as an indicator in drill-core, thus the consistent sampling of scorodite-altered zones may be beneficial.

REFERENCES

Anthill Resources Ltd., (2012). 2012 Exploration Highlights of the Einarson Project. October 15, 2012. Retrieved from http://www.anthillresources.com/s/NewsReleases.asp

Arehart, B. G., Ressel, M., Carne, R. C., & Muntean, J. (2013). A Comparison of Carlin-type Deposits in Nevada and Yukon. *Society of Economic Geologist, Inc., Special Publication 17*, p. 389-401.

ATAC Resources Ltd., (2012a). ATAC Resources Ltd. Intersects 42.93 m of 18.44 g/t Au Gold at its Rackla Gold Project-Yukon. August 21, 2012. Retrieved from http;//www.atackresources.com/s/NewsReleases.asp. Web. August 21, 2012.

ATAC Resources Ltd., (2012b). ATAC Resources Ltd. 19.85 g/t Gold over 8.51 Metres as its Newest Carlin-type Gold Discovery located 10 km West of Osiris. Retrieved from http://www.atacresources.com/s/NewsReleases.asp.Web September 2012.

Bakken, B. M., Brigham, R. H., & Fleming, R. H. (1991). The distribution of gold in unoxidized ore from Carlin-type deposits revealed by secondary ion mass spectrometry (SIMS). *GSA Abstr. Prog*. 23, A228.

Barker, S. L., Hickey, K. A., Cline, J. S., Dipple, G. M., Kilburn, M. R., Vaughan, J. R., & Longo, A. A. (2009). Uncloaking invisible gold: use of nanoSIMS to evaluate gold, trace elements, and sulfur isotopes in pyrite from Carlin-type gold deposits. *Economic Geology*, *104*(7), 897-904.

Bennett, V. (2012). Anthill Field Report.

Bouma, A. H., Kuenen, P. H., & Shepard, F. P. (1962). *Sedimentology of some flysch deposits: a graphic approach to facies interpretation* (Vol. 168). Amsterdam: Elsevier.

Cecile, M.P. (2000). Geology of the northeastern Niddery Lake map area, east-central Yukon and adjacent Northwest Territories. Geological Survey of Canada*, Bulletin 553*, 120 p.

Chakungal, J. & Bennett, V. (2011). New bedrock geology of Mount Mervyn map sheet (106C/04) and mineral potential for the South Wernecke mapping project. In: Yukon Exploration and Geology 2010, K.E. MacFarlane, L.H. Weston, and C. Relf (eds.), *Yukon Geological Survey,* p. 55-87

Cline, J. S., & Hoftstra, A. A. (2000). Ore-fluid evolution at the Getchell Carlin-type gold deposit, Nevada, USA. *European Journal of Mineralogy*, *12*(1), 195-212.

Cline, J. S. (2001). Timing of gold and arsenic sulfide mineral deposition at the Getchell Carlin-type gold deposit, north-central Nevada. *Economic Geology*, *96*(1), 75-89.

Cline, J. S., Hofstra, A. H., Muntean, J. L., Tosdal, R. M., & Hickey, K. A. (2005). Carlin-type gold deposits in Nevada: Critical geologic characteristics and viable models. *Economic Geology 100th anniversary volume*, 451-484.

Colpron, M., Nelson, J., & Murphy, D. (2007). Northern Cordillera terranes and their interactions through time. *GSA Today*, v. 17, no. 4/5, p. 4-10.

Colpron, M. (2012a). Preliminary geological map of the Mount Ferrell area (106C/3), central Yukon. Yukon Geological Survey, Open File 2012-11, 1:50 000.

Colpron, M. (2012b). Preliminary observations on the geology of the Rackla belt, Mount Ferrell map area (NTS 106C/3), central Yukon. In: *Yukon Exploration and Geology* 2011, K.E. MacFarlane, M.G. Nordling, and P. J. Sack (eds.), Yukon Geological Survey, p. 27-43

Colpron, M., Moynihan, D., Israel, S., & Abbott, G., (2013). Geological map of the Rackla belt, east-central Yukon (NTS 106C/1-4, 106D/1). Yukon Geological Survey, Open File 2013-13, 1:50 000 scale, 5 maps and legend.

Emsbo, P., Hofstra, A. H., Lauha, E. A., Griffin, G. L., & Hutchinson, R. W. (2003). Origin of high-grade gold ore, source of ore fluid components, and genesis of the Meikle and neighboring Carlin-type deposits, northern Carlin trend, Nevada. *Economic Geology*, *98*(6), 1069-1105.

Flanders, A. M., Harris, M.J., Kearns, L, and Hart, C.J.R., (2007). Micropetrology and mineral geochemistry of the Tombstone and Deadman plutons, Tombstone Plutonic Suite, central Yukon. *Yukon Exploration and Geology* 2006, D.S. Edmond, L.L. Lewis and L.H. Weston (eds.), Yukon Geological Survey, p.149-156.

Fleet, E., & Mumin, A. H. (1997). Gold-bearing arsenian pyrite and marcasite and arsenopyrite from Carlin Trend gold deposits and laboratory synthesis. *American Mineralogist*, *82*, 182-193.

Gabrielse, H. (1991). Late Paleozoic and Mesozoic terrane interactions in north-central British Columbia. *Canadian Journal of Earth Sciences*, *28*(6), 947-957.

Goldstein, J., Newbury, D., Joy, D., Lyman, C., Echlin, P., Lifshin, E., Sawyer, L. & Michael, J. (2003). Scanning Electron Microscopy and X-Ray Microanalysis, 3rd ed.

Gordey, S. P., & Anderson, R. G. (1993). Evolution of the northern Cordilleran miogeocline, Nahanni map area (1051), Yukon and Northwest territories.

Hoffman, E. L., Clark, J. R., & Yeager, J. R. (1998). Gold analysis–Fire assaying and alternative methods. *Exploration and Mining Geology*, *7*(1), 2.

Hofstra, A. H., Leventhal, J. S., Northrop, H. R., Landis, G. P., Rye, R. O., Birak, D. J., & Dahl, A. R. (1991). Genesis of sediment-hosted disseminated-gold deposits by fluid mixing and sulfidization: Chemical-reaction-path modeling of ore-depositional processes documented in the Jerritt Canyon district, Nevada. *Geology*, *19*(1), 36-40.

Ilchik, R. P., & Barton, M. D. (1997). An amagmatic origin of Carlin-type gold deposits. *Economic Geology*, *92*(3), 269-288.

Kingston, S., Mortensen, J. K., Gabites, J., & Dumala, M. (2010). Ar-Ar geochronology and Pb isotopic constraints on the origin of the Rau gold-rich carbonate replacement deposit, central Yukon.

Kuehn, C. A. (1989). *Studies of disseminated gold deposits near Carlin, Nevada: Evidence for a deep geologic setting of ore formation*. Pennsylvania State Univ., Middletown, PA (USA).

Kuehn, C. A., & Rose, A. W. (1992). Geology and geochemistry of wall-rock alteration at the Carlin gold deposit, Nevada. *Economic Geology*, *87*(7), 1697-1721.

Kuehn, C. A., & Rose, A. W. (1995). Carlin gold deposits, Nevada; origin in a deep zone of mixing between normally pressured and overpressured fluids. *Economic Geology*, *90*(1), 17-36.

Leonardson, R. W., & Rahn, J. E. (1995). Geology of the Betze-Post gold deposits, Eureka county, Nevada. *Geology and ore deposits of the American Cordillera: Geological Society of Nevada, Reno, Nevada*, 61-94.

Lubben, J. D. (2004). Silicification across the Betze-Post Carlin-type Au deposit: Clues to ore fluid properties and sources, northern Carlin trend, Nevada. *Doctoral dissertation, University of Nevada, Las Vegas.*

Mortensen, J. K., Hart, C. J. R., Murphy, D. C., & Heffernan, S. (2000). Temporal evolution of Early and mid-Cretaceous magmatism in the Tintina Gold Belt. *The Tintina Gold Belt: Concepts, Exploration and Discoveries, J. Jambor (ed.), British Columbia and Yukon Chamber of Mines, Special*, *2*, 49-57.

Moynihan, D., (2014). Bedrock Geology of NTS 106/B/04, Eastern Rackla Belt. *Yukon Exploration and Geology* 2013, K.E. MacFarlane, M.G. Nordling, and P.J. Sack (eds.), Yukon Geological Survey, p. 147-167.

Moynihan, D., (2014). Preliminary geological map of NTS 106B/04, central Yukon. Yukon Geological Survey, Open File 2014-1, 1:50 000.

Moynihan, D., (2014). Bedrock Geology of NTS 106B/04, Eastern Rackla Belt. In: Yukon Exploration and Geology 2013, K.E. MacFarlane, M.G. Nordling, and P.J. Sack (eds.), *Yukon Geological Survey*, p. 147-167.

Muntean, J. L., Cline, J. S., Simon, A. C., & Longo, A. A. (2011). Magmatic-hydrothermal origin of Nevada/'s Carlin-type gold deposits. *Nature Geoscience*, *4*(2), 122-127.

Nesse., W.D. (2012). Introduction to mineralogy. Second edition.

Nevada Bureau of Mines and Geology. (2004). The Nevada mineral industry 2003. *Nevada Bureau of Mines and Geology Special Publication MI-2003*, p. 78.

Piburn, G., & Barron, A. R. (2013). An introduction to energy dispersive X-ray spectroscopy. *Physical methods in chemistry and nano science. Connexions/Rice University, Houston*, 90-98.

Radtke, A. S., Rye, R. O., & Dickson, F. W. (1980). Geology and stable isotope studies of the Carlin gold deposit, Nevada. *Economic Geology*, *75*(5), 641-672.

Robert, F., Brommecker, R., Bourne, B. T., Dobak, P. J., McEwan, C. J., Rowe, R. R., & Zhou, X. (2007). Models and exploration methods for major gold deposit types. In B. Milkereit (Ed.), *proceedings of Exploration* (Vol. 7, pp. 691-711).

Seedorff, E. (1991). Magmatism, extension, and ore deposits of Eocene to Holocene age in the Great Basin—Mutual effects and preliminary proposed genetic relationships. *Geology and ore deposits of the Great Basin*, *1*, 133-178.

Schutz, L., & Williams, C. (1995). Gold mineralization in the Blue Star/Genesis mine, Eureka County, Nevada. *Structural geology of the Carlin trend: Geological Society of Nevada Field Trip Guidebook*, 167-175.

Shearer, J.T. (1976). Geological and geochemical report on the Tom and Mom claims, North Stewart River Area, Mayo mining division. Assessment report # 090080.

Simon, G., Kesler, S. E., & Chryssoulis, S. (1999). Geochemistry and textures of gold-bearing arsenian pyrite, Twin Creeks, Nevada; implications for deposition of gold in Carlin-type deposits. *Economic Geology*, *94*(3), 405-421.

Teal, L., & Jackson, M. (2002). Geologic overview of the Carlin trend gold deposits. *Gold deposits of the Carlin trend: Nevada Bureau of Mines and Geology Bulletin*, *111*, 204.

Thiessen, E.J., Gleeson, S.A., Dufrane, S.A., Carne, R.C., & Dumala, M. (2011). Upper age constraint and paragenesis of the Tiger zone, Rau property, central Yukon. *Yukon Exploration and Geology 2011*, K.E. MacFarlane and P.J. Sack (eds.), Yukon Geological Survey, p. 151-164.

Thoreson, R. F. (1993). Geology of the Post deposit, Eureka County, Nevada. *Gold Deposits of the Carlin Trend, Nevada. Soc. Econ. Geol., Field Trip Guidebook*, 50-64.

Tucker, M. J., Hart, J. R., & Carne, R. (2013). Geology, alteration, and mineralization of the Carlin-type Conrad zone, Yukon. *Yukon Exploration and Geology, 2012,* K.E. MacFarlane, M.G. Nordling, and P.J. Sack (eds.), Yukon Geological Survey, p. 163-178.

Wolf, S. F., Bowers, D. L., & Cunnane, J. C. (2005). Analysis of high burnup spent nuclear fuel by ICP-MS. *Journal of Radioanalytical and Nuclear Chemistry*, *263*(3), 581-586.

APPENDIX I

MAPS

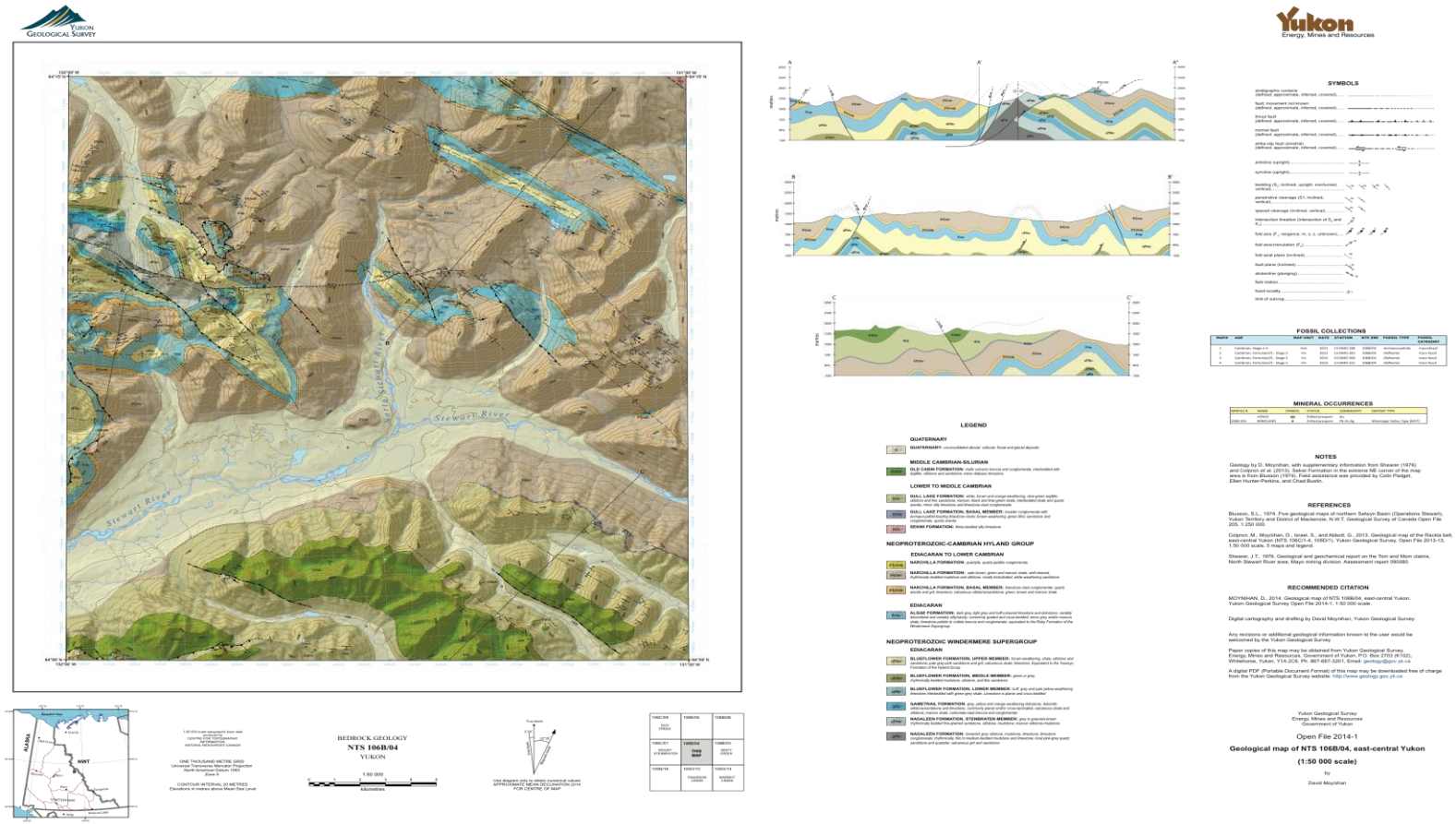

Figure AI.1. Bedrock geology map of the eastern Rackla Belt. The Venus Zone is in the southwest corner of the map *(After Moynihan, 2014*).

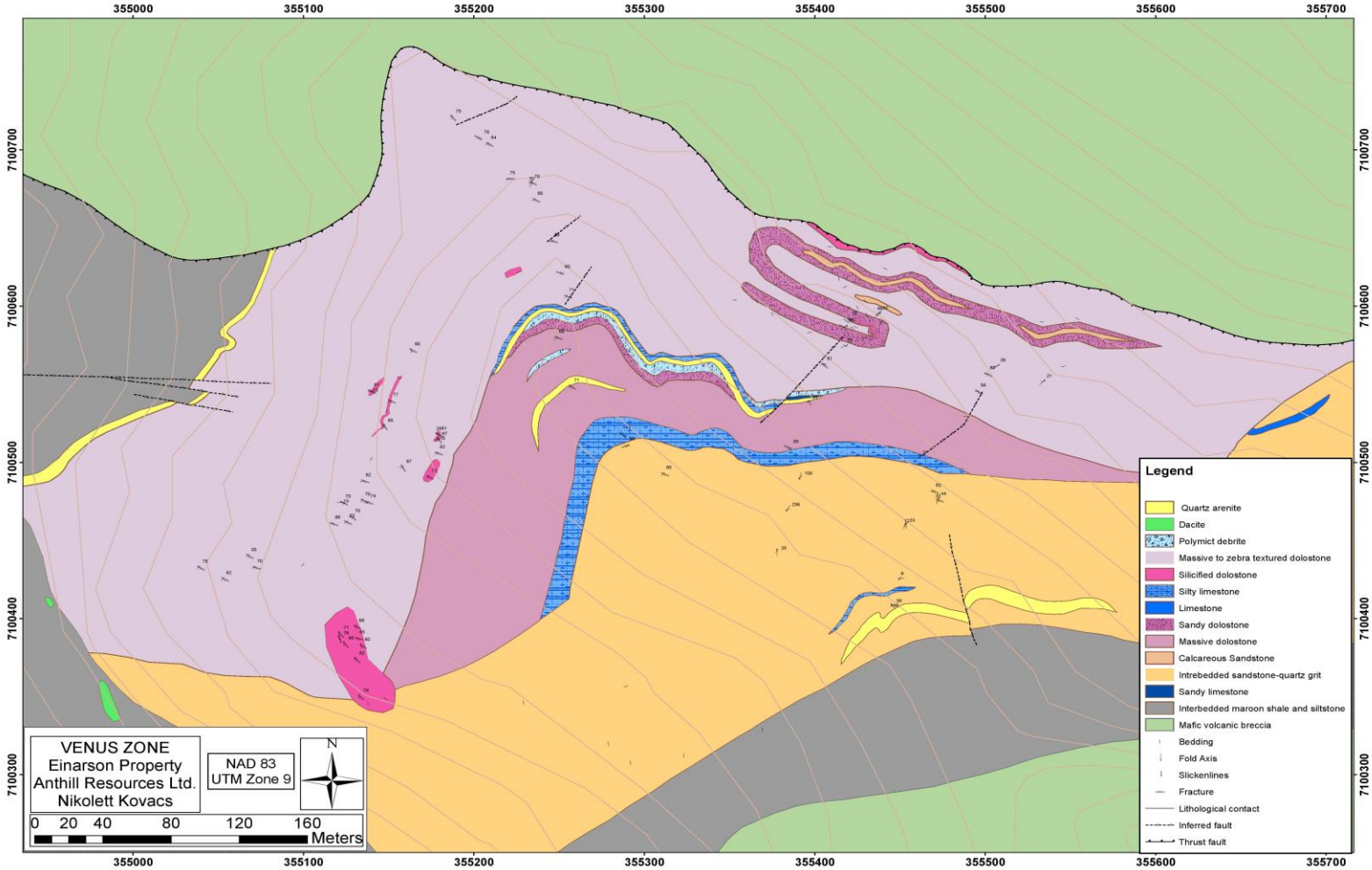

Figure AI.2. Bedrock geology map of the Venus Zone with structural measurements.

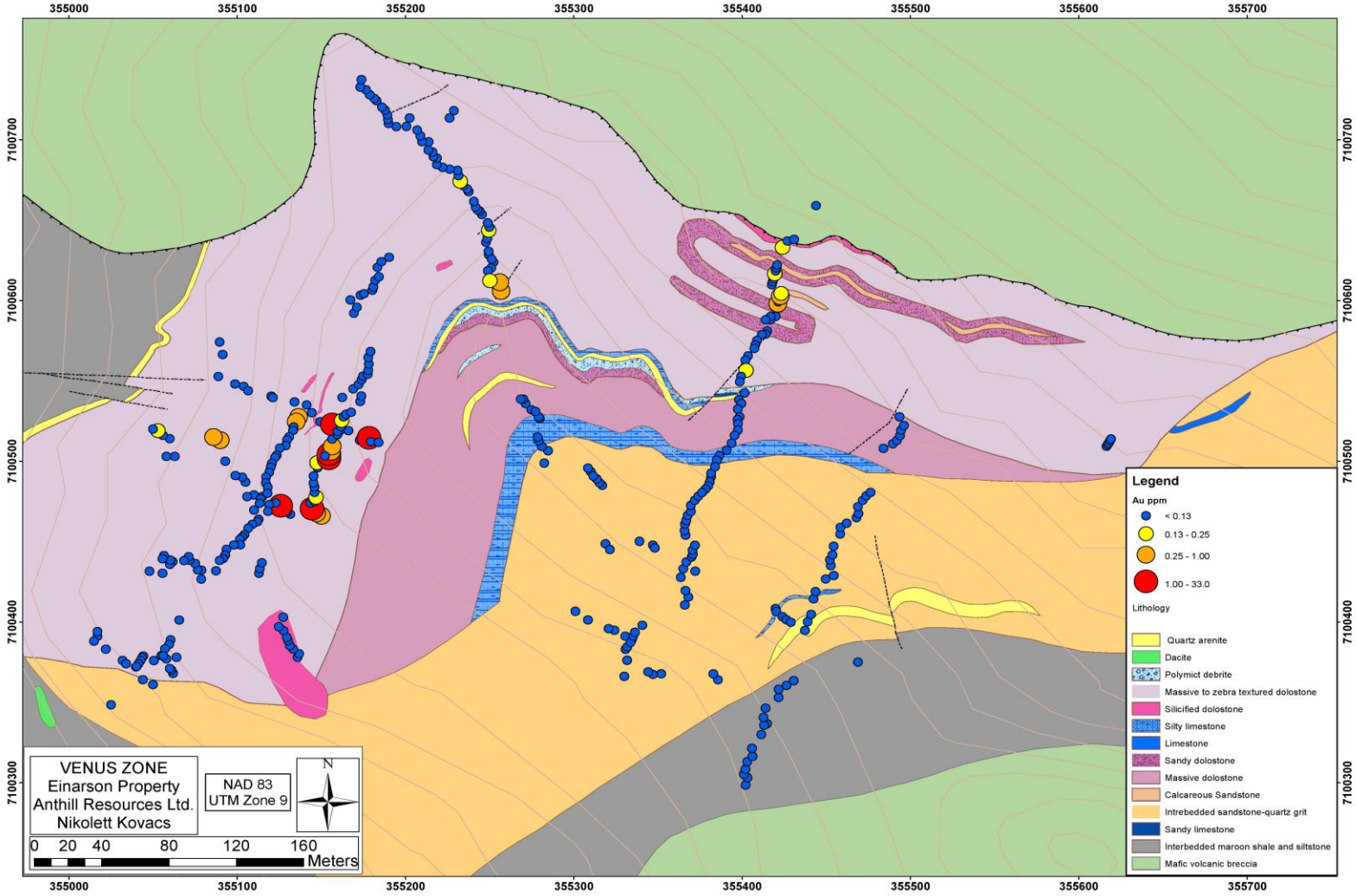

Figure AI.3. Gold rock-chip map, Venus Zone.

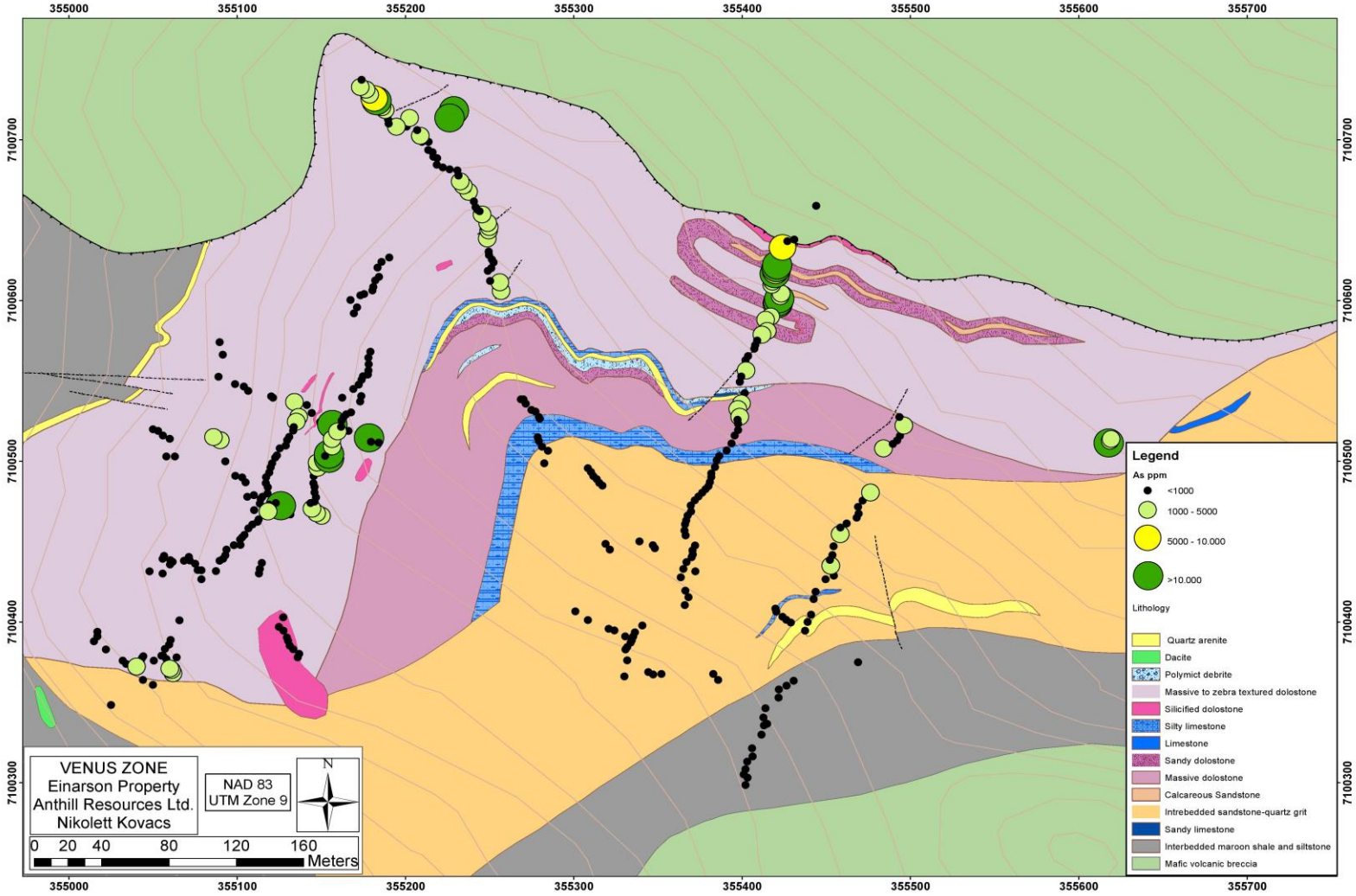

Figure AI.4. Arsenic rock-chip map, Venus Zone.

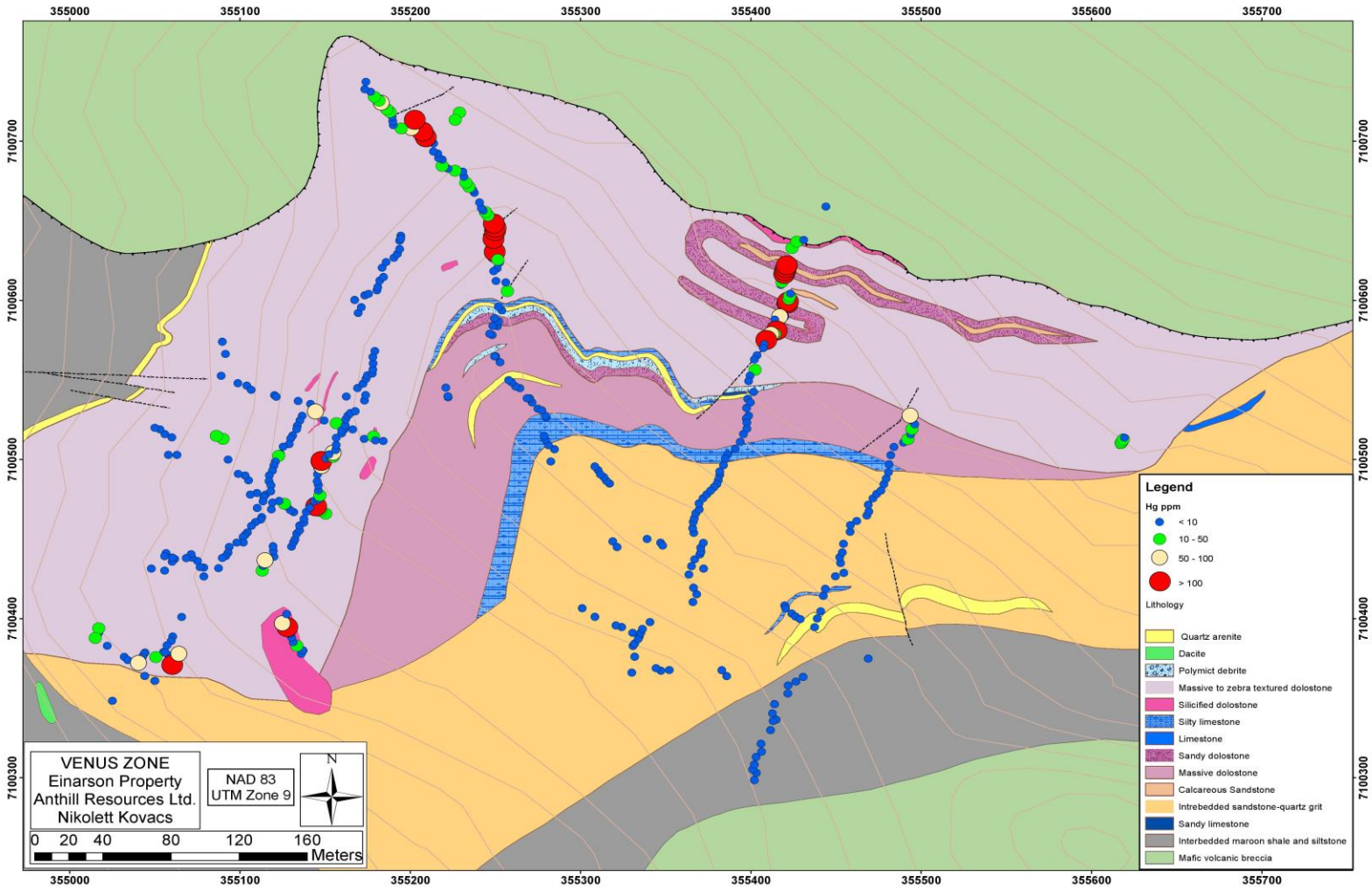

Figure AI.5. Mercury rock-chip map, Venus Zone.

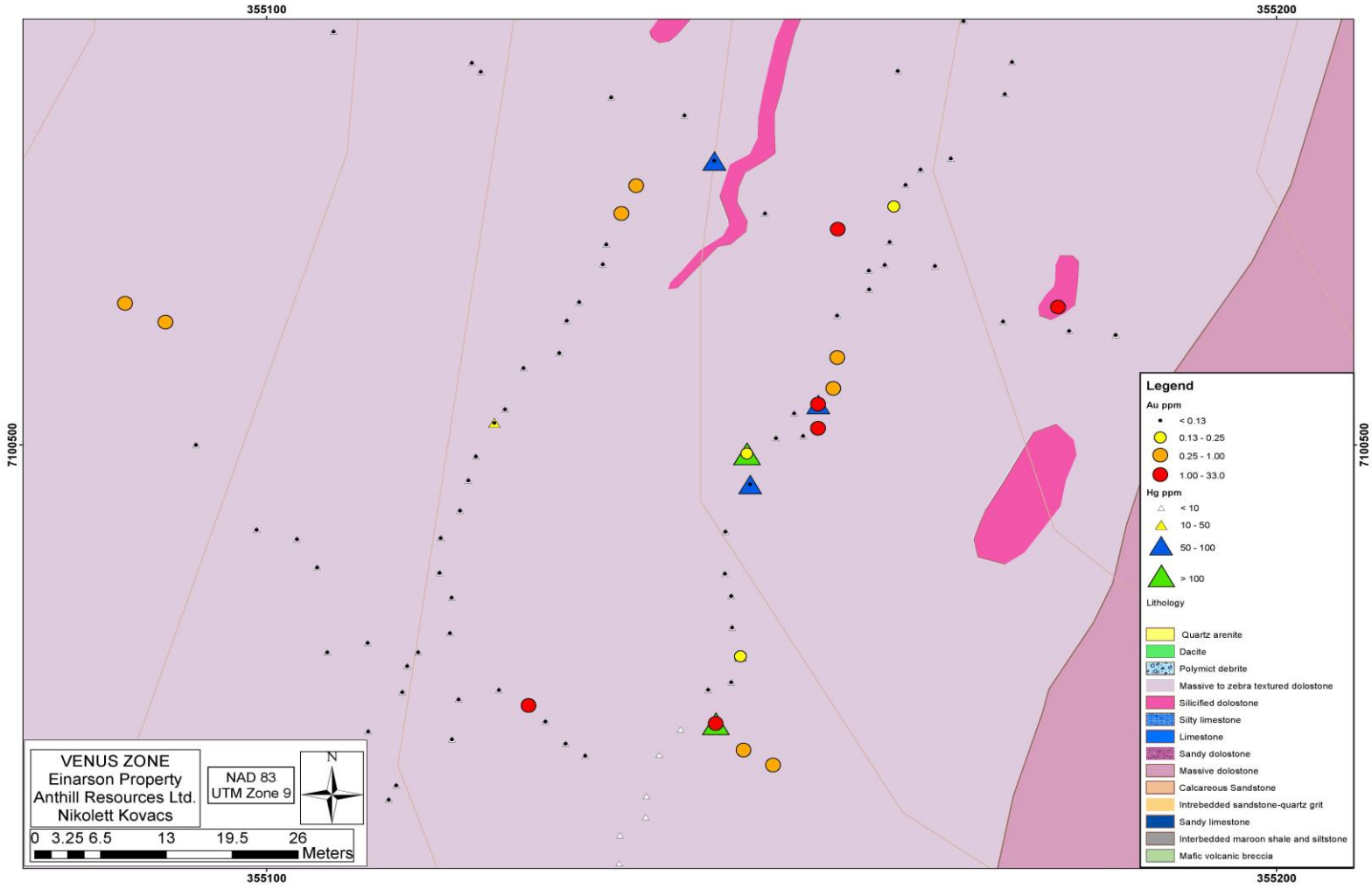

Figure AI.6. Gold-mercury rock-chip map showing the correlation between elevated Au and Hg, central Venus Zone.

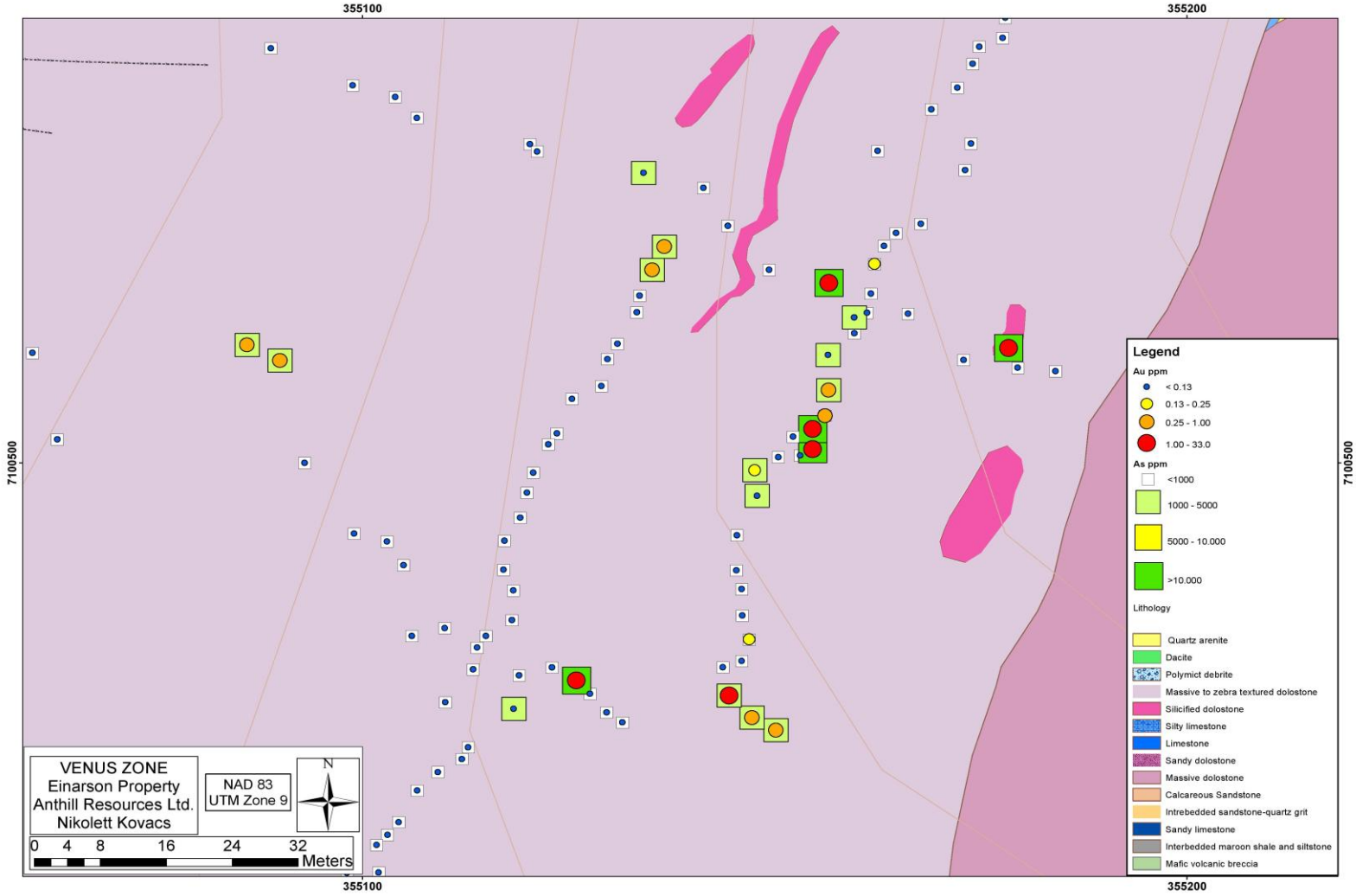

Figure AI.7. Gold-arsenic rock-chip map showing the correlation between elevated Au and As, central Venus Zone.

APPENDIX II

GEOCHEMICAL BACKGROUND SIGNATURES

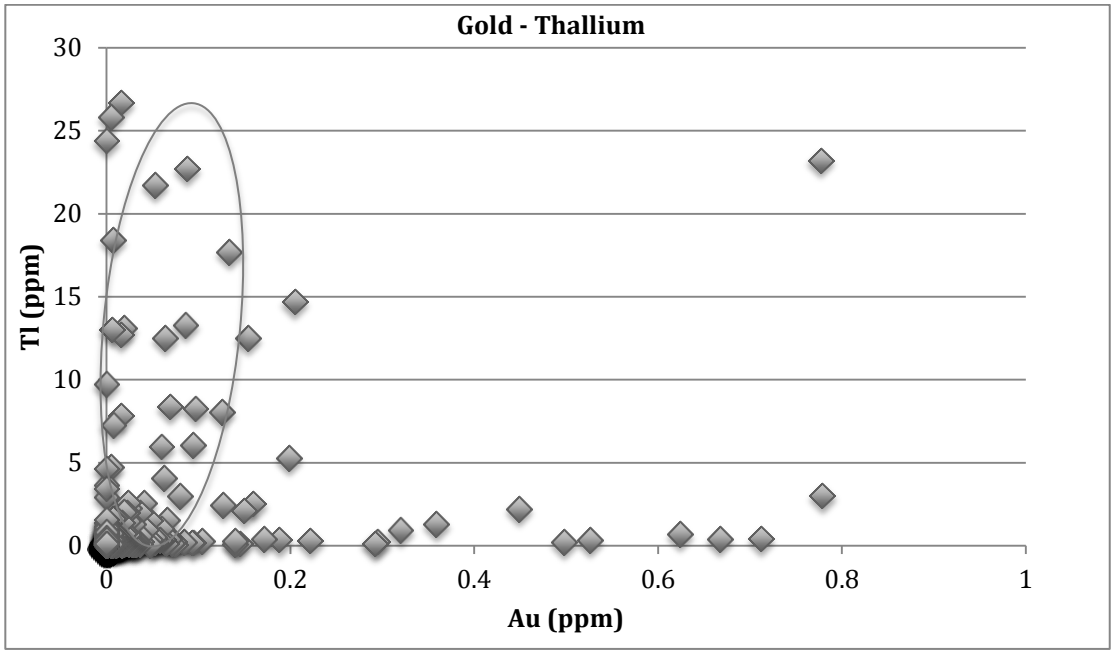

Figure AII.1. Gold-thallium plot indicative of elevated Tl in non-gold mineralized rocks.

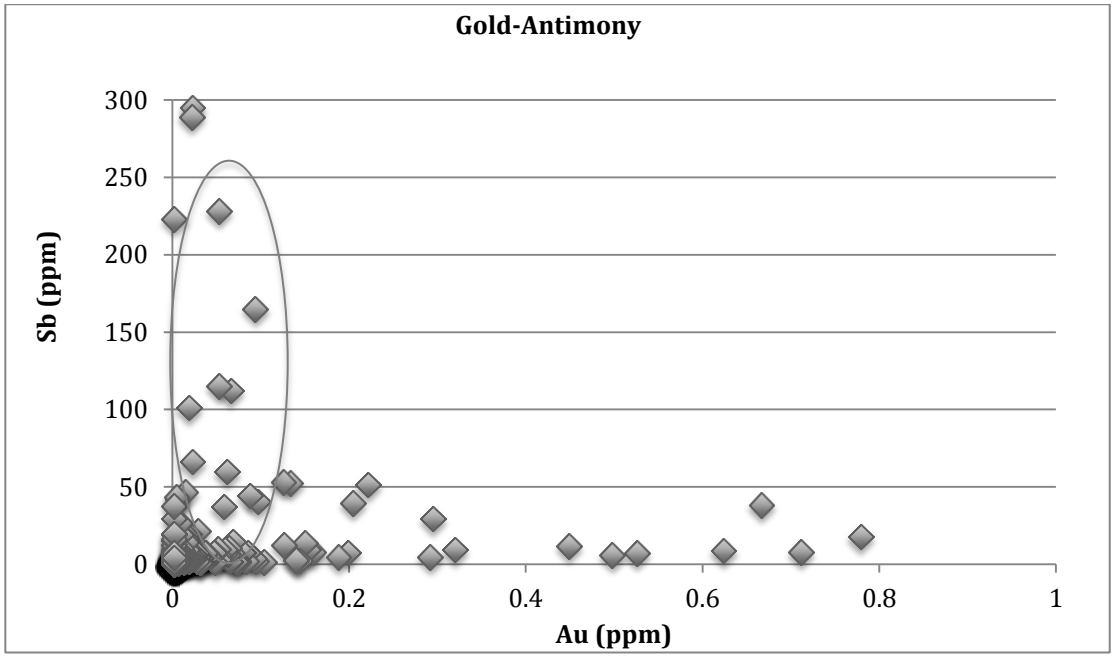

Figure AII.2. Gold-antimony plot indicative of elevated Sb in non-gold mineralized rocks.

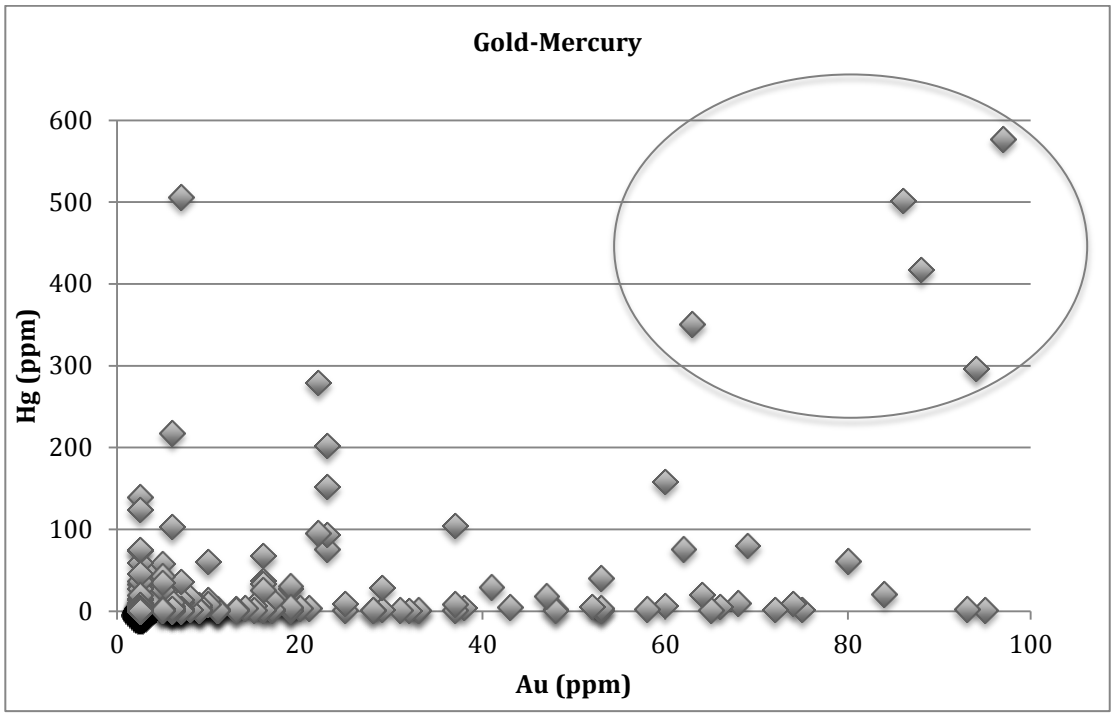

Figure AII. 3. Gold-mercury plot showing elevated Au with Hg. Elevated Au-Hg values may represent proximity to gold mineralization.

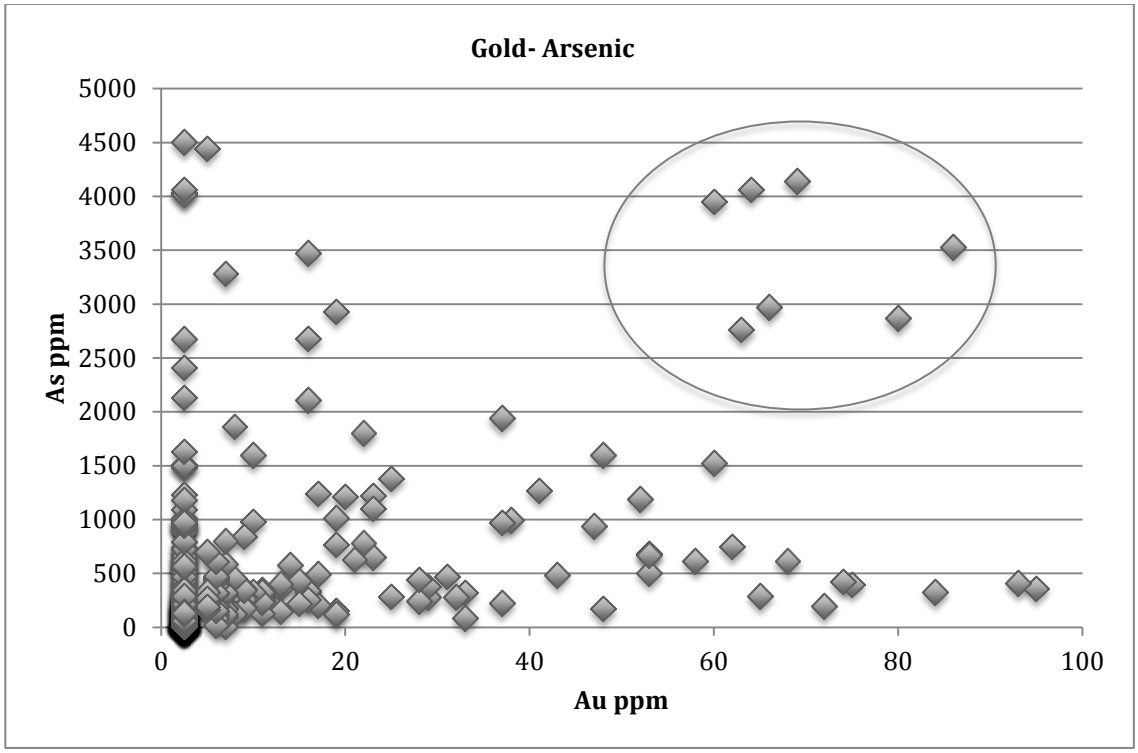

Figure AII.4. Gold-arsenic plot showing elevated Au with As. Elevated Au-As values may represent proximity to gold mineralization.

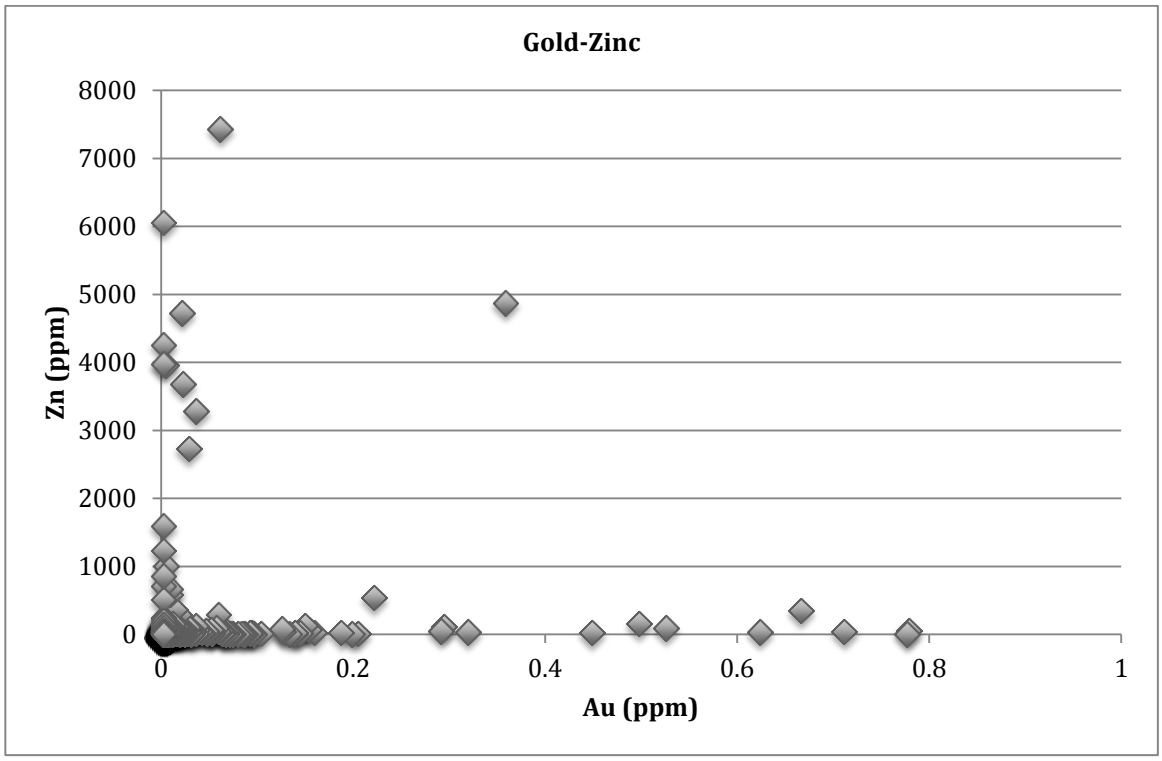

Figure AII.5. Gold-zinc plot.

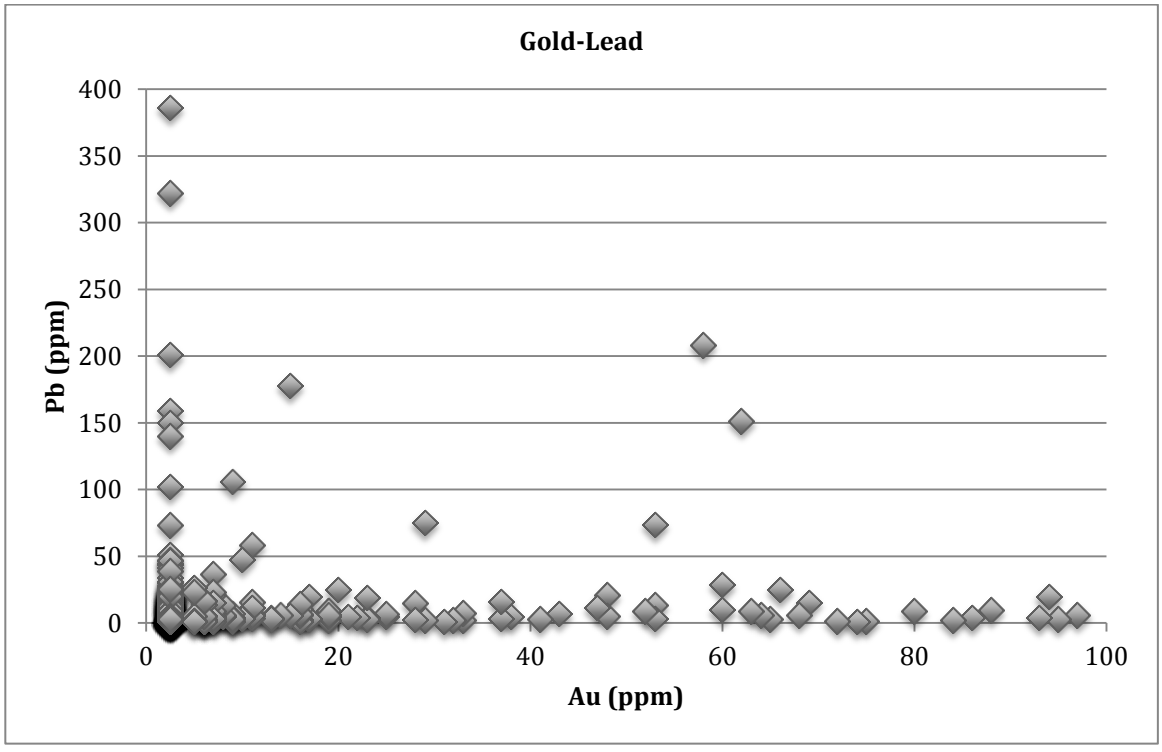

Figure AII.6. Gold-lead plot.

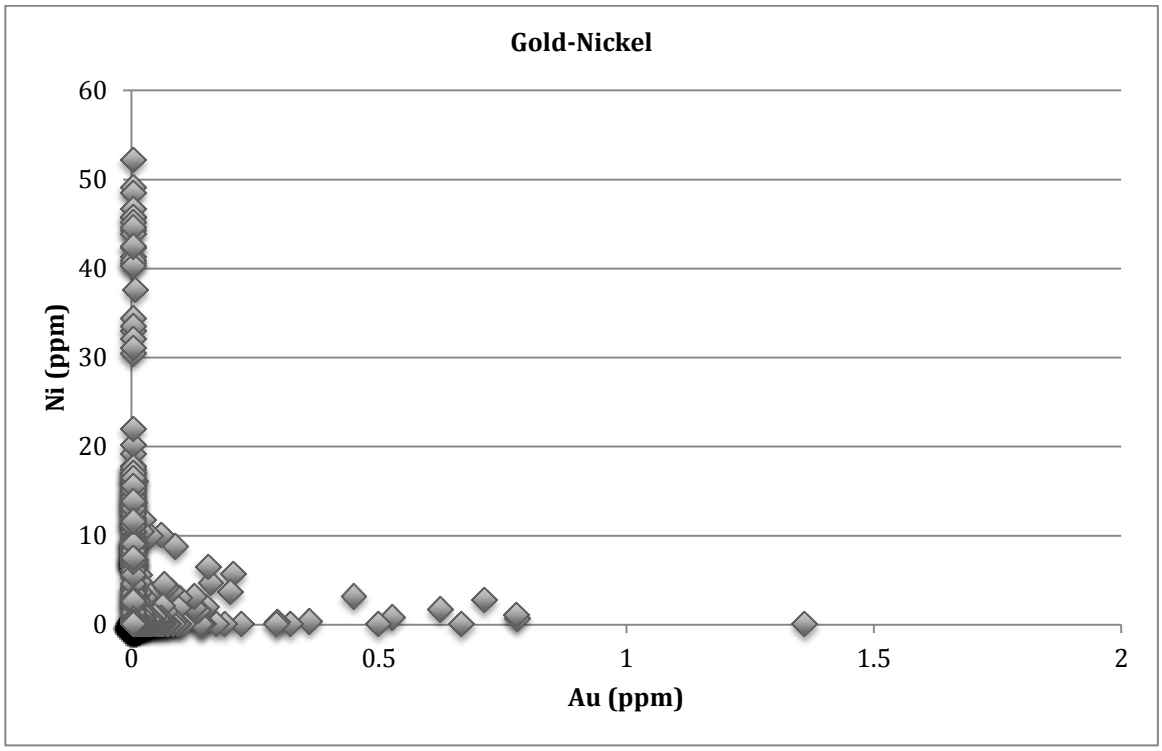

Figure AII.7. Gold-nickel plot.

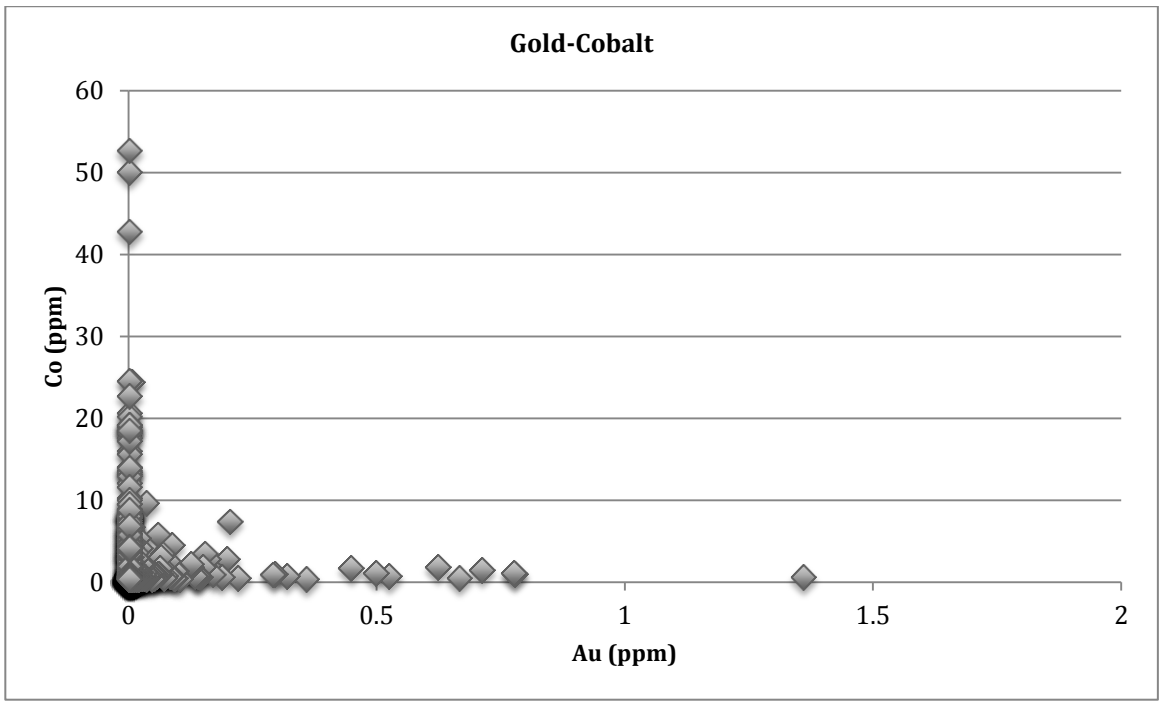

Figure AII.8. Gold-cobalt plot.

GOLD MINERALIZED SAMPLES

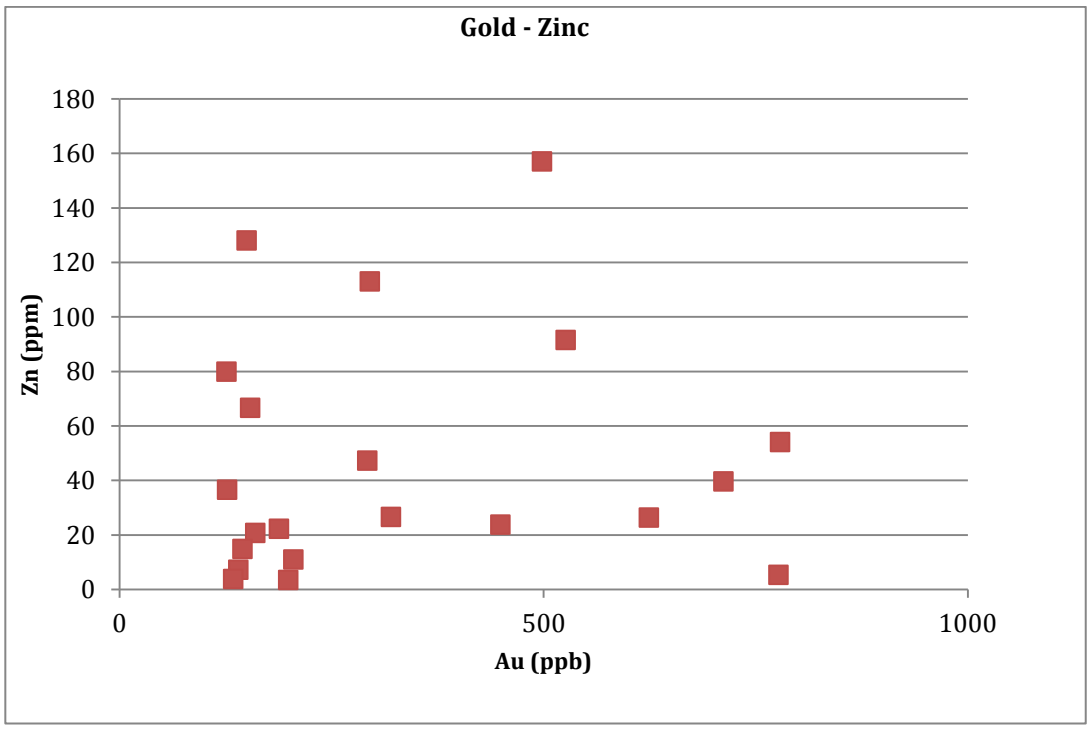

Figure AII.9. Gold-zinc plot showing the scattered nature of zinc. Zinc is indicative of pelitic lithologies.

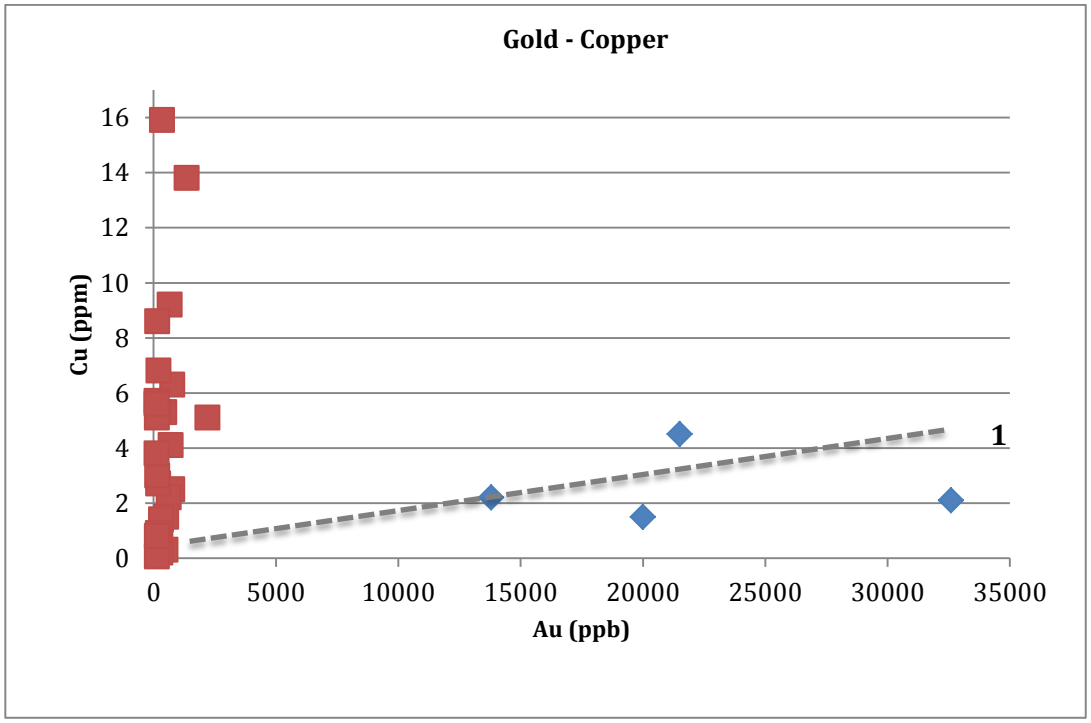

Figure AII.10. Gold-copper plot. Undetermined correlation.

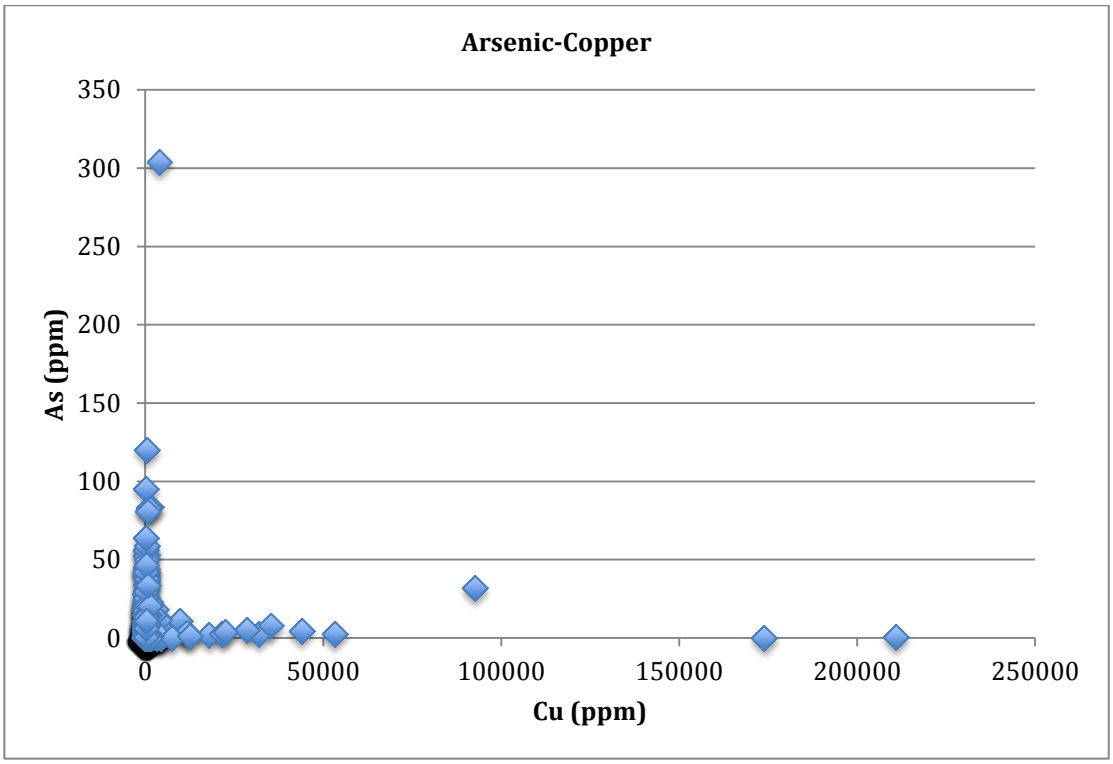

Figure AII.11. Arsenic-copper plot.

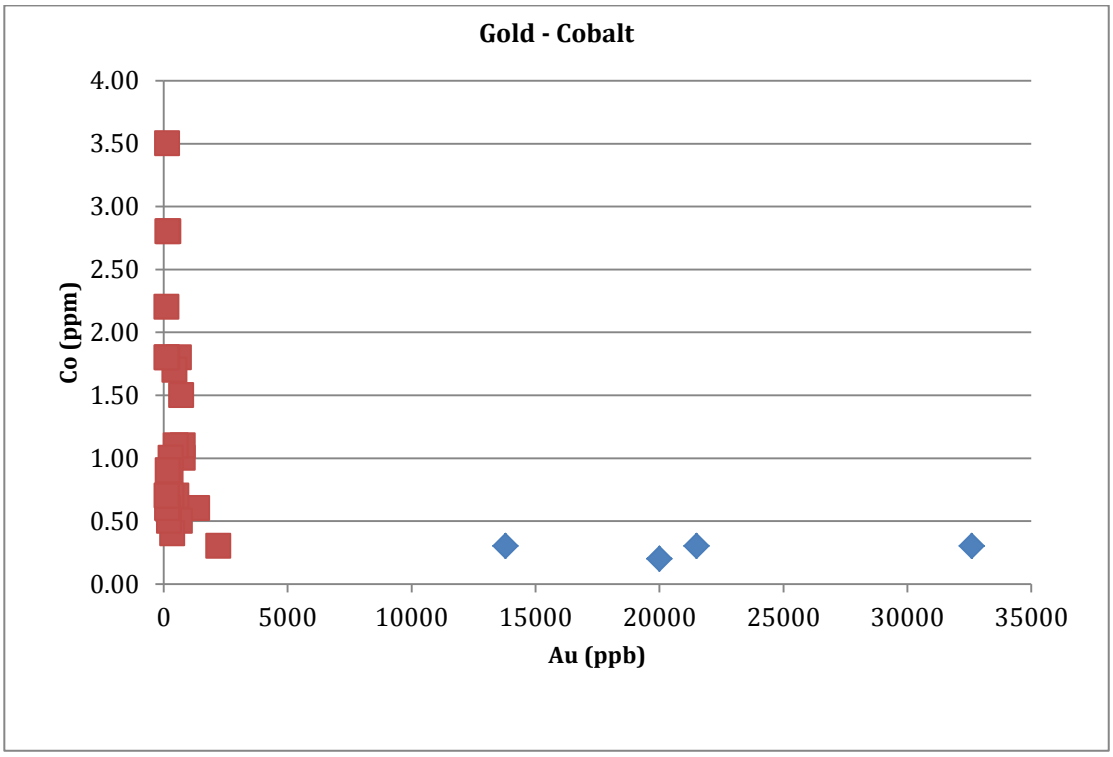

Figure AII.12. Gold-cobalt plot.

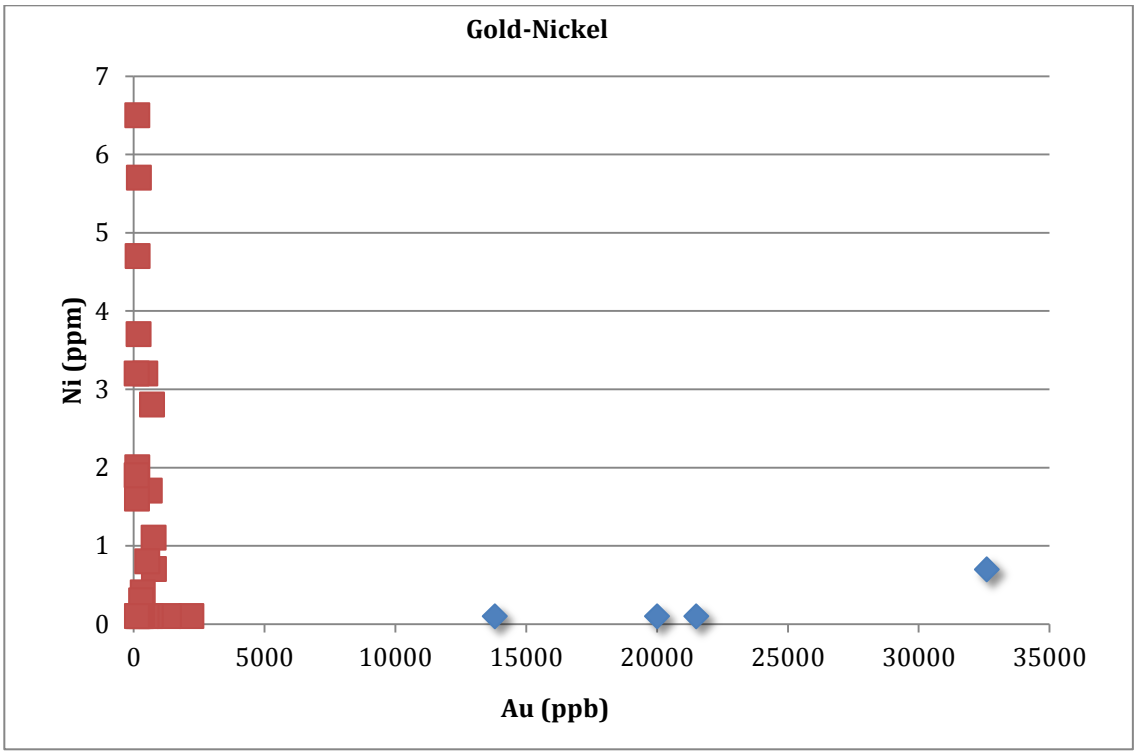

Figure AII.13. Gold-nickel plot.